SILICON BASED CO-INTEGRATED BIOELECTRICAL AND BIOMECHANICAL INTERFACES: APPLICATIONS TO INSECT OLFACTORY NEURAL INTERFACES, MINIATURE NEURAL INTERFACES, AND CARDIAC EXCITATION CHARACTERIZATION

A Dissertation

Presented to the Faculty of the Graduate School

of Cornell University

in Partial Fulfillment of the Requirements for the Degree of

Doctor of Philosophy

by

Ching-Ping Janet Shen

January 2012

SILICON BASED CO-INTEGRATED BIOELECTRICAL AND BIOMECHANICAL INTERFACES: APPLICATIONS TO INSECT OLFACTORY NEURAL INTERFACES, MINIATURE NEURAL INTERFACES, AND CARDIAC EXCITATION CHARACTERIZATION

Ching-Ping Janet Shen, Ph.D.

Cornell University 2012

Biosensors have been extremely important in revolutionizing healthcare and environmental monitoring. In combination with Microelectromechanical Systems (MEMS) devices, biological systems can be probed on similar micro and nano dimensions. This can provide a better understanding of how biological systems function and allow for improved treatment methods for diseases and other maladies. However, there are still key limitations in advancing biosensor technology. One of the limitations is biological integration of sensors with tissue for robust interfaces that minimally damage the tissue and can be used in long-term implantations.

In this dissertation, three projects are presented where strategies have been used and developed to minimize biosensor invasiveness. Ultrasonic horn probes driven at their longitudinal resonances can allow penetration of tough tissue, such as cardiac tissue or the dura layer surrounding the brain. For cardiac tissue, ultrasonic probes can allow study of the onset of arrhythmias in 3D. A model governing the force reduction propertions of ultrasonic horn probes dependent on driving voltage, insertion velocity, and substrate elasticity is presented to guide design and use of ultrasonic horn probes in a variety of tissues. The first three-dimensional recordings of action potential propagation during

ischemia are obtained. The results show the change in activation delay, action potential duration, action potential amplitude, and morphology through the tissue thickness with ischemia.

Secondly, based on the ultrasonic horn design, a new miniature neural interface system is introduced. This system can allow study of probe insertion force effects on long-term reactions, stress fields around the inserted probes, and changes in electrode impedance and electrical activity from nearby cells over time.

Thirdly, a new hybrid insect olfactory sensor system for gas sensing is presented, which uses Early Metamorphosis Insertion Technology (EMIT) to achieve probe integration. The presented olfactory sensor is based on a silicon neural electrode and is shown to monitor responses to pheromone components and the host plant of the insect, *Manduca sexta*. The probe sensor is lightweight enough to be carried on the moths.

In the context of these projects, wireless system designs and implementations are presented that allow portability and parallel recording from the tissue. The first system presented is used for wireless transmission of cardiac action potentials, and the second is designed for multiplexed wireless transmission of neural signals. By making the probe and data collection systems fully wireless, wire-induced stresses on probes integrated with tissue can be reduced and serve to reduce damage to the tissues.

BIOGRAPHICAL SKETCH

Ching-Ping Janet Shen received her B.S. degree as a dual major in Mechanical Engineering and Business, Economics, and Management from the California Institute of Technology in Pasadena, CA in 2006. She will receive her Ph.D. degree in Biomedical Engineering from Cornell University in 2012.

To my parents Wen-Ru and Gon-Yen Shen

ACKNOWLEDGEMENTS

I would like to thank my Ph.D advisor, Professor Amit Lal, for his guidance and support through the years. His advice and ideas have been invaluable during my Ph.D. time in helping me become a more thorough, creative, and better researcher.

I would also like to thank my committee members, Professor Gilmour, Professor Garcia, and Professor Bhave for their advice during my Ph.D. time. In particular, I'd like to thank Professor Gilmour for the useful discussions and collaborations on studying cardiac arrhythmias using silicon microprobes. Professor Gilmour graciously opened up his laboratory for experiments and collaborations on cardiac investigation. I'd also like to thank Prof. Bhave for his advice and suggestions within the MEMS field and introducing me to many relevant MEMS researchers with whom I was able to discuss and further ideas. I'd also like to thank Professor Garcia for his advice on bridging the gap in interdisciplinary research with mechanical and electrical engineering backgrounds.

Additionally, I'd like to thank members of the SonicMEMS and OxideMEMS research labs at Cornell, with whom I have shared much time, and from whom I have learned a lot. In particular, I'd like to thank Abhishek Ramkumar, who introduced me to the cardiac work, Norimasa Yoshimizu, Steven Tin, Yue Shi, Kwame Amponsah, Yuerui Lu, Hadi Hoesseinzadegan, Alper Bozkurt, Ayesa Sinha, and Serhan Ardanuc. I'd also like to thank other members of the SonicMEMS with whom I've worked and collaborated on the most recent projects including Po-Cheng Chen and Bobby Nijjar. i'd like to thank Sachin Nadig for help with force measurements and multiplexer design and creation during his summer internship in the SonicMEMS lab. I'd also like to thank Xiao Wang and Eugene Hwang for circuit design advice, and Flavio Fenton, Niels Otani, and

Fred Von Stein for help and suggestions with cardiac preparations and analysis.

I'm very grateful for all the collaborations, advice, and things I've learned working with the people at Cornell over my Ph.D. time.

TABLE OF CONTENTS

LIST OF FIGURES

CHAPTER 1

INTRODUCTION

Biosensors are capable of revolutionizing our treatment of diseases, as well as serving a key role in environmental monitoring, including in agricultural and veterinary practice [7]. Together with micro-electro-mechanical systems (MEMS) fabrication technology, which is capable of producing patterned mechanical devices with tens to hundreds of nanometers resolution, it is possible to probe biological systems with similar micro and nano dimensions. By probing biological systems in mechanical, thermal, electrical, and chemical modalities, a better understanding of function under normal and abnormal conditions can be obtained.

A key attribute for the success of biosensors is their ability to measure biological quantities and gather as much information as necessary with high resolution while minimizing their invasiveness. While *in vitro* tests can provide a good understanding of some fundamental behavior of cells and engineered systems, *in vivo* and *ex vivo* tests often require a greater focus on system integration and minimized disruption of the biological system. In the current thesis, three biosystems based on silicon MEMS are presented that use and investigate methods for minimizing invasiveness to study health care and environmental monitoring challenges.

1.1 Microelectromechanical Systems (MEMS) biointerfaces

MEMS interfaces to brain and cardiac tissue can be used to monitor electrical activity as the primary indicator of function. MEMS devices can also be used

to monitor mechanical, thermal, and chemical changes to gain an overall understanding of how the system behaves. With this information, methodologies to treat maladies such as paralysis and cardiac arrhythmias can be developed. For interfaces to electrically-active tissue, silicon electrode arrays allow for high resolution fixed geometry measurements of electrical activity in a system. With known electrode geometry, the electrode arrays allow analysis of recorded signals and decomposition into regional variations in activity, which is important in understanding onset of cardiac arrhythmias and neural activity patterns.

For neural recordings, silicon probe arrays such as the Utah and Michigan electrode arrays have been developed with tens to hundreds of recording electrode sites to allow intracortical parallel recordings [8, 9]. However, the effectiveness of these neural implants for long term recordings have not been reliable over long periods of measurement. One of the reasons preventing long term reliability is the body's immune response which can quickly encapsulate foreign objects. Study of the immune response onset and methods to counteract the response have been the subject of much current research.

Silicon multifunctional electrodes are the basis of the projects presented in this thesis. To provide a understanding and rationale for the technology, the following sections include an introduction to cell signaling by neurons and cardiac cells, a comparison of MEMS electrodes to other types of cell recording and microfabricated electrodes, and a discussion of how biological cell activity can be transduced into electrical currents recorded by the electrodes.

1.1.1 Neuronal and cardiac cell signaling

In neurons and muscle cells, networks of cells communicate by conduction of action potentials. Action potentials arise from the flow of ionic currents in and out of cells. Neurons have voltage-gated ion channels that selectively allow ions to flow through them based on the voltage difference between the inside and outside of the cells [10]. The intracellular potential relative to the extracellular potential is called the resting membrane potential. The resting potential is determined by the leakage current predominantly caused by open potassium channels, and is typically on the order of -70 mV relative to the extracellular potential. The value of the resting potential can be approximately determined using the Nernst equation relating internal and external potassium concentrations:

$$E_k = -61 * log \frac{[K+]_{in}}{[K+]_{out}} \tag{1.1}$$

If the cell is stimulated beyond its threshold voltage of approximately -50 mV, voltage-gated sodium channels will begin to open with sodium ions entering the cell resulting in cell depolarization. When the membrane potential is sufficiently depolarized, voltage-gated potassium channels begin to open allowing potassium out of the cell which repolarizes the cell. At this lower potential, the sodium channels begin to inactivate and membrane permeability to sodium ions decreases. The resulting membrane potential waveform is called the action potential and is shown in Fig. 1.1.

Since cardiac tissue is a muscle whose function is to pump blood to the body, the electrical action potentials underlying cardiac tissue is slightly different than

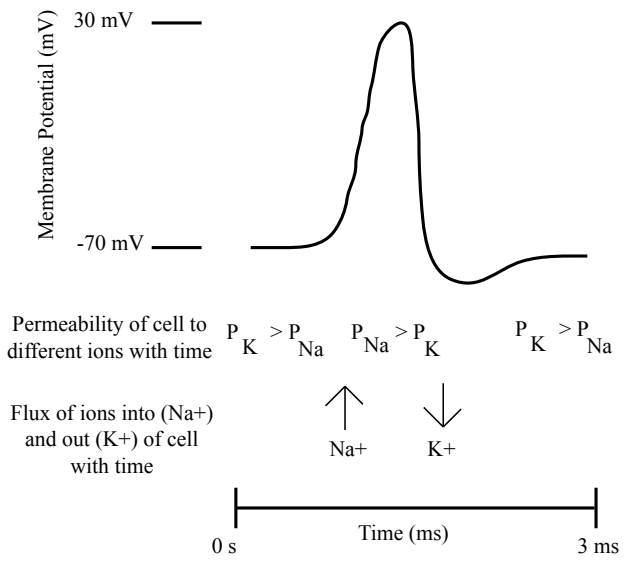

Figure 1.1: Neural action potential with changes in membrane permeability to sodium and potassium ions over time.

for neurons. Cardiac cell action potentials arise through mainly sodium, potassium, and calcium currents. Cardiac cells maintain an intracellular resting potential relative to the extracellular environment of approximately -90 mV. The resting potential is maintained by cell membrane channels with selective permeability to K^+, and its value can be determined using the Nernst equation above.

A typical cardiac action potential signal waveform is shown in Fig. 1.2. The potassium current maintaining the resting potential is called the inward rectifier current I_{K1}. The inward current associated with the fast upstroke in the cardiac action potential is the fast inward sodium current I_{Na}. This results from the opening of voltage-gated sodium channels. Cell depolarization results in the opening of Ca^{2+} and potassium channels, resulting in the I_{Ca} current as well as slow and rapid delayed rectifier currents I_{Ks}, and I_{Kr}. These maintain the

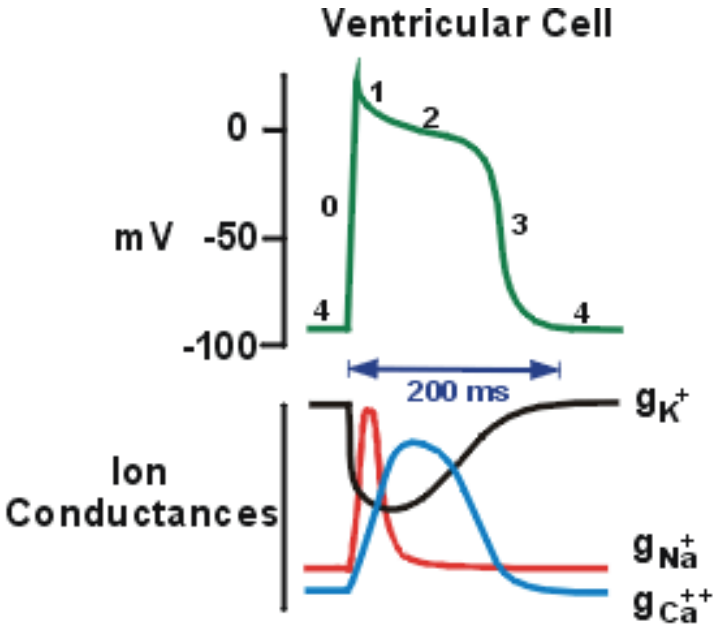

Figure 1.2: Cardiac action potential with changes in membrane permeability (conductance) to sodium, potassium, and calcium ions over time [1].

plateau phase of the cardiac action potential. As the calcium current I_{Ca} inactivates, the potassium efflux currents dominate resulting in cell repolarization. The potassium delayed rectifier currents inactivate after sufficient repolarization, and the inward rectifier potassium current I_{K1} takes over and maintains the resting potential of the cell [11].

1.1.2 Intracellular and MEMS extracellular electrodes

Neurophysiologists have traditionally studied neuron activity using glass microcapillaries that can be pulled to a very fine tip diameter to penetrate a cell's double layer and record cell internal potential changes. The glass capillaries are filled with a conductive solution and a small metal wire is threaded down

the capillary to transduce the ionic signals to electrons in the metal wire [12]. MEMS silicon probes typically differ geometrically in having a relatively large (micron-dimensions) exposed metal electrode surface to the solution and therefore record the extracellular activity representative of the summed activity of nearby cells. It should be noted that some efforts have attempted to make intracellular MEMS probes [12], but the bulk of MEMS electrodes record extracellular activity. Due to the geometric differences and the presence of a capacitive shunt in microcapillary recordings, the frequency filtering properties of the two types of electrodes are different. Glass microcapillaries have low DC resistances of 10-200 MΩ versus MEMS microelectrodes which can have DC resistances of 10-100 GΩ. For this reason, glass microcapillaries behave as low pass filters and MEMS electrodes can behave as high pass filters.

In intracellular recordings, the activity of one cell is recorded. In extracellular recordings, recorded activity includes local field potentials and neural spike activity with frequency components up to 10 kHz. Extracellular recording has limitations due to the mixing of signals from many neurons. However, the problem of confounded signals can be alleviated by having many electrode sites to allow decomposition of signals into their various source signals. Additionally, the main benefit of extracellular recording lies in providing a viable method for longer-term neural recordings. Though immune reactions are seen when electrodes are inserted in biological tissue, in extracellular recordings, cells are not penetrated and damaged as they would be for intracellular recordings.

1.1.3 MEMS electrode substrates and materials

Lithographically defined electrodes enabled with microfabrication technology have utilized various substrates including silicon [8, 9], polyimide [13], and even silk [14]. Silicon-based substrates allow integration of additional circuits, sensors, and microfluidic elements to gather further information about the environment [15]. Polyimide and silk have been introduced as electrode substrates to better match the mechanical elasticity of neural tissue. It is believed that this may reduce likelihood of tissue damage and immune reactions seen in long-term mammalian implants, though the exact mechanisms are unclear. In comparison with silicon electrodes, soft and flexible electrodes often require additional insertion mechanisms to reach target areas in the brain as their mechanical rigidity is not sufficient to penetrate the tissue [16].

1.1.4 Electrochemical transduction mechanism to metal electrodes

The charge exchange between ions in a solution and electrons in metal electrodes occurs capacitively at small current densities, and with reduction-oxidation reactions at larger current densities. When a partially soluble metal electrode is immersed in an electrolyte, thermodynamic processes favor chemical reactions which result in the dissolution of metal into metal ions and the build up of negative charges on the metal electrode surface [17]. Noble metals experience an exchange of electrons with the solution [12]. Positive charges from the electrolyte accumulate near the electrode surface. This buildup proceeds until an equilibrium state is reached where the charge accumulated in the

metal is enough to balance the thermodynamic favorability of the chemical reaction, so that reduction and oxidation reactions occur at equal rates. From this process, a capacitive electrical double layer (EDL) is formed at the surface of the electrode. This double-layer capacitance in conjunction with a series resistance ultimately affects the frequency response of ion to electron transduction.

Based on the Stern model, the interfacial capacitance C_I can be described by the combination of a closely held Helmholtz capacitive layer C_H and a diffuse layer C_D [17]. It is described by equation 1.2 where A is the electrode area, d_{OHP} is the distance to the end of the outer Helmholtz plane, V_{OHP} is the voltage at the outer Helmholtz plane, L_D is the Debye length over which the potential decays by a factor of e, C* is the concentration of the bulk solution in moles/liter, and ϵ_o and ϵ_r are the permittivity of free space and dielectric constant, respectively.

$$\frac{1}{C_I} = \frac{1}{C_H} + \frac{1}{C_D} = \frac{1}{A}\left(\frac{d_{ohp}}{\epsilon_o \epsilon_r} + \frac{L_D \cosh\left(\frac{zV_{OHP}}{2V_t}\right)}{\epsilon_o \epsilon_r}\right) \tag{1.2}$$

This can be simplified to the below expression at 25°C

$$\frac{1}{C_I} = \frac{1}{C_H} + \frac{1}{C_D} = \frac{1}{A}\left(\frac{d_{ohp}}{\epsilon_o \epsilon_r} + \frac{1}{2.28\sqrt{C^* \cosh(19.5 V_{OHP})}}\right) \tag{1.3}$$

The interface also consists of a resistance which serves as the DC path for current flow in parallel with the interfacial capacitance. This is termed the charge transfer resistance. For small applied voltages, this is shown to be $R_{ct} = \frac{V_t}{J_o z}$ where V_t is the thermal voltage, J_o is the exchange current density [A/cm^2], and z is the valence of the ion responsible for conduction. Additionally, there is a series resistance which arises from the metal electrode resistance and solution resistance shown as R_s in Fig. 1.3. Diffusion effects can be significant and add to further terms in the equivalent circuit, but are not relevant at the low fre-

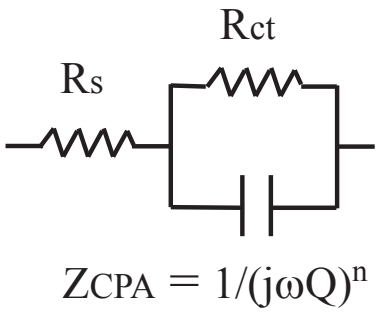

Figure 1.3: Electrode-electrolyte interface equivalent circuit.

quencies discussed here with platinum electrodes. Empirically, the interfacial capacitance has been shown to fit the model

$$Z_{CPA} = \frac{1}{(j\omega Q)^n} \tag{1.4}$$

where $\omega = 2\pi f$, Q is the magnitude of the impedance, and n is a constant between 0 and 1 [18]. Described in this way, the equivalent circuit is shown in Fig. 1.3.

1.2 Summary of contributions

The current thesis presents results pertaining to three areas of investigation summarized below, along with the key contributions in each area.

Ultrasonic horn probe system for study of cardiac arrhythmias in 3D with wireless data transmission

Sudden cardiac death is one of the leading causes of death in the industrialized world, but the mechanisms behind its onset are not fully understood. One of the ways to investigate the mechanisms further is to mesure electrical activity using microelectrodes. However, the stiffness of cardiac tissue is often high to allow penetration with silicon electrodes which are brittle or lower stiffness polyimide electrodes. Silicon ultrasonic horns with integrated electrodes can decrease the insertion force required to penetrate cardiac tissue, and allow extraction of activity patterns in 3D throughout the tissue thickness. With this data, models of cardiac arrhythmia onset can be further developed from current 2D models to understand how heart rhythms function in normal and abnormal behavior. The key contributions in this area are listed below and presented in Chapters 2, 3, and 4:

1. Derivation of an empirical model to describe silicon ultrasonic horn reduced insertion force as a function of insertion velocity, substrate elasticity, and piezoelectric driving voltage. This model can be used to design and predict maximum forces that the substrate and probe will encounter during insertion.
2. Extraction of action potentials through the depth and along the surface from base to apex in cardiac tissue to understand ventricular fibrillation onset using silicon ultrasonic horn probes. It is shown that activation time, action potential delay, and action potential morphology differences exist both laterally and transmurally in the tissue during a period leading up to ventricular fibrillation.

3. Design and development of a wireless data transmission chip for cardiac action potentials. Using this wireless transmission chip, the action potential restitution curves can be extracted to describe the likelihood of undergoing cardiac alternans, a precursor to ventricular fibrillation.

Hybrid insect olfactory system for gas sensing

Insects have developed highly sensitive olfactory sensors over billions of years of evolution, with sensitivities of parts per trillion that surpass man-made gas sensors. By developing a neural interface to the olfactory neural tissue of moths, it is possible to sense the neural responses to olfactory stimulants in the air. This allows for a sensor system that is portable and very low power, and most critically enables high sensitivity. The key contribution in this area is below and is presented in Chapter 5:

1. Design, development, and demonstration of an hybrid insect olfactory sensor based on an integrated silicon neural probe.

Miniature ultrasonic horn probes for neural interfaces

Many people suffer from paralysis or are amputees, and neural interfaces can potentially allow these patients to regain function of paralyzed parts of their body directly or through the use of prosthetics. Immune reactions currently limit the lifetime of these neural implants, though the exact mechanisms leading to particular immune reactions and the methods to combat them still are under investigation. The key contributions in this area are listed below and presented in Chapters 6 and 7:

1. Development of a miniature ultrasonic horn neural probe that can allow measurement of mechanical properties such as stress fields in the tissue near the probes, effect of probe insertion force on long-term immune reactions, while simultaneously measuring neural electrical activity.
2. Design and testing of a multiplexed wireless transmission integrated circuit for amplification and wireless transmission of neural electrical activity and neural strain induced on inserted electrodes.

CHAPTER 2

CHARACTERIZATION OF MECHANICAL AND ELECTRICAL PROPERTIES OF SILICON ULTRASONIC HORNS AND PROBES FOR CARDIAC AND NEURAL RECORDING

2.1 Motivation

Microfabricated silicon probes that can be ultrasonically inserted into cardiac tissue [2] have been previously presented. These probes provide two main benefits, namely the ability to record from many sites with well defined spatial locations, and the ability to penetrate tissue while minimizing relative penetration force [2]. These probes can be used to study the onset of cardiac arrhythmias in 3D throughout the depth of the tissue. In this chapter, further characterization and development of a model to describe the force reduction properties of these devices is presented. The presented force-reduction properties suggest the promise of ultrasonic horn probes for applications in reducing initial insertion trauma for neural implants and creation of long-term viable implants.

2.2 Ultrasonic horn probes design and fabrication

Titanium ultrasonic transducers are well known instruments for ultrasonic surgery such as for phacoemulsification. However, by implementing ultrasonic transducers in silicon, particle ultrasonic velocities of eight times higher than titanium can be achieved due to the high dislocation density in titanium which limits particle velocity [19]. Additionally, as with silicon-based neural elec-

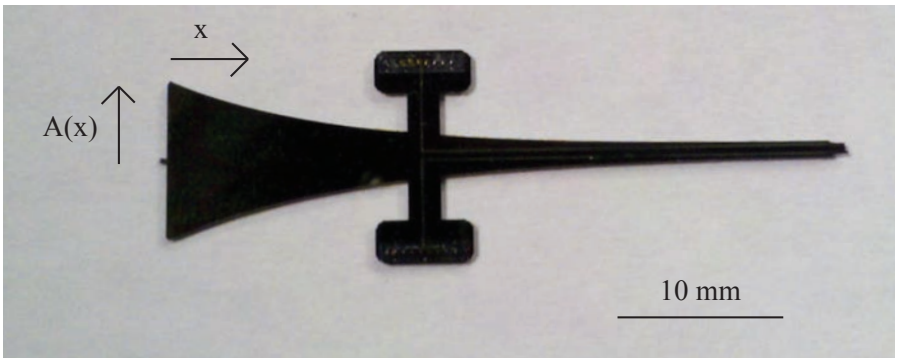

Figure 2.1: Shape of catenoidal horn probe.

trodes, silicon ultrasonic transducers can contain integrated sensors to monitor the environment, and can generate less heat compared to titanium based instruments. While several horn shapes (A(x) in Fig. 2.1 have been previously investigated, including exponential, linear, and stepped horns, a catenoidal horn shape allows for a large displacement amplification between the end and tip of the probe [19]. The catenoidal horn shape is shown in Fig. 2.1 and defined by

$$A(x) = A_1 * cosh^2(\alpha(L - x)) \tag{2.1}$$

where

$$\alpha = \frac{acosh(\sqrt{\frac{A_0}{A_1}})}{L} \tag{2.2}$$

where A_0 and A_1 are the cross-sectional areas of the probe at the tip and end, and L is the length of the probe not including the probe tips. The mass of the tips are small compared with the mass of the ultrasonic horn and so do not significantly affect the motion of the horn.

The simulated longitudinal displacements for a probe with dimensions of 10 mm wide at the end of the probe, 1 mm at the tip of the probe, and 140 μm thick at the ends of the probe bonded to another probe 140 μm thick are as shown

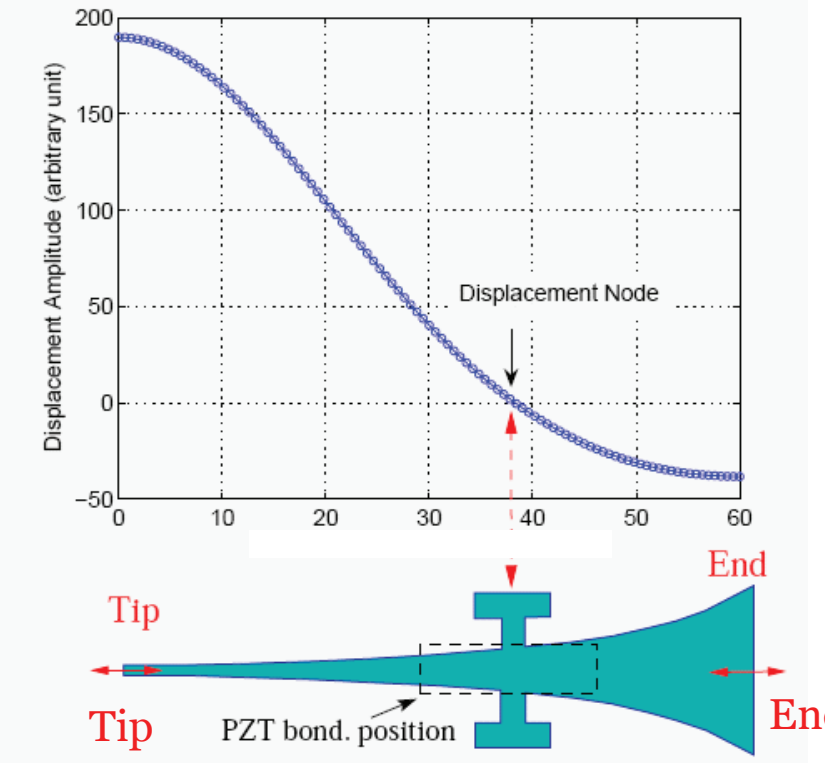

Figure 2.2: Finite element simulation of catenoidal horn longitudinal displacement (adapted from [2]). An amplitude magnification of 4 is obtained between the tip and end of the probe.

in Fig. 2.2. The silicon horn displays an approximately four-fold displacement amplification between the end of the probe and the tip of the probe.

2.2.1 Fabrication process flow

Probes with platinum recording sites

The fabrication process flow for the probes are shown in Fig. 2.3. The process starts with four inch silicon wafers coated with a 1 μm thick film of LPCVD nitride on both sides of the wafer. This insulation layer serves to isolate the metal signal lines from the silicon substrate and impede the formation of Schot-

tky electrical contacts. After LPCVD nitride deposition, platinum is deposited using a lift-off photoresist process. Platinum is selected as the metal interface to the electrolyte due to its good biocompatibility and chemical stability. To promote adhesion of platinum to silicon nitride, a 30 nm layer of chrome is first evaporated followed by 250 nm of platinum. Following platinum evaporation and patterning, PECVD nitride is deposited to insulate the platinum. PECVD nitride can be deposited at a temperature of 400 °C, which ensures thermal compatibility with the low-melting temperature metals on the wafer. The low-stress LPCVD nitride recipes, on the other hand, are run at temperatures around 1000 ° C. This allows deposition of a more conformal layer. Following PECVD nitride deposition, contact openings in the nitride to the platinum metal are lithographically defined , and the silicon nitride is dry etched. This is followed by frontside patterning and etching of the probe edges in nitride and silicon, followed by a final backside wet potassium hydroxide (KOH) etch to release the probes. Alternatively, deep reactive ion etching (DRIE) can also be used to define and release the probes from the wafer.

Probes with platinum recording sites and integrated strain gauges

Probes with integrated strain gauges are fabricated from < 100 > silicon wafers. The process flow for fabrication is shown in 2.4, and consists of seven lithography steps, as introduced in [20]. Briefly, LPCVD polysilicon is implanted with boron at a dose of $2x10^{15}$ ions/cm^2 at 100 keV, and is used to realize the polysilicon strain gauge resistors. Doped polysilicon exhibits piezoresistive behavior where its resistance changes with strain. The sensitivity of a film is governed by the gauge factor (GF), defined as

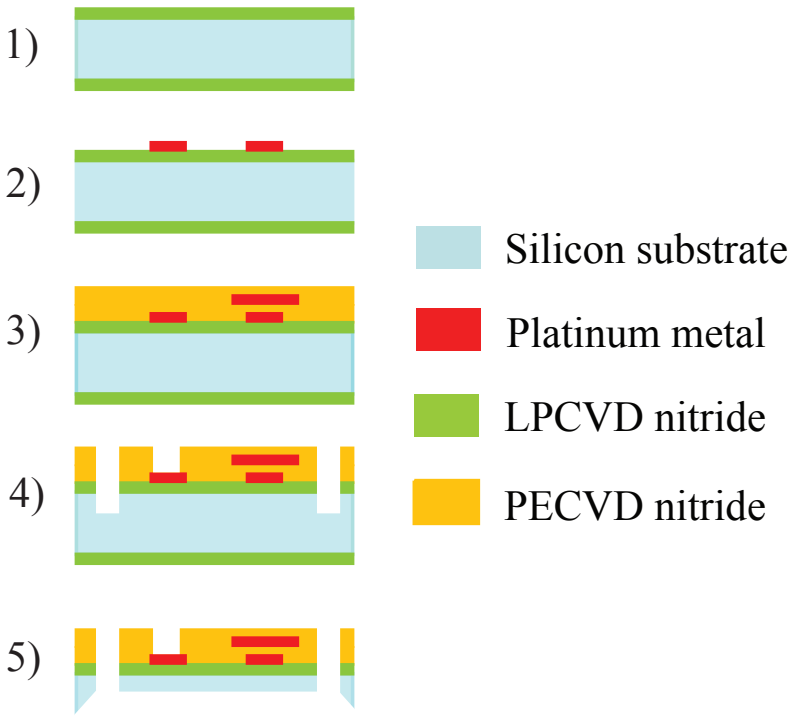

Figure 2.3: Process flow for microfabricating neural probes illustrated using cross-section of probe tip. 1) Deposit LPCVD nitride on silicon wafer. 2) Deposit photoresist and evaporate and pattern metal using lift-off. 3) Deposit an insulating layer of nitride, evaporate and pattern another ground layer of metal using lift-off, then passivate surface with another layer of silicon nitride. 4) Etch openings to bond and recording sites. DRIE silicon to define probe boundaries. 5) KOH etch to release probes.

$$GF = \frac{R_s - R_0}{R_0 \epsilon} \tag{2.3}$$

where R_s is the resistance with strain ϵ and R_0 is the original resistance [21]. The resistors are defined lithographically, and are electrically contacted with aluminum alloy (Al + 1% silicon) metal lines. The wafers are then annealed to activate the dopants and produce a good contact between the aluminum and polysilicon. Insulating PECVD nitride is deposited, followed by platinum evap-

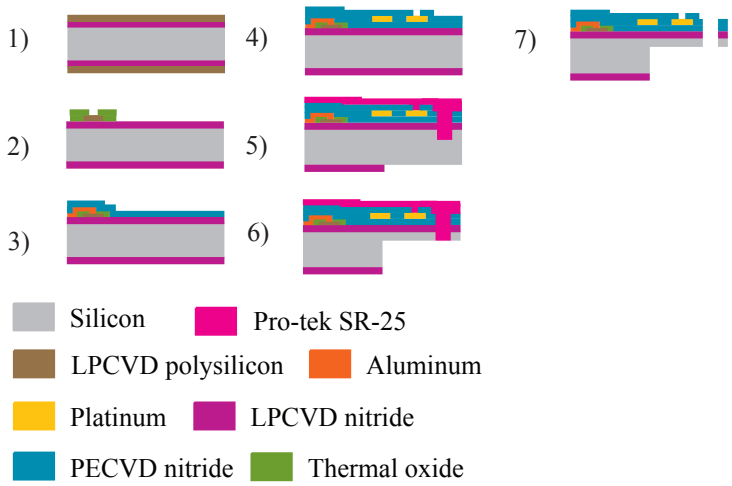

Figure 2.4: Process flow for fabricating silicon platinum electrodes with integrated strain gauges. LPCVD nitride and LPCVD polysilicon are first deposited on the wafers. The polysilicon is ion implanted with Boron and patterned lithographically to define the piezoresistors. A thermal oxide film is grown, followed by sputtering of aluminum contacts to the piezoresistors. PECVD nitride is deposited as an insulation material, followed by evaporation of platinum for metal electrodes and lines. This is followed by PECVD nitride top insulation deposition, and patterning and etching of insulation and frontside patterns. The probe is released with DRIE backside etching.

oration to define electrical recording sites in platinum. The probes are designed in catenoidal horn shapes. As with the platinum-only probes, the horns are adhesively bonded with lead zirconate titanate (PZT) plates whose longitudinal resonance frequency is matched with the longitudinal resonance frequency of the ultrasonic horn probes.

The polysilicon resistors are laid out in a Wheatstone bridge configuration, with two variable polysilicon resistors that sense probe strain, and two constant polysilicon resistors, as shown in Fig. 2.5a. As the probe cantilever bends, the resistances on the variable polyresistors change allowing monitoring of strain

on the probes. For an applied voltage V_{in} over the Wheatstone bridge, the output measured voltage will depend on the non-variable resistors, R_1 whose values are assumed to be approximately equal, and the variable resistors which will have resistances of $R_1 + \Delta R$ assuming both resistors feel the same strain. This will be true in cases of longitudinal and bending strain on the probe. The expression for the measured output voltage will then be given by

$$V_{out} = AV_{in}(\frac{R_1 + \Delta R}{2R_1 + \Delta R} - \frac{R_1}{2R_1 + \Delta R}) \tag{2.4}$$

where A is the gain of the amplifier. This simplifies to

$$V_{out} = AV_{in}\frac{\Delta R}{2R_1 + \Delta R} = AV_{in}\frac{\Delta R}{2R_1} \tag{2.5}$$

assuming ΔR is much smaller than R_1. The output voltage is proportional to the resistance change, which is proportional to the strain on the resistors.

The bending and longitudinal sensitivities of the probe were measured using a motorized micrometer stage and a force transducer. As shown in Fig. 2.5b, the polyresistors are more sensitive to bending forces versus longitudinal forces. This is expected since the effective cantilever spring constant in the bending direction is orders of magnitude lower than that in the longitudinal direction. The force vs. Wheatstone bridge voltage shown in 2.5b was characterized for a catenoidal horn probe 9 mm long, 200 μm wide, and 140 μm thick.

After probe fabrication, the probes are adhesively bonded to a dummy probe with the same dimensions to allow symmetry in the excited structure. Piezoelectric lead zirconate titanate (PZT-4) plates are then adhesively bonded to the

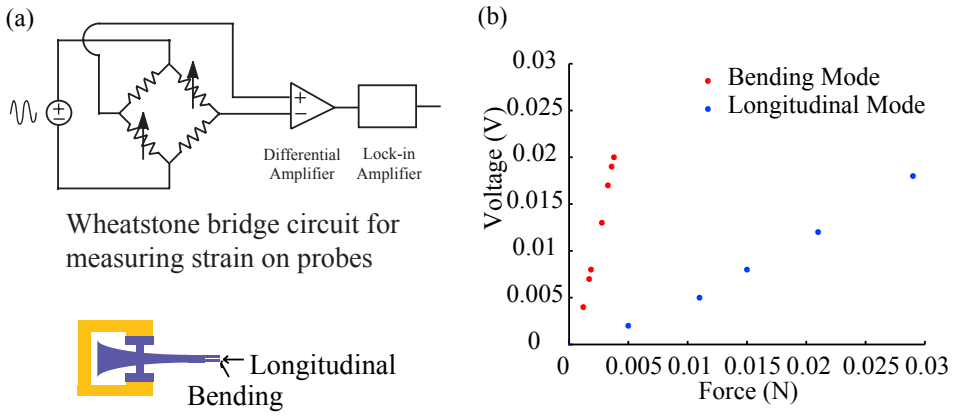

Figure 2.5: Wheatstone Bridge configuration and characterized bending (left dots) and longitudinal (right dots) stiffnesses for probe with integrated strain gauges.

silicon probes to mechanically drive the probes. The PZT is actuated at its $\lambda/2$ resonance, which is matched to the 110 kHz longitudinal resonance of the silicon probe. With a driving voltage of 10 Vpp on the PZT plates there is approximately a 15% reduction in the axial force imposed on the probe tip during tissue insertion for 120 μm thick probes, and a 50% reduction for 60 μm thick probes [2].

To verify the probe tip displacement, interferometric measurements of the silicon horn longitudinal displacement were taken for a frequency range around the anticipated longitudinal resonance frequency. Due to the limited interferometer range of focus, the probes were driven using a 600 mVpp sine wave, instead of the typical 8-16 Vpp used during cardiac tissue insertion. A Stanford Research Systems SR844 lock-in amplifier was used to extract the amplitude and phase of the measured interferometer signals with respect to the drive signals generated by an Agilent 33250A function generator. LabVIEW code was used to control the function generator frequency and read in the lock-in amplifier data using a GPIB interface. As expected, the frequency sweep of the silicon

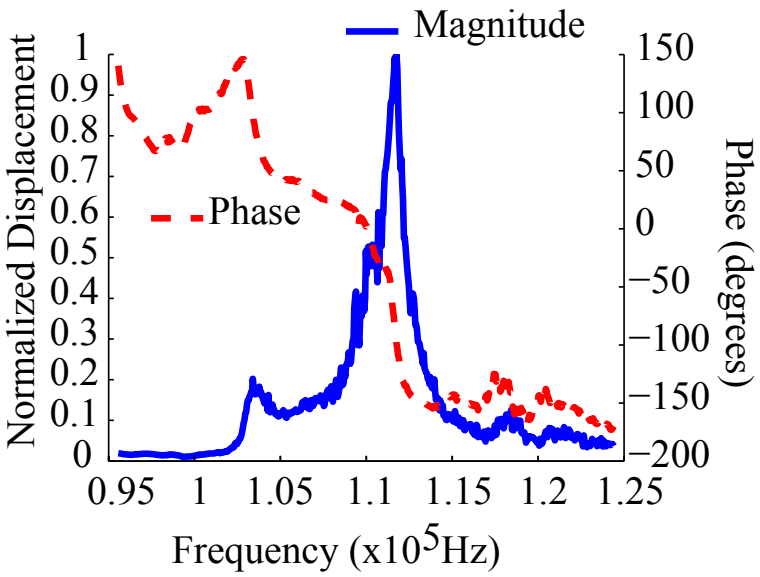

Figure 2.6: Interferometer measured displacement versus frequency of the cardiac ultrasonically actuated device in air with various driving frequencies and a driving amplitude of 600 mVpp. The normalized displacement (solid line) and the phase (dotted line) are shown.

horn probe revealed the maximum displacement at a frequency of 111.75 kHz (Figure 2.6), which matches closely to the longitudinal resonance of the silicon probe (110 kHz) given by finite element simulations using ANSYS. Small variations in probe longitudinal resonance are expected to arise from fabrication tolerances and bonding alignment.

2.3 Ultrasonic horn probe electrical characterization

With the ability to penetrate cardiac tissue with ultrasonically inserted probes, it is also important to understand the electrical characteristics of the probes for action potential recording. The fabricated probes contain ten planar 35 μm x 35 μm

platinum recording sites used to capture cardiac action potentials at various 3D locations within the tissue wall. Using electrochemical impedance spectroscopy (EIS), the electrode impedances can be measured.

A three-electrode configuration is used with a Gamry FAS2 potentiostat, with the setup shown in Fig. 2.7. The silicon ultrasonic probe serves as the working electrode whose impedance is of interest. A platinum sheet with a large area (2 cm^2) compared to the working electrode is used as the counter electrode, and an Ag/AgCl wire is used as the reference electrode. Cyclic voltammetry is first performed on the electrode sites to allow cleaning of the electrode surface prior to impedance measurements to remove any excess dirt. During the tests, the electrodes are immersed in 0.9% physiological saline. A 1 mV sine wave is applied between the counter electrode and the reference electrode. The resulting current required to maintain a constant voltage between the working electrode and the reference electrode is measured. The equivalent circuit parameters were estimated to the fit as shown in Figure 2.8b.

The electrode-electrolyte interface properties were measured and fit to the model presented in the previous chapter, with the spreading resistance R_s, the interfacial capacitance Z_{CPA}, and the DC path characterized by the charge transfer resistance R_{ct} [17]. The measured and fit circuit parameters for the silicon ultrasonic probes are shown in Figure 2.8 [22, 3].

2.4 Mechanical characteristics of ultrasonic horn probes

A basic understanding of the mechanical properties of the ultrasonic horn probes has been presented with a relative decrease in tissue penetration force.

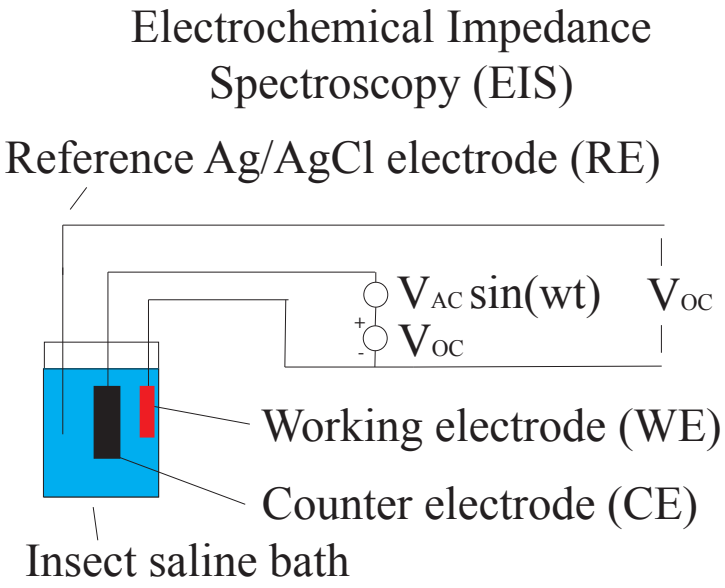

Figure 2.7: Setup for electrochemical impedance spectroscopy (EIS). The counter electrode is a 2 cm^2 platinum sheet. The reference electrode is an ideally nonpolarizable Ag/AgCl electrode, and the working electrode is the microfabricated probe of interest.

In this section, the absolute penetration forces are further investigated as well as the optimal insertion parameters to minimize insertion forces including PZT drive voltage and insertion velocity. To characterize probe insertion forces, probes are also fabricated with integrated strain gauges.

2.4.1 Damping of ultrasonic horns in fluids

By changing the boundary conditions on the ultrasonic horn probe, one would expect the resonance characteristics of the probe to change as well. As a resonant system, the quality factor, Q, can be defined as the ratio of energy stored per cycle divided by the energy dissipated per cycle. The quality factor can be

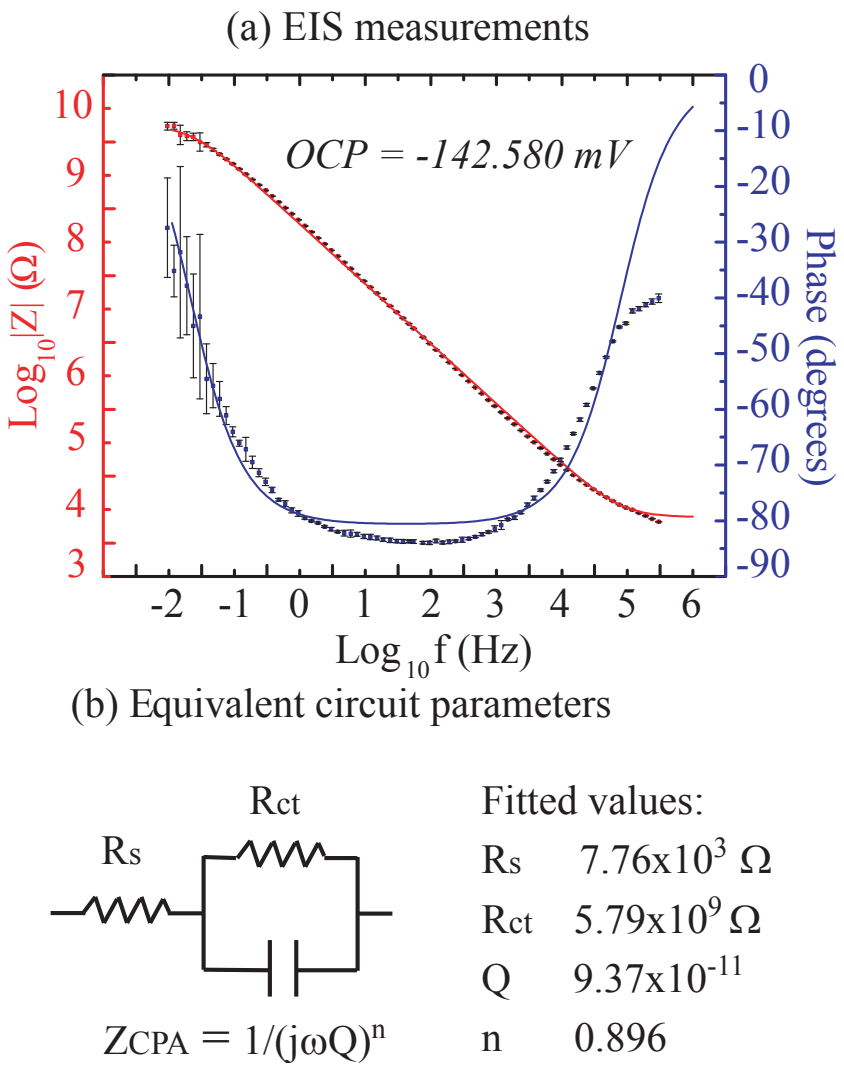

Figure 2.8: Measured and fit electrode-electrolyte equivalent circuit parameters. The equivalent circuit consists of a spreading resistance, Rs, a charge transfer resistance, Rct, and an interfacial capacitance, Zcpa (adapted from [3]).

monitored by observing the displacement of the probe using an optical interferometer, and measuring the resonance frequency f_r and width of the resonance peak at half the peak energy Δf_{-3dB}:

$$Q = \frac{f_r}{\Delta f_{-3dB}} \tag{2.6}$$

For the coupled silicon horn-PZT system, the shift in quality of resonance can also be monitored by measuring the current required to drive a given voltage on the piezoelectric plates. As the driving voltage converts electrical to mechanical energy, and the mechanical motion of the PZT is coupled to the quality of resonance of the silicon horn as well as affecting the electric field in the PZT, the impedance of the PZT can be used to monitor the quality of resonance of the silicon horn structure. The equivalent circuit of a piezoelectric material is shown in Fig. 2.9, and described by capacitors, inductors, and resistors dependent on the material properties of the piezoelectric actuator [23]. The equivalent circuit parameters can also be easily extracted from the impedance spectrum of the piezoelectric actuator and the resonance and anti-resonance frequencies. The capacitance C_o is the capacitance of the piezoelectric plates with no voltage applied, and can be measured directly from the piezoelectric actuator at low frequencies away from resonance. The resistance R_m is the lowest impedance in the impedance spectrum. The resonance frequency is given by

$$\omega = \sqrt{\frac{1}{L_m C_m}} \tag{2.7}$$

and the anti-resonance frequency is given by

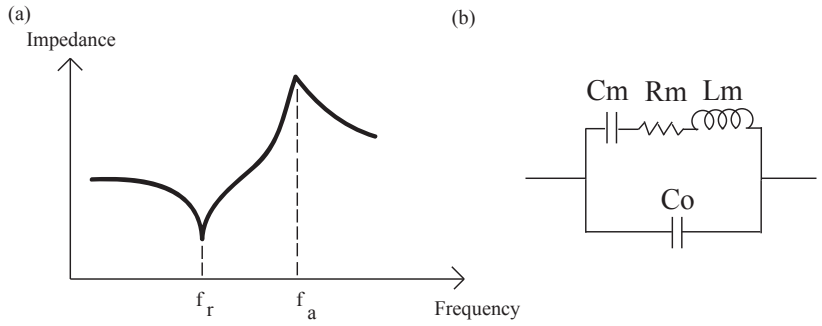

Figure 2.9: (a) Impedance spectrum of a piezoelectric driver with resonance and anti-resonance frequencies shown. (b) Equivalent circuit of piezoelectric material near resonance. The parameters can be calculated from the impedance spectrum.

$$\omega = \frac{1}{2\pi}\sqrt{\frac{1}{\frac{1}{\frac{1}{C_m}+\frac{1}{C_o}}L_m}} \tag{2.8}$$

The equivalent circuit parameters L_m and C_m can be derived as

$$L_m = \frac{1}{2\pi^2}\frac{1}{C_d}\frac{1}{f_r^{\,2} - f_a^{\,2}} \tag{2.9}$$

$$C_m = C_d\frac{f_r^{\,2} - f_a^{\,2}}{f_a^{\,2}} \tag{2.10}$$

and the quality factor further defined as

$$Q = \frac{1}{\omega_r C_m R_m} \tag{2.11}$$

The ultrasonic horn probe was inserted a distance of 3.5 mm into several different percent agarose substrates. The resonance frequency and impedance of the probe in air is 269.9 Ω with a resonance frequency of 111.17 kHz. As shown in Fig. 2.10, there is a less than 0.2% change in the resonance frequency when the probe is in air versus 1% agarose, while the impedance of the probe shifts

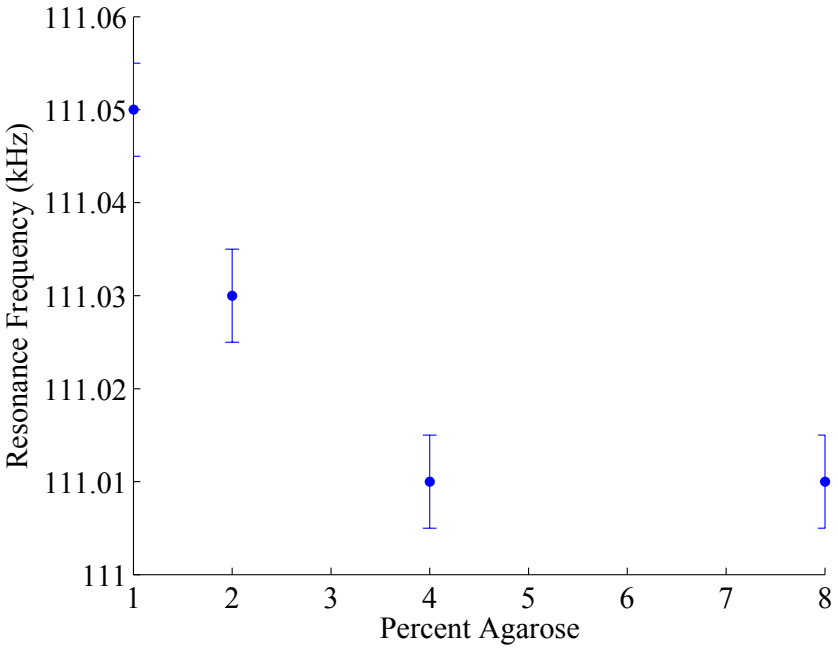

Figure 2.10: Shift in piezoelectric resonance frequency with probe insertion into agarose substrates.

29.4% between air and when in 8% agarose as shown in Fig. 2.11. This indicates damping of the ultrasonic horn motion, but a small shift in resonance frequency. The shift in resonance frequency accounts for a less than 0.1% decrease in the quality factor, while the increase in impedance at resonance shifts the quality factor by up to 23%, as shown in Fig. 2.12.

2.4.2 Ultrasonic horn probe insertion forces measured with integrated strain gauges

Absolute forces on the probes during substrate insertion can be estimated and measured with integrated strain gauges. The fabrication process flow for these probes has been presented earlier. It is observed that with increasing PZT driv-

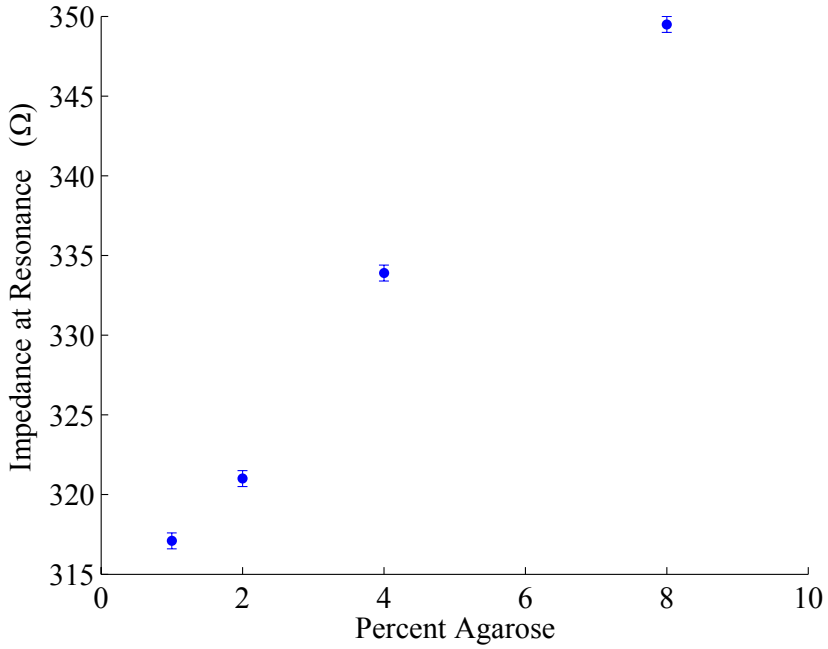

Figure 2.11: Shift in piezoelectric impedance with probe insertion into agarose substrates.

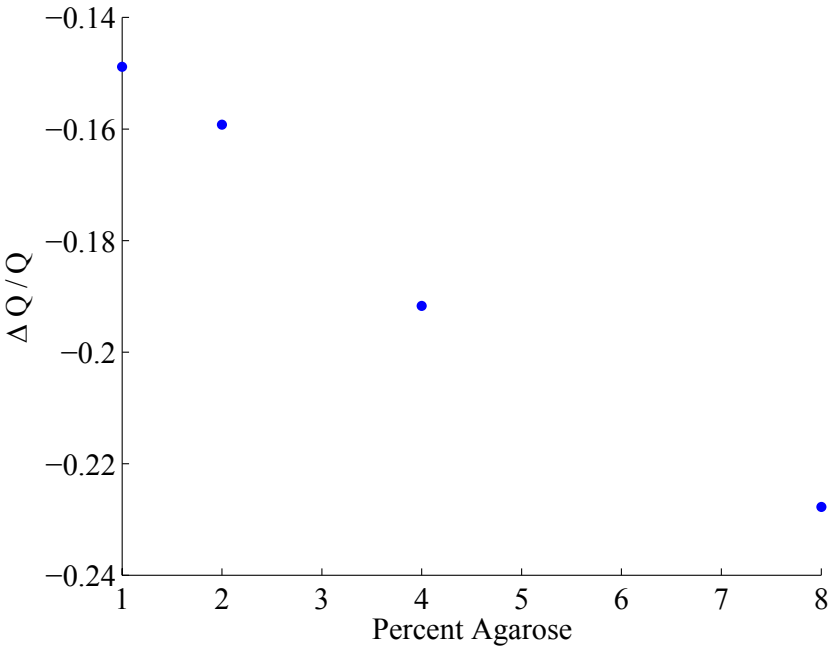

Figure 2.12: Change in quality factor from increase in impedance at resonance with probe insertion into agarose substrates.

ing voltage, the peak force measured by the strain gauges decreases, as shown in Fig. 2.13. With the integrated strain gauges, the absolute forces introduced at the tissue surface can be measured given that the axial compression of the silicon probes is much smaller than the compression introduced into tissue or gelatin. Based on insertion experiments with integrated strain gauges, the insertion interface characteristics display large substrate dimpling with no ultrasound and little to no surface bending with 20 Vpp driving ultrasound, diagramatically illustrated in 2.14. The measured insertion forces are shown for a probe inserted with a 20 Vpp PZT driving voltage and 0 V driving voltage in Fig. 2.15.

Euler's compression buckling formula gives the maximum force a beam can withstand before buckling as

$$F_{cr} = \frac{\pi^2 EI}{KL^2} \tag{2.12}$$

where

$$I = \frac{wt^3}{12} \tag{2.13}$$

where K = 2 for a fixed-roller beam. The boundary conditions on the probes during insertion are such that one end is clamped into a holder while the tip is driven into the substrate. For forces smaller than the buckling load, the probe can return to the equilibrium stable position. At a sufficiently large force, the probe breaks through the substrate surface at which point the probe inserts through the substrate. The probe is inserted a constant distance then allowed to remain at a fixed position. At this point, the measured strain stabilizes at a fixed value. This insertion characteristic is demonstrated in Fig. 2.16. The insertion

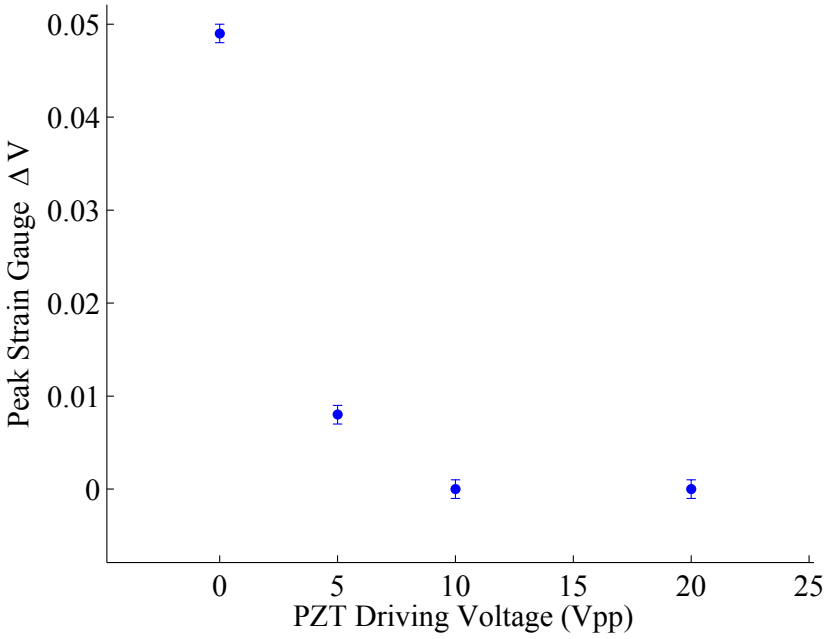

Figure 2.13: Peak change in strain gauge voltage with driving PZT voltage.

velocity is 2.6 mm per second.

2.4.3 Model for insertion force reduction as a function of varying velocity, substrate, and PZT driving voltage

In this section, the conditions governing the insertion forces felt by the substrates and probes are further investigated by varying insertion velocities, ultrasonic PZT driving voltages, and substrate elasticity. Nabibekov et al. presented a theory for ultrasound enhanced insertion into tissue [24]

$$f_o - F_x = -mA\omega^2 sin(\omega t + \phi) + k_1\dot{x} + k_2\dot{x}^2 \tag{2.14}$$

where ω is the ultrasonic drive frequency, A is the amplitude of oscillation, m is

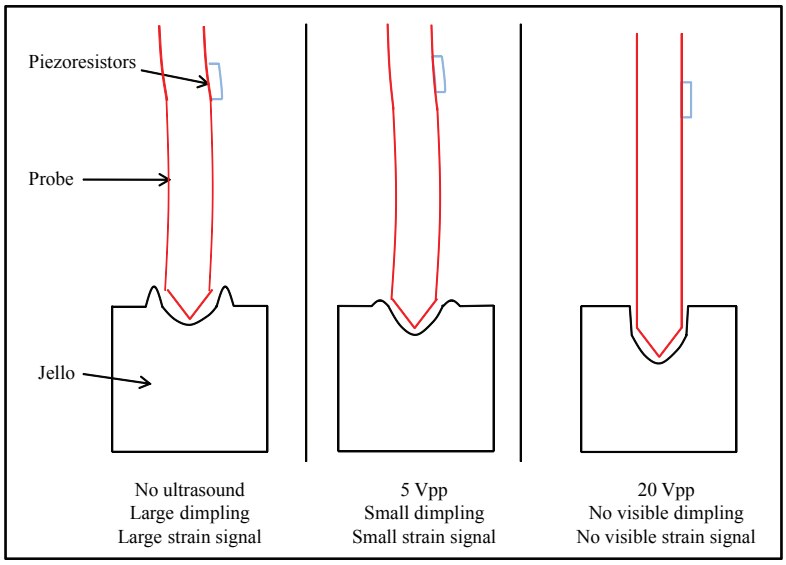

Figure 2.14: Probe interface characteristics with changing PZT driving voltage.

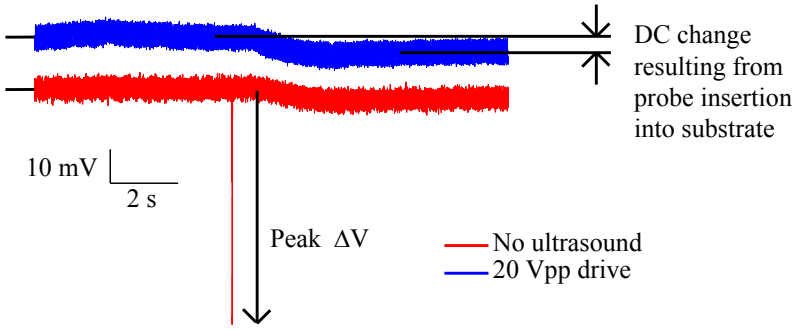

Figure 2.15: Measured strain gauge voltages for probe insertions with no ultrasound and 20 Vpp PZT driving voltage. The probe moves a constant distance down into the substrate and then movement stops. There is a DC shift generated in the strain signal from the probe insertion into the substrate, as well as a transient peak in the case of the no-ultrasound insertion.

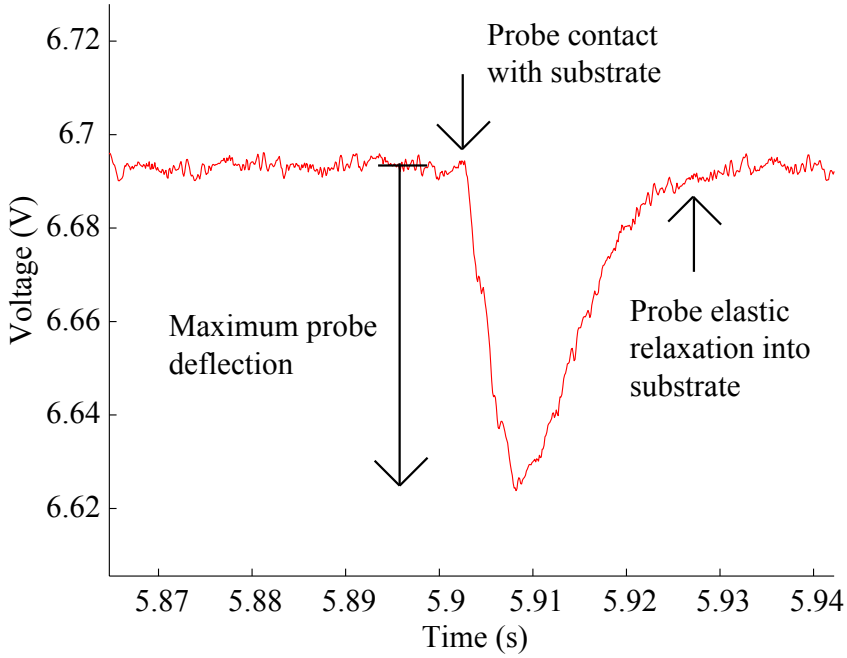

Figure 2.16: Measured strain gauge voltages for probe insertions with no ultrasound.

the mass of the moving segment of the probes, f_o is the tissue reaction force, $\dot{x}$ is the insertion velocity, and F_x is the user applied insertion force. k_1, k_2, and ϕ are constants.

The amplitude of oscillation of the probes, A, can be measured using an optical interferometer. The interferometer measures the phase shift between a laser directed at the sample and a reference laser beam. The measured values and fit are shown in Fig. 2.17. Since the optical interferometer has a limited range of focus, the tip displacements are measured for small driving voltages. Assuming an approximately linear PZT drive voltage and tip displacement relation which would hold given a general forced response to a sinusoidal input driving function, the tip displacements for the probe with various drive voltages including 0, 10, and 20 V can be estimated with

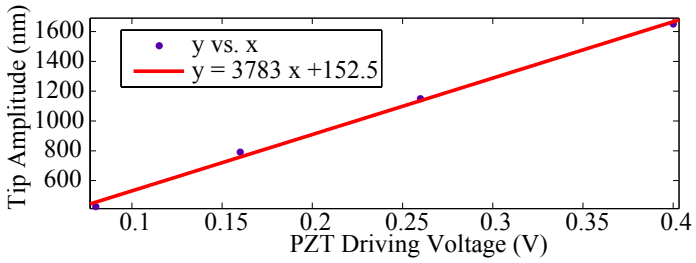

Figure 2.17: Displacement of ultrasonic horn probe with varying PZT drive voltages. A linear slope of 3783 nm/V is accurrate to describe probe motion in air.

$$Amplitude[nm] = 3783 * Voltage[V] + 152.5 \tag{2.15}$$

where A is the amplitude in nanometers, and V is the voltage in volts. The estimated tip displacement amplitudes at drive voltages of 10 and 20 V are 38.0 μm and 75.8 μm, respectively.

To measure the forces during probe insertion, the setup shown in Fig. 2.18 is used with a Chatillon DGGS force transducer. A glass slide is placed on top of the force transducer and the agarose/gelatin is placed on top of the glass slide. The ultrasonic drive on the probes is at a frequency of approximately 110 kHz which is the longitudinal resonance frequency. Since the maximum force gauge sampling frequency is approximately 42 Hz, the Chatillon force gauge effectively measures an average cutting force contribution from the ultrasonic drive. The probe tip, during a sonic cycle, sees a fraction of the 2π phase of cutting when the tip is in contact with the substrate. There is also a passive phase of the cycle when it oscillates back to the top position without contact. As the tip moves up and down at 110 kHz, the tip moves a displacement of approximately 38 μm in a 110 kHz period which is approximately 9 μs. This gives an effective

tip velocity of approximately 4.2 m/s. Since the probe is inserted at a velocity of less than 2.6 mm/s, viscous damping forces on the edge of this probe tip would cancel in a time-averaged oscillation cycle. However, the contribution from the active cutting where the tip contacts the substrate contributes to the overall forces felt by the force transducer. As a result, the effective measured force by the force transducer is

$$F_t = F_x - f_o + \gamma V + k_1 \dot{x} + k_2 \dot{x}^2 \tag{2.16}$$

where γ represents a multiplication factor indicating the time the tip is in active cutting mode with the substrate, F_t is the measured force transducer force in milli-Newtons, and V is the PZT driving voltage in volts. With the velocities used in this study, the nonlinear dependence on velocity was not observed, and hence assumed negligible. Additionally, by varying the substrate percent agarose, the elasticity of the substrate can be changed. This affects the viscous damping expression k_1 term but also the tissue reaction force f_o. The expression can be further simplified to

$$F_t = \alpha Y + \beta Y \dot{x} + \gamma V + \delta \tag{2.17}$$

where Y is the substrate percent agarose, which is an indication of the elasticity of the material, $\dot{x}$ is the probe insertion velocity in mm/s, and V is the PZT driving voltage in volts.

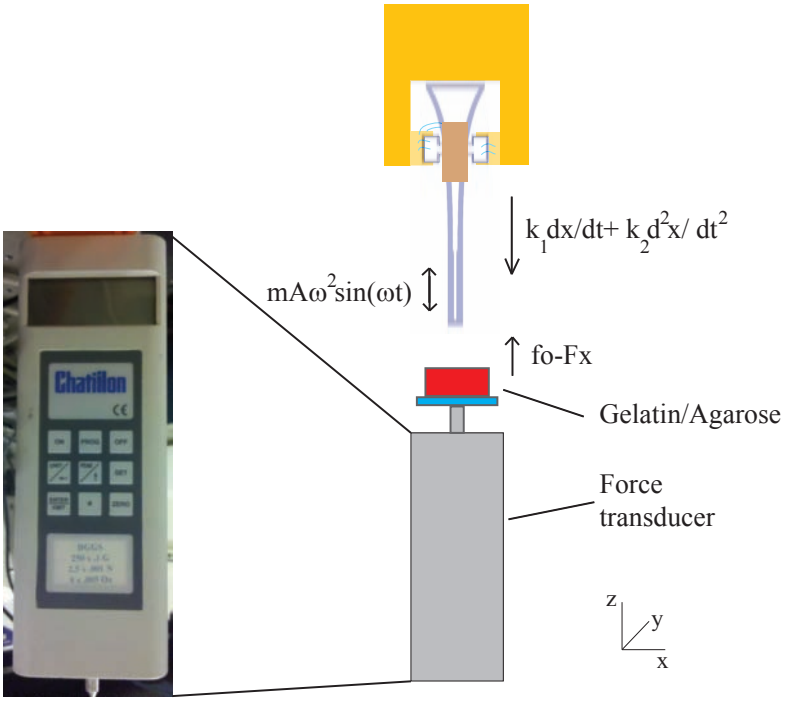

Figure 2.18: Setup for measuring insertion forces with ultrasonically actuated probes.

Effect of insertion velocity, PZT drive voltage, and substrate elasticity

The probe was inserted at various velocities into agarose sitting on the force transducer. By measuring the transducer force during insertion, the force profile in Fig. 2.20 was obtained. A large initial force peak is seen in the force profile from the probe breaking through the substrate surface. As the probe is inserted further into the substrate a constant depth, the shear and damping forces cause the measured forces to increase. Probe motion is then stopped, and the residual force from probe insertion remains.

The elastic modulus of the substrates can be estimated from the initial insertion force peak before the probe breaks through the substrate, much in the same

way AFM tips can be used to estimate substrate elasticity [25]. By observing the measured forces in the force profile prior to the first peak when the probe penetrates the substrate surface, the force versus penetration depth of the probe can be measured. The probe tip is composed of a wedge shape 80 microns long and 100 microns wide. Since biological tissue and agarose substrates are compressible below the area of indentation, the indentation deformation should be less than 10% of the thickness of the substrate to obtain a valid measurement [25]. A Hertzian theory contact model with Sneddon mechanics is assumed for a conical tip penetrating a flat, deformable substrate [26]. This gives a relative Young's modulus of

$$E^* = \frac{\pi}{2}\frac{F tan\theta}{d^2} \tag{2.18}$$

where F is the insertion force, θ is the contact angle of the probe with the substrate, and d is the indentation distance. The Young's modulus of the substrate can be calculated as

$$\frac{1}{E^*} = \frac{1-{\nu_{Si}}^2}{E_{Si}} + \frac{1-{\nu_{ag}}^2}{E_{ag}} \tag{2.19}$$

where ν_{Si} and E_{Si} are the Poisson's ratio and Young's modulus for the probe tip which is made of silicon. Since E_{Si} is approximately 170 GPa, the first term on the right side can be ignored. The terms ν_{Ag} and E_{ag} are Poisson's ratio and Young's modulus for the agarose substrate. Poisson's ratio for agarose can be approximated as equal to 0.5 [25]. The estimated Young's moduluses for the various agarose gels used in this experiment are shown in Fig. 2.19, and are comparable to measurements in the literature [27].

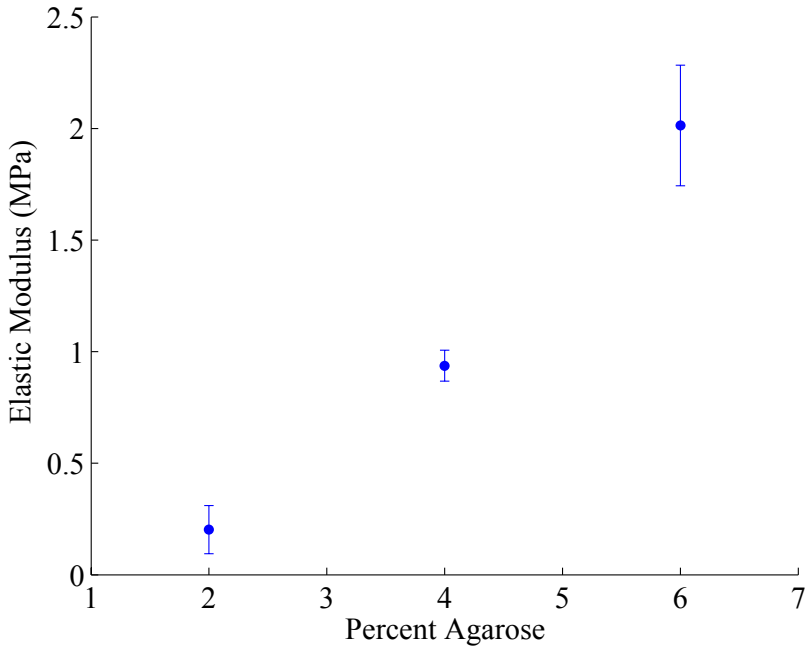

Figure 2.19: Extracted elastic moduluses for various percent agarose substrates.

As shown in Fig. 2.21, the measured force profile is dependent on insertion velocity. As the velocity of insertion increases, the peak force also increases, as expected from the increased viscous damping force. Additionally, as seen in Fig. 2.22, for a given insertion velocity, as the PZT drive voltage increases, the peak force decreases. Additionally, as the substrate elasticity decreases, the peak force increases as seen in Fig. 2.23. For each PZT drive voltage, insertion velocity, and substrate elasticity condition, the insertion profiles and peak forces were measured for three separate insertions and the peak values were averaged. The measured curves approach the sensitivity limits of the force transducer of 1 mN, and errors on the measurements were calculated with the following equation, where m is the mean of the three measurements a, b, and c, where the error on the measurements is 0.5 mN, half of the measurement sensitivity.

By extracting the peak forces from the data, and fitting the data using a

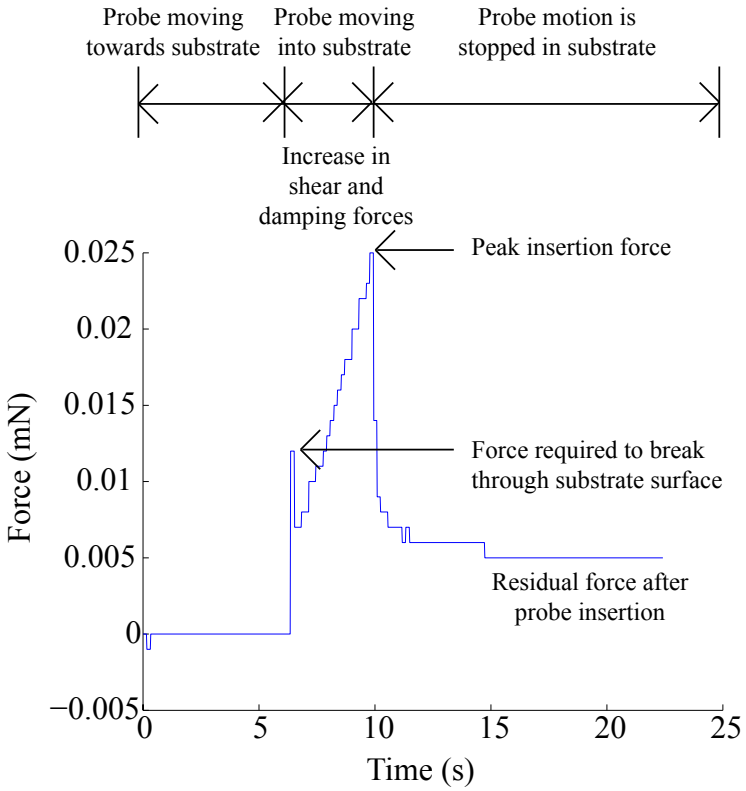

Figure 2.20: Measured insertion force profile for ultrasonic horn probe driven at 20 Vpp and inserted into 4% agarose at 2.4 mm/s. As the probe is first moved towards the substrate, no forces are measured. A small initial peak occurs as the probe breaks through the surface of the substrate. The forces steadily increase as the shear and damping forces increase. Finally, probe motion is stopped in the substrate, and damping forces dependent on the insertion velocity disappear, revealing the residual force in the substrate.

nonlinear regression χ-squared minimization function, the following fit was obtained:

$$F_t = (5.90+/-0.52)Y+(1.18+/-0.26)Y\dot{x}-(0.30+/-0.18)V-(3.93+/-0.97) \quad (2.20)$$

The averaged force transducer data plotted against the fit for each variable is

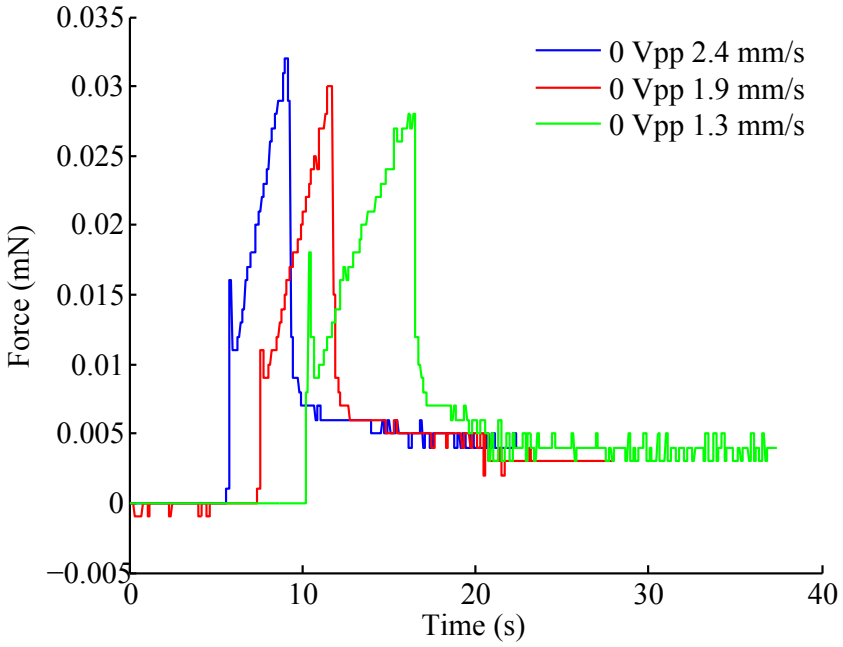

Figure 2.21: Measured insertion forces in 4% agarose for indicated probe insertion velocities with a PZT driving voltage of 0 volts. As the velocity increases, the peak force also increases.

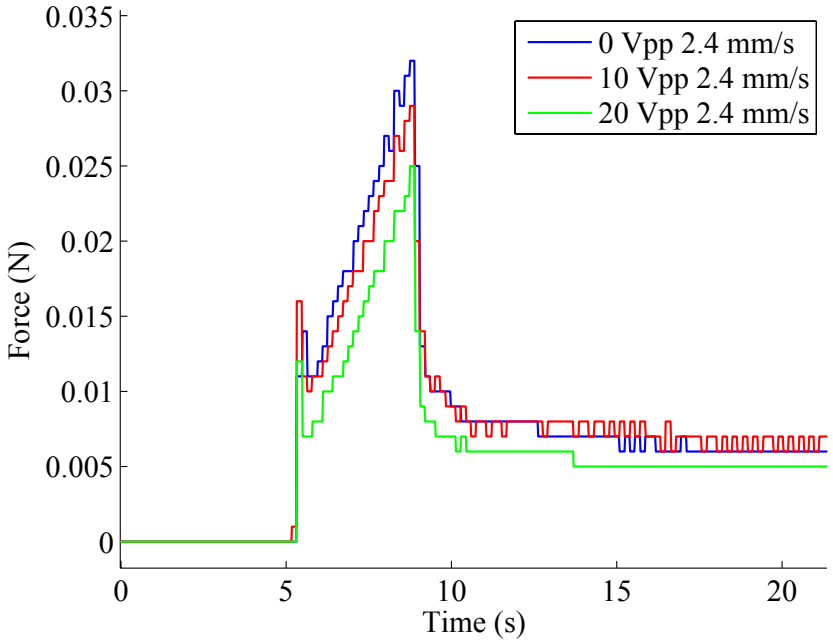

Figure 2.22: Measured insertion force curves for PZT drive voltages of 0, 10 and 20 volts in 4 % agarose and with an insertion velocity of 2.4 mm/s.

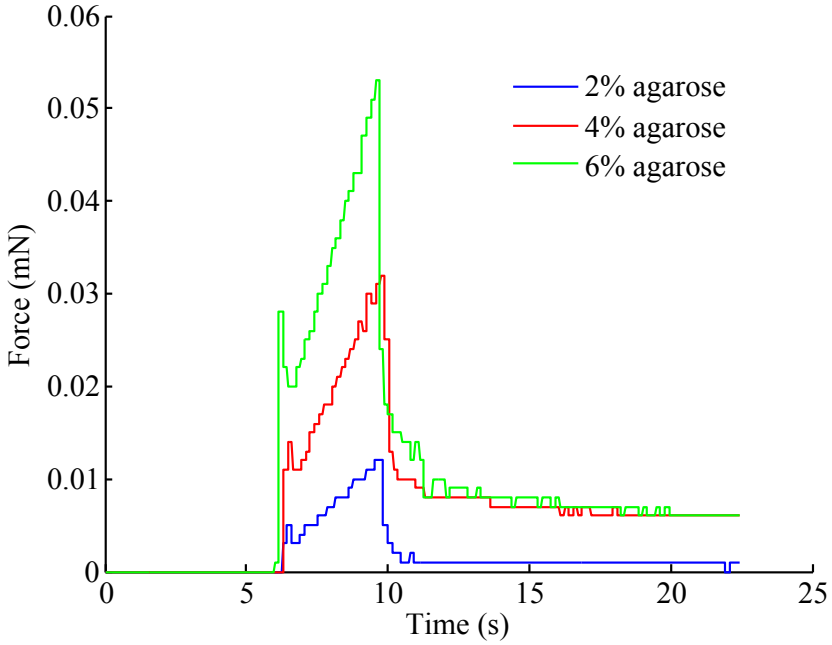

Figure 2.23: Measured insertion force curves for 2%, 4%, and 6% agarose with an insertion velocity of 2.4 mm/s and a PZT drive voltage of 0 volts.

shown in the following figures, with dependence on PZT drive voltage shown in Fig. 2.24, dependence on percent agarose substrate shown in Fig. 2.25, and dependence on insertion velocity shown in Fig. 2.26. The data indicates that by minimizing insertion velocity and maximizing PZT drive voltage, the forces felt by a given substrate can be minimized.

2.5 Conclusions and Future Directions

In this section, the design and fabrication of ultrasonic horn probes has been introduced. Strain gauges and electrodes can be integrated with the horn structure to allow monitoring of electrical and mechanical signals. Additionally, a model governing the insertion forces of ultrasonic horn probes is presented.

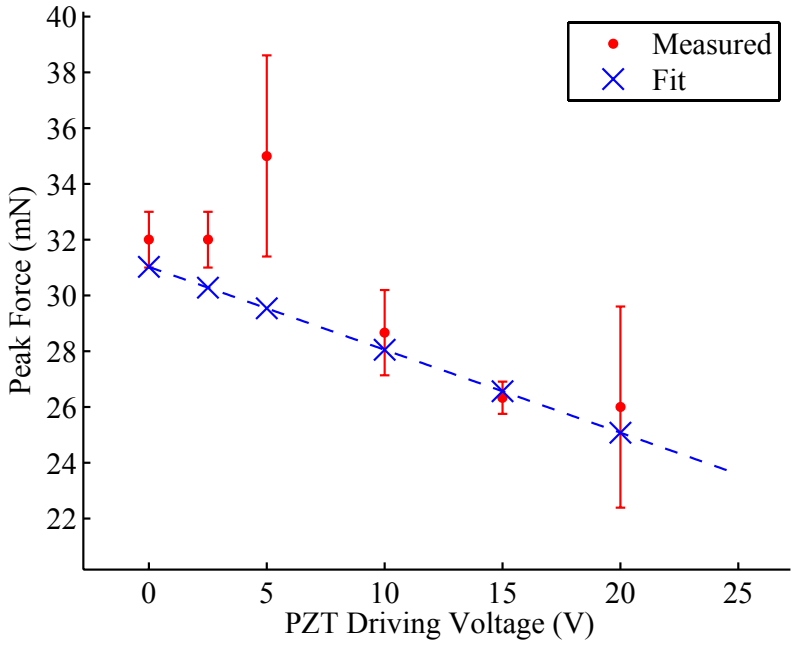

Figure 2.24: Measured insertion forces for various PZT drive voltages with a PZT driving voltage of 0 V and insertion velocity of 2.4 mm/s.

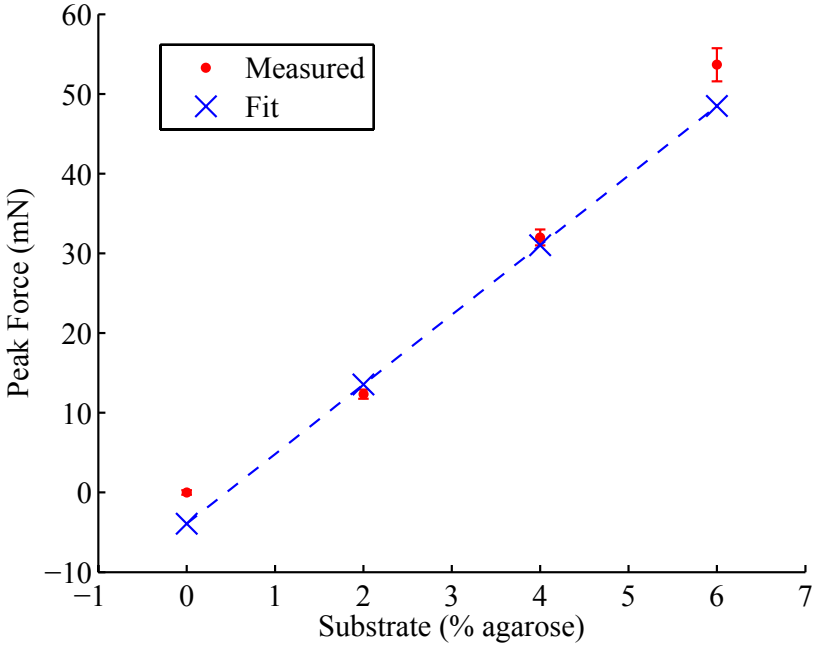

Figure 2.25: Measured insertion forces for various percent agarose substrates with a PZT driving voltage of 0 V and insertion velocity of 2.4 mm/s.

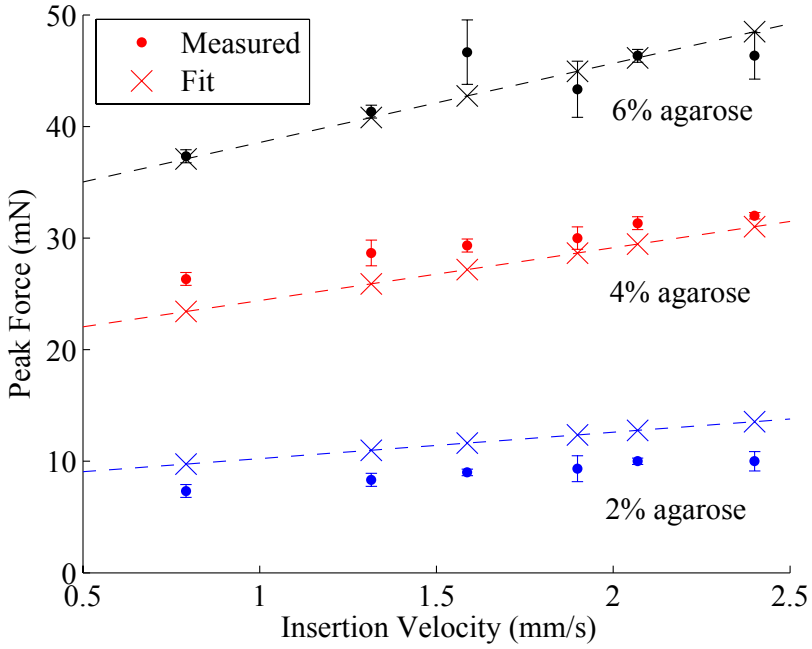

Figure 2.26: Measured insertion forces for various probe insertion velocities with no ultrasound and substrates of 2% (lower points), 4% (middle), and 6% (upper) agarose.

This model governs the effect of PZT driving voltage, probe insertion velocity, and substrate elasticity on insertion force. The measured results and model agree fairly well. For the measured forces versus PZT driving voltage, a linear model is assumed. From the measured data, it may be possible that the insertion forces remain constant until a large enough driving voltage is achieved to reduce the insertion forces. The force reduction properties of ultrasonic horn probes can be further investigated for scaling to higher and lower resonance frequencies. With a low enough resonance frequency, the oscillating forces may be able to be monitored during substrate insertion to fit the exact parameters presented in Nabibekov's model [24]. With the currently presented model, silicon probes can be designed for a variety of applications with different tissue elasticities including cardiac and neural tissue, and maximum forces felt by a tissue during probe insertion can be estimated.

CHAPTER 3

ULTRASONIC HORN PROBES FOR STUDY OF CARDIAC ARRHYTHMIA ONSET IN 3D

3.1 Motivation

One of the leading causes of death in the industrialized world is sudden cardiac death linked to ventricular fibrillation (VF). In VF, the cells in the heart beat asynchronously and are not able to contract the ventricles sufficiently to pump blood to the body. The mechanisms behind its onset are not fully understood. With an improved understanding of its onset, better tools can be developed to treat and prevent lethal arrhythmias. While it is known that VF is often preceded by ventricular tachycardia or other rapid heart rhythms, the reentry mechanisms leading to this arrhythmia are still being studied [28]. Theory and experiments have demonstrated that rapid cardiac rhythms may precipitate cardiac alternans, characterized by alternating long and short action potential durations. Additionally, electrical alternans can give rise to the spiral waves of excitation that are thought to underlie VF [29, 30]. Alternans typically arises from a steeply sloped action potential (APD) restitution, the relation between diastolic interval and the action potential duration. High resolution transmural characterization of this relation, which currently is not available, could provide valuable insights regarding the mechanisms for VF.

Previous experimental observations of electrical excitation patterns prior to and during VF have been conducted using voltage sensitive dyes [29, 30], which can provide a meaningful picture of electrical wave propagation, but one that is limited to the tissue surface. Intramural multisite optical recordings have been

proposed and developed, but the demonstrated optical system does not allow calibration of fluorescence signals to electrical potentials [31].

While there are 2D electrical models that predict electrical patterns on the surface of the ventricles, experimental data is lacking in 3D through the 5-10 mm ventricle thickness. With knowledge of the propagation of action potentials transmurally and laterally, 3D propagation models could be refined and validated. Additionally, the efficacy and efficiency of Implantable Cardioverter Defibrillators (ICDs), which are used to treat VF could potentially be improved with a better understanding. ICDs function by delivering algorithmically-determined electric shocks, and have shown promise in preventing sudden cardiac death, by delivering large electrical shocks [32]. However, these devices have significant drawbacks, including tissue damage and pain. The information gained from an improved understanding of cardiac fibrillation in 3D may be valuable in developing and implementing new lower energy pacing algorithms to prevent VF, such as adaptive diastolic interval control (ADIC) and extended time-delay autosynchronization (ETDAS) [33, 34].

The difficulty with gathering data in 3D through cardiac tissue lies with its tough and firm composition. As a result, it is difficult for traditional (10-100 μm diameter, 5 mm long) brittle silicon electrodes to penetrate cardiac tissue and avoid silicon fracture. Additionally, it is difficult for flexible substrate based electrodes to penetrate cardiac tissue. As introduced in the last chapter, our group has previously demonstrated the capability to reduce penetration force with silicon ultrasonic horn probes and additionally record action potentials using these probes from cardiac tissue transmurally [2]. These probes offer an important advantage over traditional neural recording silicon electrodes in that

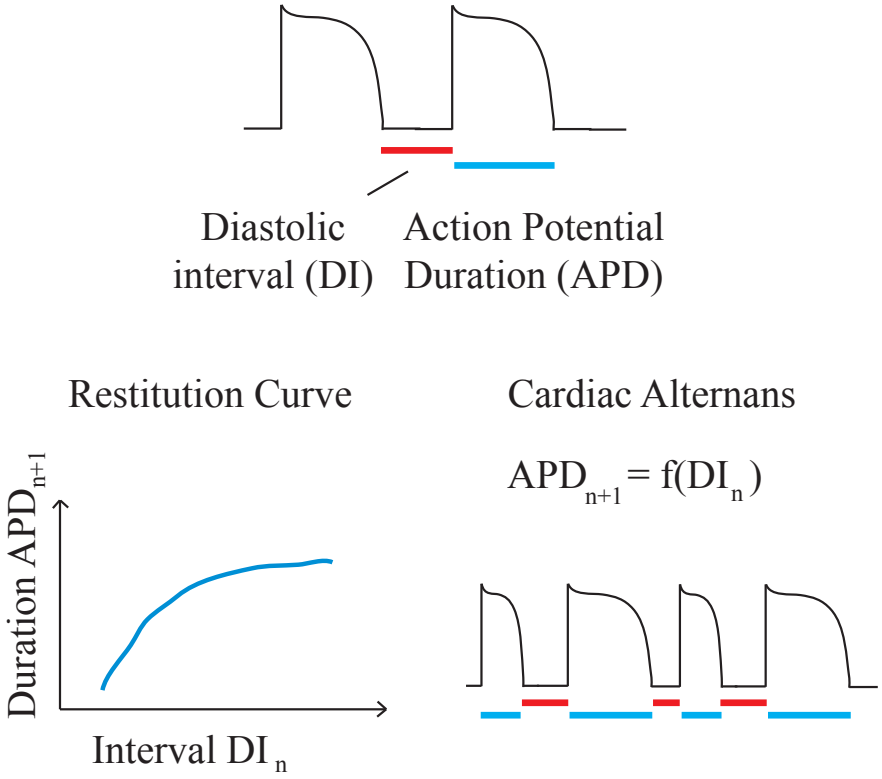

Figure 3.1: Diagrammatic representation of restitution relation model of cardiac tissue, where the action potential duration (APD) is a function of the previous diastolic interval (DI).

the ultrasonic drive allows penetration of tough cardiac tissue without causing silicon fracture [35]. In this section, data collected from multichannel and multisite recordings with ultrasonic horn probes are presented that demonstrate 3D action potential propagation prior to ventricular fibrillation.

3.2 Cardiac alternans model for ventricular fibrillation onset

One proposed pathway leading to ventricular fibrillation (VF) is the development of cardiac alternans, as shown in Fig. 3.1, which is characterized by alternating long and short action potential durations. The cardiac restitution relation defines the relation between the cardiac action potential duration and the preceding diastolic interval, as shown in Fig. 3.1. This relation can be an indicator of likelihood of cardiac alternans and ventricular fibrillation. At short diastolic intervals, the steep slope of the curve allows small variations in diastolic interval to lead to large variations in APD which is characteristic of cardiac alternans [36]. Ectopic beats during cardiac alternans can lead to re-entry and VF. With 2D voltage-sensitive dye recordings of cardiac alternans onset on the surface of the heart, it has been observed that alternans can be concordant where all part of the tissue are in the same phase, or discordant where the phase varies spatially over a 1-cm scale on the surface of the heart [37].

Acute myocardial ischemia has been shown to be highly correlated with malignant ventricular arrhythmias [38], motivating study of the mechanisms linking ischemia to arrhythmias. The effects observed with ischemia have been classified into two stages. In the initial stage, there is increase in extracellular potassium and electrical depolarization [38]. After many minutes, the second phase occurs with electrical uncoupling, loss of intracellular potassium, and ischemic contracture [38]. With transmembrane potential recording, decreased action potential durations, amplitude, upstroke velocity, and resting potential have been observed in intact pig hearts [39]. The types of arrhythmias that occur during the two stages are termed immedicate ventricular arrhythmias (IVAs) and delayed ventricular arrhythmias (DVAs) [40]. Both are thought to arise from

re-entry mechanisms.

While phenomenologically these electrical, chemical, and mechanical effects have been observed, the interrelation in leading to arrhythmias is not well understood. One hypothesis is that reentry related to premature ventricular contractions can lead to arrhythmias [41]. Conduction delay differences longer than the refractory period of nearby cells could contribute to the development of re-entry in the tissue during ischemia [41]. Other studies have observed alternation and 2:1 action potential responses concurrent with the onset of ventricular arrhythmias [39]. With alternans, ectopic beats could lead to ventricular fibrillation or ventricular tachycardia [37].

Further information on the distribution of activity changes transmurally would be helpful. Models have sought to investigate re-entrant mechanisms on the epicardium, and also ones arising from ischemia-induced heterogeneities that exist transmurally [42]. Experimental studies have investigated the effect of ischemia on action potentials in the epicardium and endocardium, demonstrating a greater impact on epicardium versus endocardium in terms of action potential amplitude reduction, prolonged activation time, and decreased maximum dV/dt [43]. However, experimental data of the distribution of these heterogeneities transmurally would be very helpful to understand how ischemic conditions can contribute to arrhythmias.

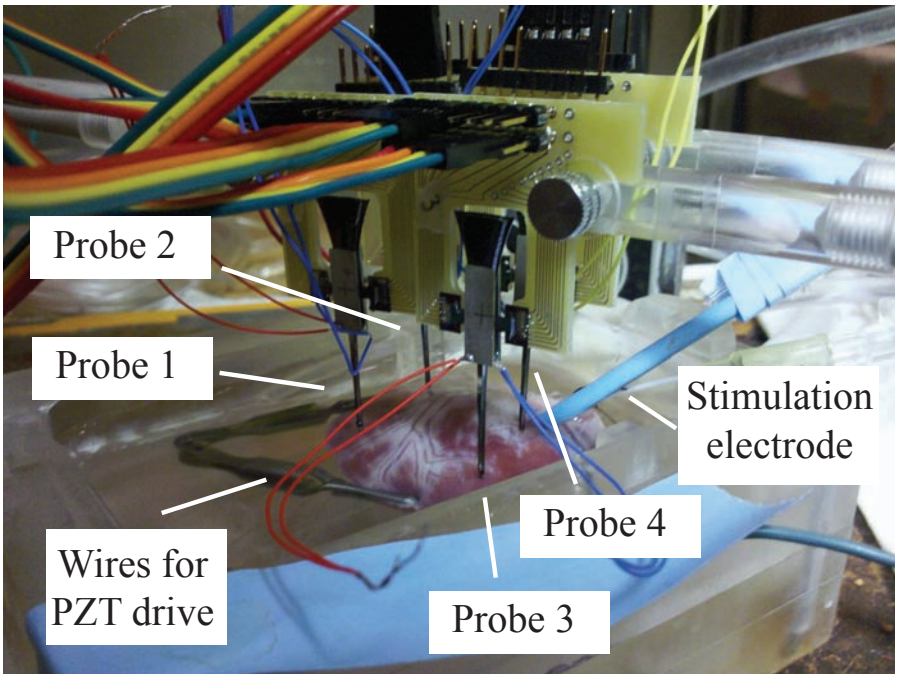

Figure 3.2: Four ultrasonic horn probes inserted in canine left ventricle tissue to record cardiac action potentials through ischemia.

3.3 Multi-probe recordings of cardiac action potentials during cardiac ischemia

Cardiac action potentials at many different locations throughout the tissue can be monitored simultaneously with the ultrasonic horn probes, as shown in Fig. 3.2. The probes have five electrodes on each tine at the end of the probe. The tines are 9 mm long with each electrode spaced 2 mm apart. The two tines are 500 μm apart laterally, as shown in Fig. 3.3.

Cardiac monophasic action potentials recorded with the silicon horn probes are shown in Fig. 3.4a. Extracellular action potentials resemble ideal monophasic action potentials soon after ultrasonic insertion, but degrade over time. In some cases, ideal action potentials are observed at some recording sites while

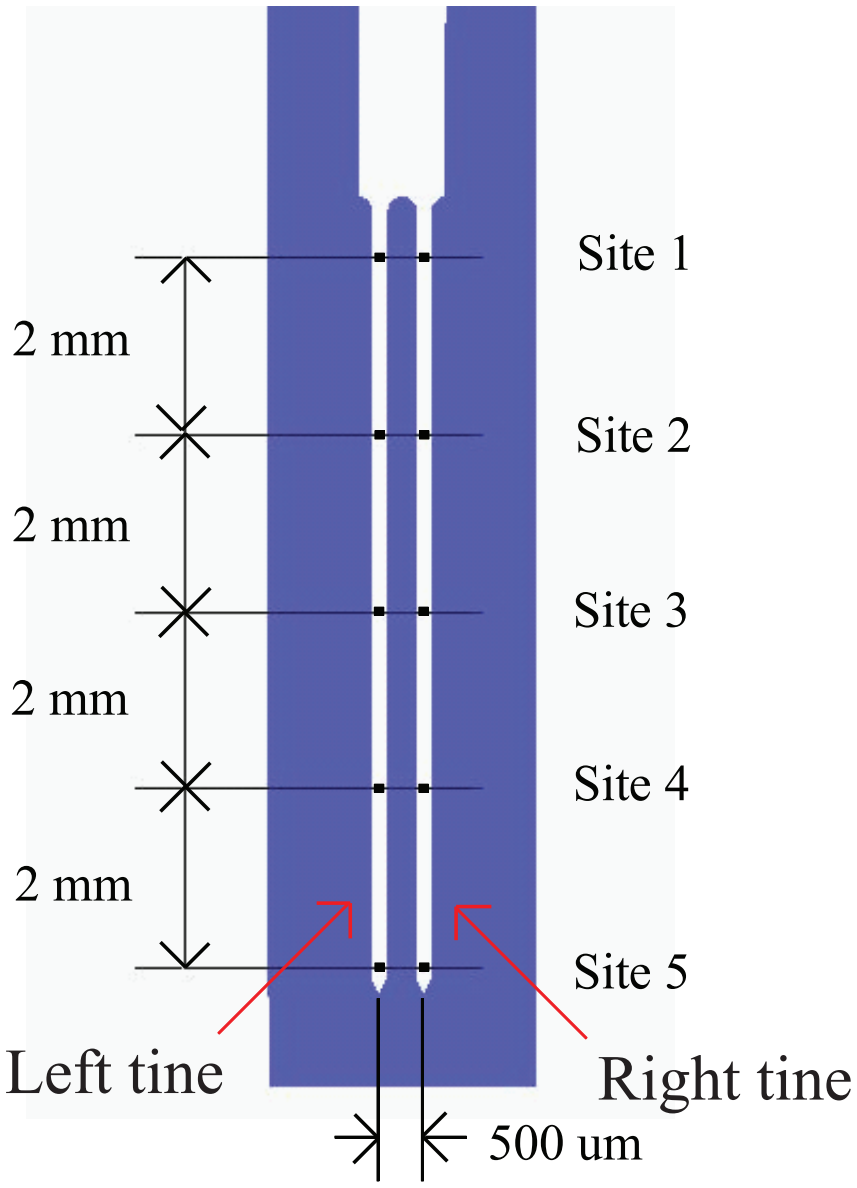

Figure 3.3: Probe recording site locations.

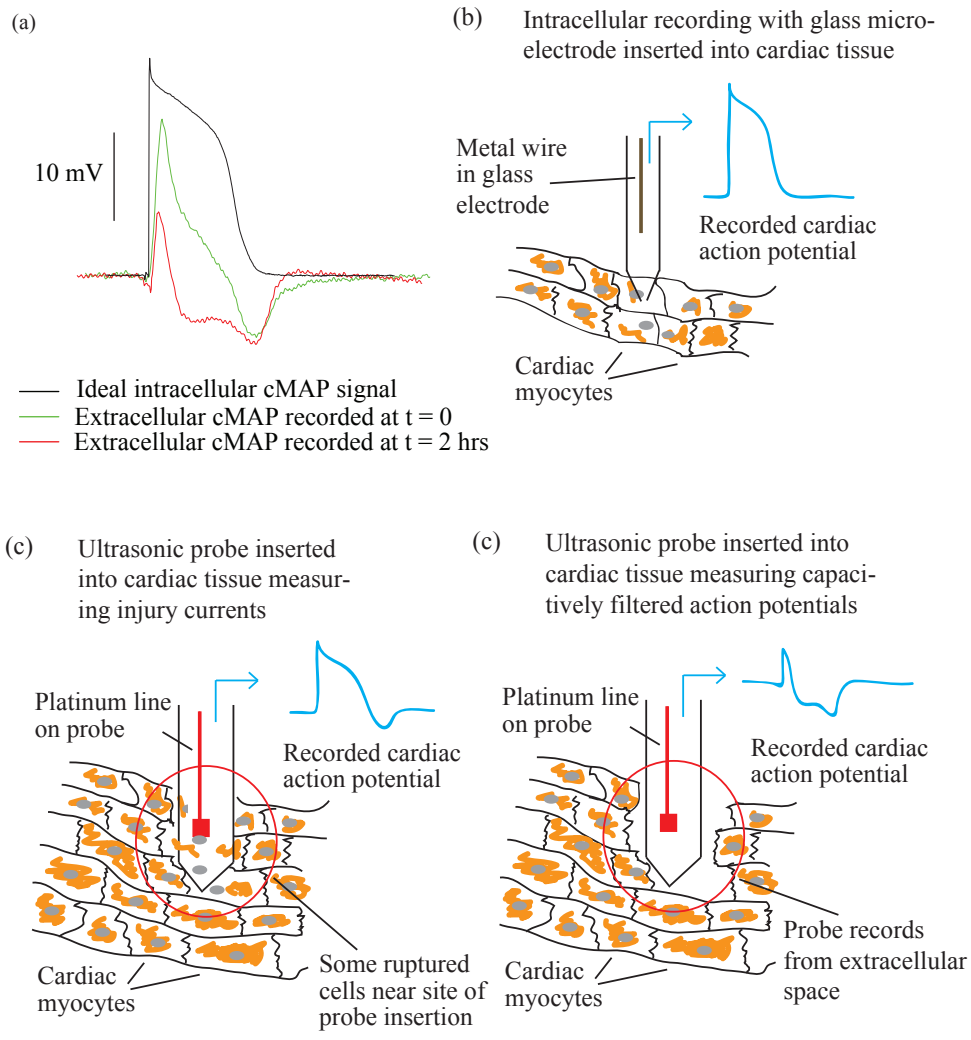

Figure 3.4: (a) Change in recorded cardiac action potential morphology through time (adapted from [10]). (b) Hypothesized effect of probe insertion on cardiac myocytes and effect on signal morphology.

degraded action potentials are observed at other sites just after probe insertion. It is hypothesized that the ultrasonic probe insertion causes some cell rupture, as shown in Fig. 3.4b, sometimes allowing for initial coupling with cell interiors and the currents that generate the initial action potential morphologies. As time progresses, the morphology of the action potentials appear to be a differentiated biphasic version of the initial signals. It is hypothesized this transition in morphology could arise from the capacitive double layer of the cell membranes.

3.3.1 Multiplexer circuit for 32-channel recording

To record from many channels simultaneously, a multiplexing circuit was developed. The data acquisition device used (National Instruments BNC-6259) has a limited number of input channels of 16, though the total acquisition rate possible is 1.25 MS/s. The developed multiplexing circuit uses four 8x1 multiplexer chips (ADG508FBNZ), which are controlled using digital outputs from an Arduino Mega-2560 microcontroller board. The microcontroller could also be used to achieve the multiplexing, but the use of separate multiplexer chips allows for lower noise and better noise isolation between the microcontroller and analog signals from the biological setup. The multiplexing circuit is shown in Fig. 3.8. From Fig. 2.8, the charge transfer resistance on the microfabricated silicon probes is 5.79 GΩs. To ensure sufficient signal quality, the input impedance of the stage following the probes should be at least 100 GΩ. The multiplexer does not have a sufficiently large input impedance, so a unity gain buffer stage with an input impedance of 100 GΩ is used, realized using the LT1113 chip. The equivalent circuit is shown in Fig. 3.5. The input transfer function is then given by the expression

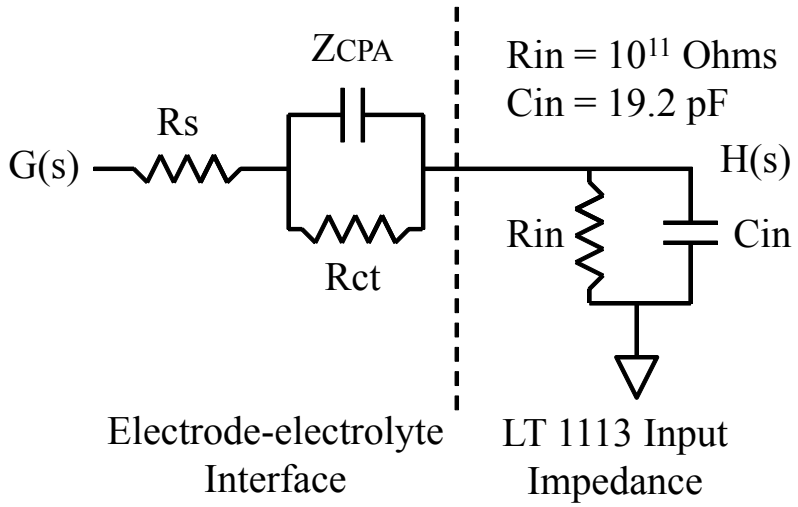

Figure 3.5: Equivalent circuit of electrode-electrolyte interface and LT 1113 input.

$$H(s) = \frac{\frac{Rin}{1+j\omega RinCin}}{\frac{Rin}{1+j\omega RinCin} + Rs + \frac{ZcpaRct}{Zcpa+Rct}} G(s) \tag{3.1}$$

The magnitude of the transfer function is plotted in Fig. 3.6. It is clear that the magnitude of the transfer function varies by 2.45% over the region from 0.01 to 1 kHz.

To evaluate the signal frequencies of interest within a cardiac signal, a cardiac signal was recorded at a 10 kHz sampling rate. The signal is low pass filtered with various cutoff frequencies and the action potential duration and diastolic intervals between the filtered signal and unfiltered signals are compared, as shown in Fig. 3.7. With a 150 Hz low pass filter, the difference between the action potential durations for five unfiltered and filtered signals is 0.14 milliseconds, indicating a percent different of 0.06%. With this small change, it is

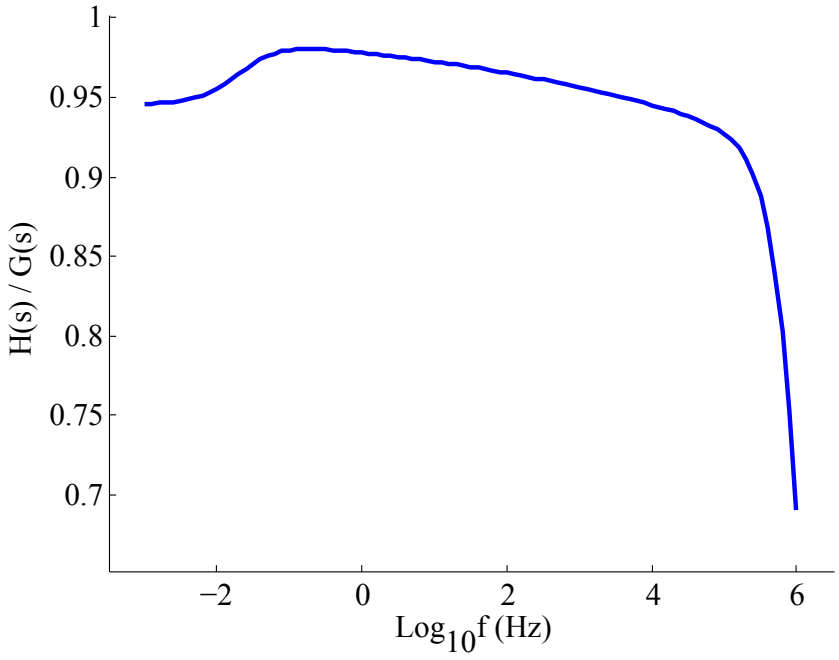

Figure 3.6: Transfer function of input to unity-gain amplifier.

justified to sample the signals at 1 kHz and low pass filter the signals at 150 Hz to extract action potential durations.

Thirty-two inputs are fed from the input stages to the multiplexer, which uses four 8x1 multiplexers to provide 4 outputs. The microcontroller clock speed is 16 kHz, which is aligned to the data acquisition sampling. Since the multiplexers are switched every two clock cycles, two samples from a given channel are taken per channel switching. As there are timing and capacitive charging effects, the sample is taken which provides a non-distorted recording of the input signals. The code used to control the Arduino Mega-2560 is shown in Appendix A. To allow for a reference indicating which multiplexed output corresponds to which probe channel, one channel is grounded for each multiplexer.

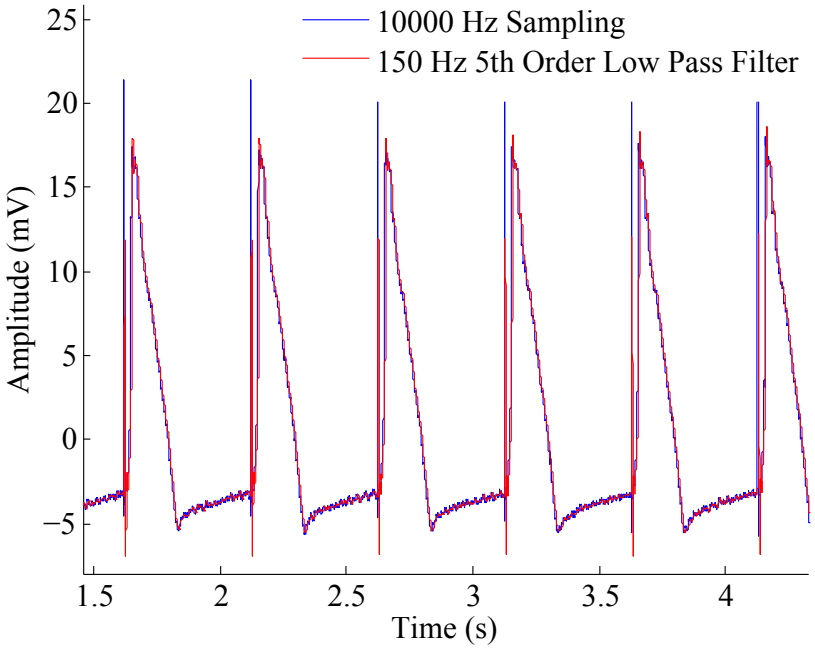

Figure 3.7: Unfiltered and 150 Hz low-pass filtered cardiac signals.

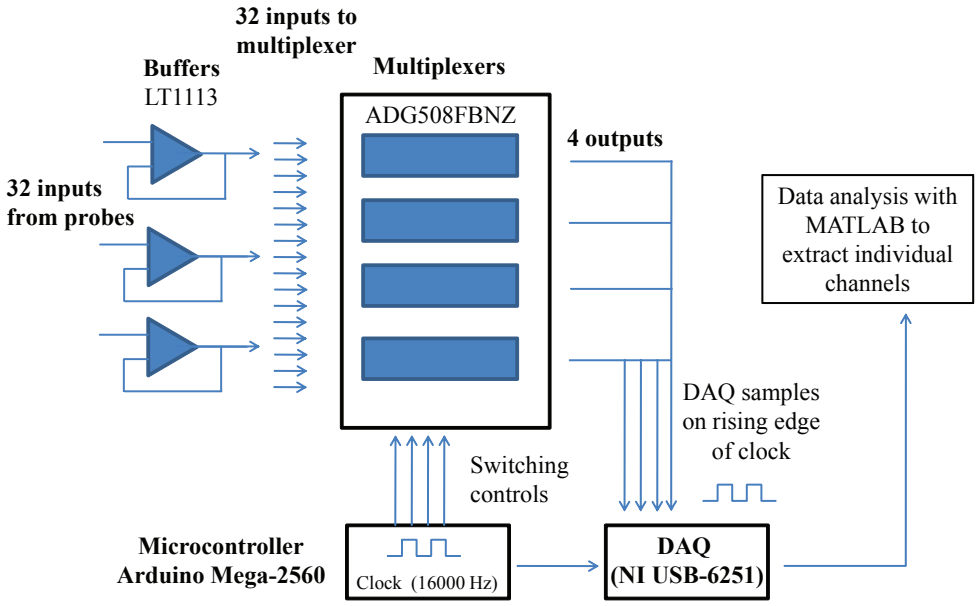

Figure 3.8: Multiplexing circuit used to extract data from 32 channels with a sampling rate of 1 kHz per channel.

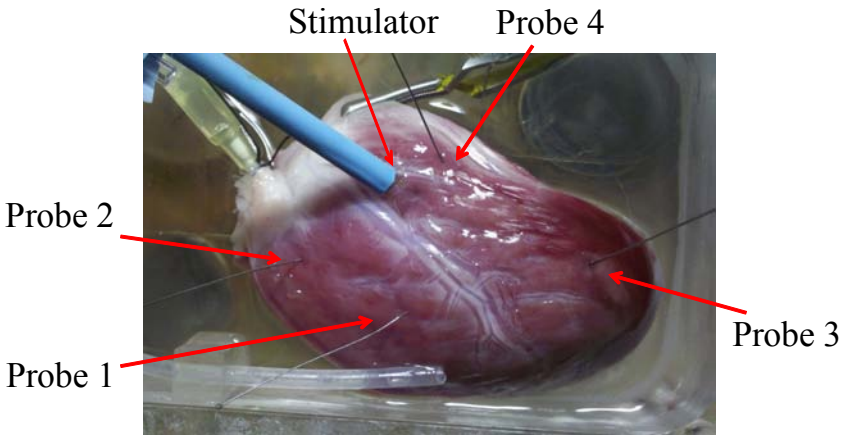

Figure 3.9: Recording locations of ultrasonic horn probes inserted in canine left ventricle tissue to record cardiac action potentials through ischemia.

3.3.2 Multichannel recordings

The electrode recording sites are distributed through the tissue, as shown in Fig. 3.9. Using a custom MATLAB code, the action potentials are extracted for each electrode site, and referenced to the multiplexer channel set to ground. The recordings shown in Fig. 3.10 are obtained for one probe. The recordings show the distribution of action potentials throughout the depth of the tissue.

To analyze the recordings, the signals are first cleaned up by filtering and averaging. As shown in the previous section, 150 Hz low pass filtering of the signals provided an action potential duration difference of 0.14 seconds, indicating the small degree of filtering of the actual signal with a 150 Hz low pass filter. After 150 Hz low pass filtering, random noise can be further removed from the signals by averaging multiple action potentials together. Since cardiac alternans

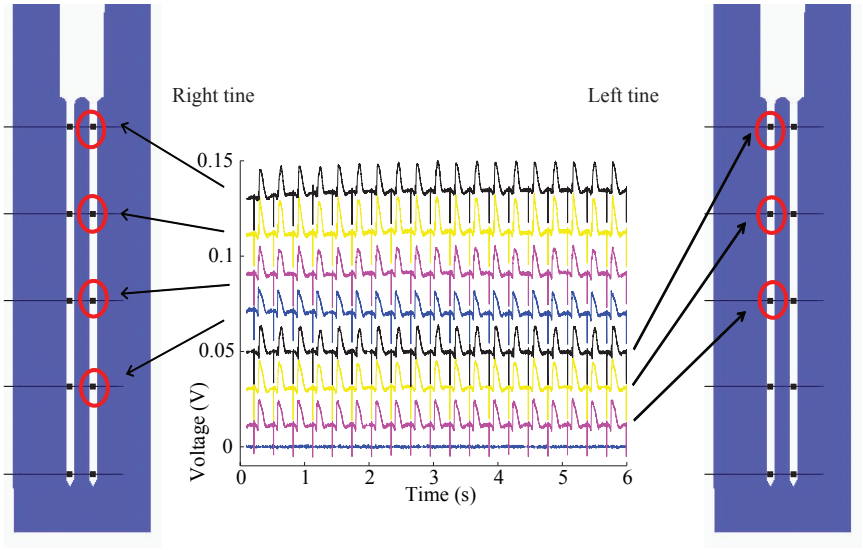

Figure 3.10: Multiplexed recording of 8 channels from 1 probe.

is present in some of the recordings, alternate action potentials are set aside for averaging to not distort the alternans waveforms. With this alternating pattern, five segments of two consecutive action potentials are taken from each recording. Action potentials from these time segments are averaged together. The raw signal and resulting filtered and averaged waveforms are shown in Fig. 3.11, where the two action potentials in the lower trace are taken as the representative recordings from each timepoint. As each of the two action potentials in the lower trace exhibit different properties, most notably action potential amplitude, quantities are assessed separately for each. The two action potentials are termed action potential one and two in the next sections.

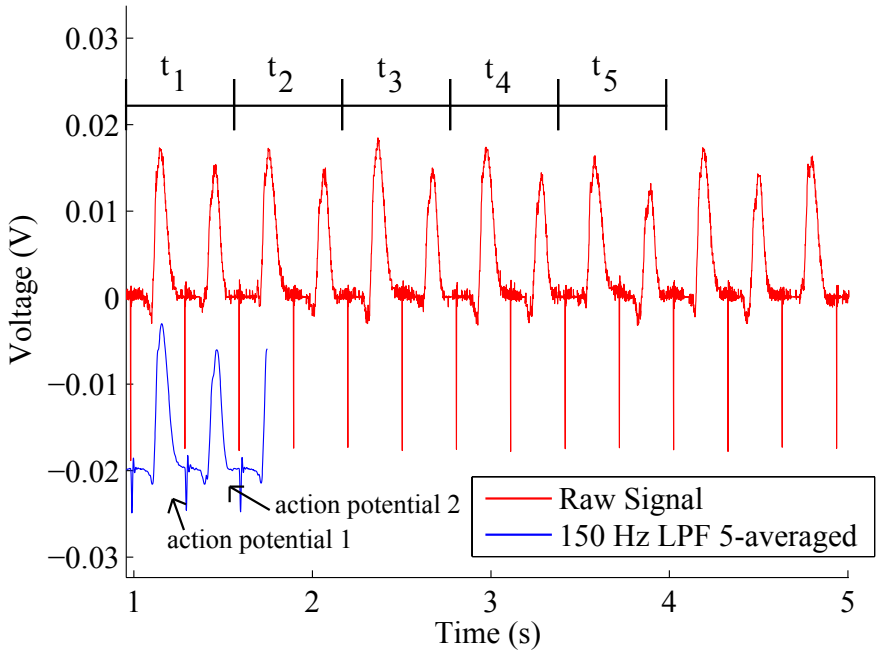

Figure 3.11: Raw signal recording and filtered signal for two consecutive action potentials during ischemia. Five consecutive time segments (t_1 through t_5 are averaged together and filtered to produce the lower trace. The signals have been DC offset for ease of viewing. Cardiac alternans is apparent in the recordings with alternating long and short action potentials, which are labeled action potential 1 and 2.

3.3.3 Change in action potential morphology through ischemia

Changes in action potential morphology with ischemia or conditions imitating ischemic effects have been studied in epicardial and endocardial cells [43]. These studies demonstrate that the endocardium is less susceptible to action potential changes than epicardium, possibly due to the presence of Purkinje cells in the endocardium. In the current experiments, canine ventricles from two dogs were used for testing the effects of ischemia on action potential characteristics. Four probes were used to record from several locations throughout the tissue. The recording locations are as shown in Fig. 3.9 for dog 1. The pacing

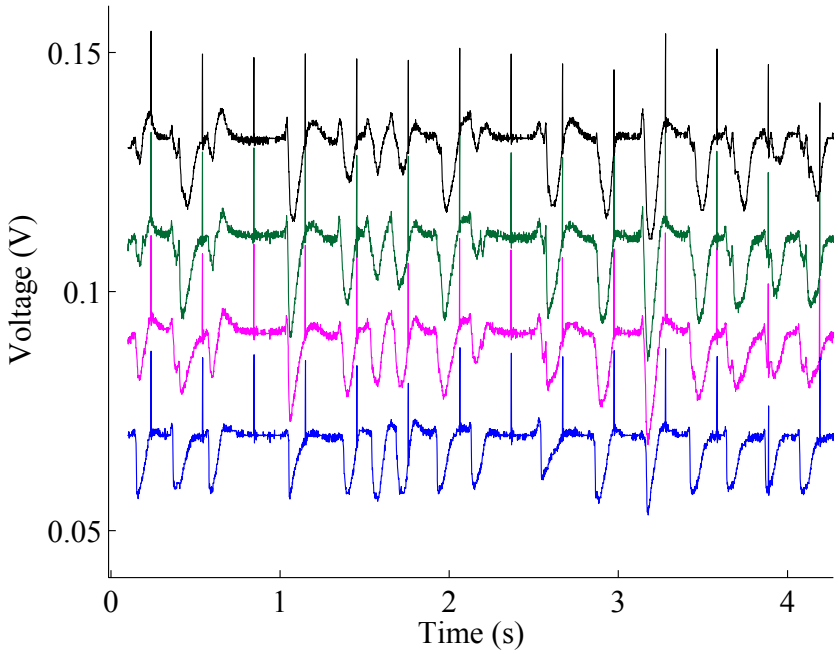

Figure 3.12: Polymorphic ventricular tachycardia of canine left ventricle after 123 seconds of no perfusion. The action potentials at the top epicardial electrode, and electrodes 2 mm, 4 mm, and 6 mm into the depth of the tissue are shown. The traces are epicardial on the top to endocardial on the bottom. The traces are DC offset for ease of viewing.

protocol for dog 1 starts with normal perfusion of the canine ventricle with 500 ms cycle lengths and 2 ms duration current pulses at t = -200 seconds, followed by 400 ms cycles at t = -100 seconds, then 300 ms cycles at t = 0 seconds. At t = 0 seconds, perfusion is turned off. In dog 1, the dog experienced polymorphic ventricular tachycardia after 123 seconds of ischemia with pacing with 300 ms cycle lengths and 2 ms stimulus pulses. The recorded waveforms are shown in Fig. 3.12 for four sites through the depth of the tissue.

Action potential recordings from before polymorphic ventricular tachycardia indicate that the epicardial sites have more altered action potentials than the endocardial sites, as seen in Fig. 3.13. Additionally, the maximum rate of volt-

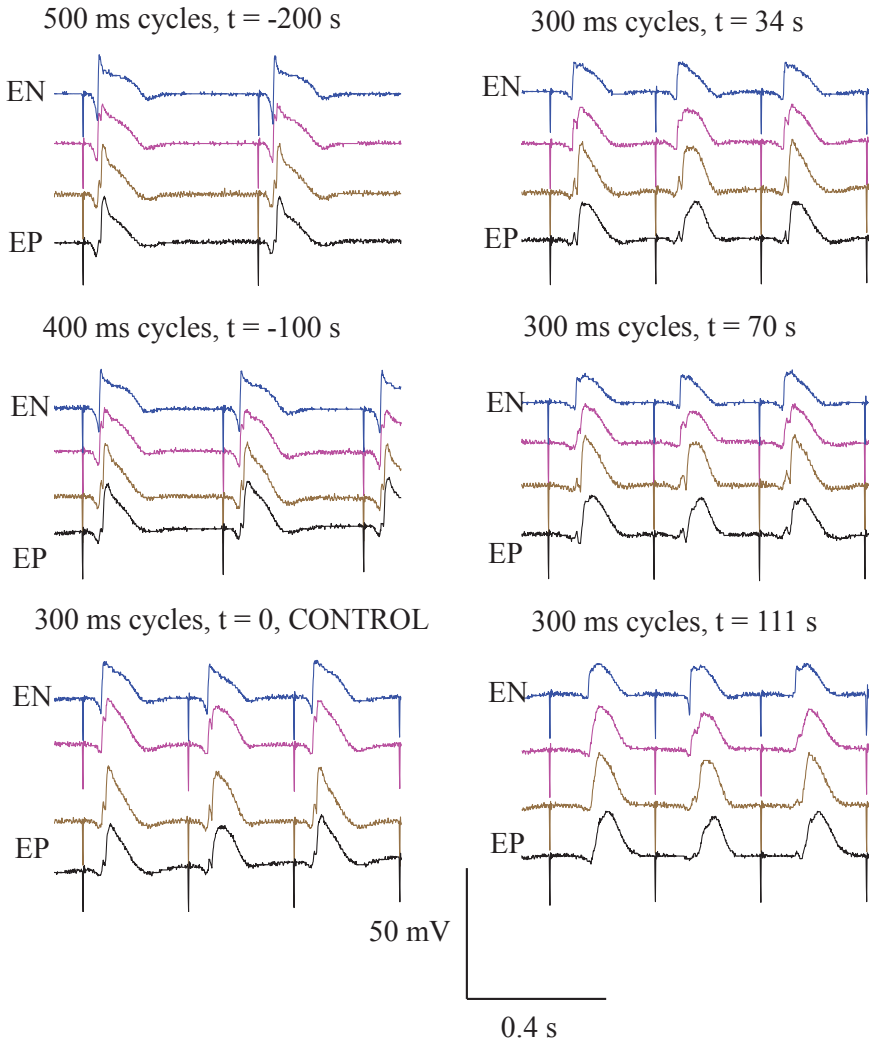

Figure 3.13: Change in action potential characteristics over time with no perfusion for Probe 4.

age change dV/dt appears to decline over time with no perfusion. The dV/dt also alternates during cardiac alternans. It is evident that there is an increase in the stimulus activation time and change in action potential duration with ischemia, both of which are quantified further in the following sections.

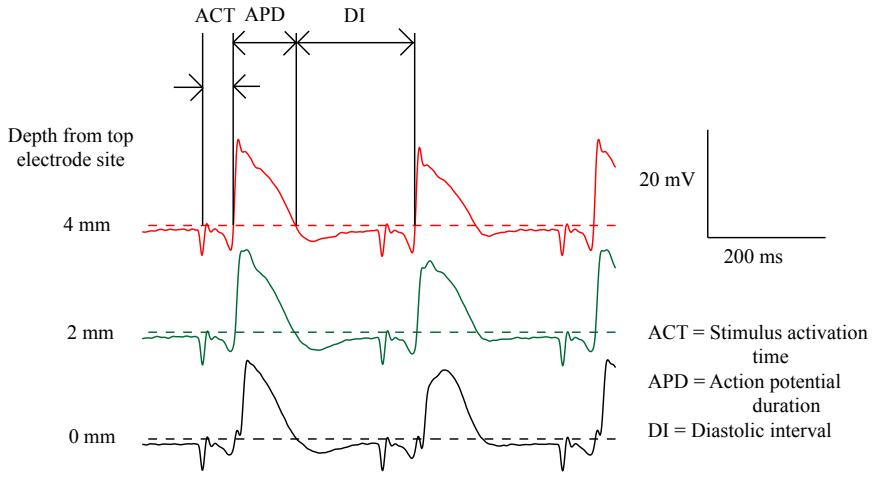

Figure 3.14: Action potential waveforms at three depths within the tissue during normal perfusion. The stimulus activation time, action potential duration, and diastolic interval can be estimated as shown.

Change in stimulus activation time with ischemia

The activation time (ACT) can be estimated as the time between the stimulus artifact and the upstroke peak of the action potential [41]. As mentioned previously, the signals recorded with the silicon microprobes sometimes exhibit a morphology characteristic of capacitive filtering. To analyze such recordings and extract action potential parameters of interest, a thresholding technique can be used to determine action potential durations and activation times. The method for estimating activation time (ACT), action potential duration (APD), and diastolic interval (DI) is shown in Fig. 3.14.

As mentioned in the previous section, representative plots of two consecutive action potentials are extracted for each recording. The activation times during ischemia for the first action potentials for each set were measured and are as shown in Fig. 3.15. Though cardiac alternans is present in many of the record-

ings, the activation times for the first and second action potentials are similar, as shown in Fig. 3.16 for Probe 4 and Fig. 3.17 for Probe 2. The activation delay increases with ischemic conditions, indicating conduction changes in the tissue. Transmurally, activation times for action potentials at all depths increase over time, but not completely uniformly. Fig. 3.18, Fig. 3.19, and Fig. 3.20 show the activation times through the tissue depth during normal perfusion, and at t = 70 and t = 110 seconds for Probes 4, 2, and 1, respectively. For Probe 4, epicardial sites experience a longer delay than endocardial sites. For Probe 2, some epicardial and endocardial sites experience a longer delay than intermediate sites. For Probe 1, endocardial and epicardial sites experience shorter delays than intermediate sites.

It is apparent there are heterogeneities in conduction delay which are present both laterally through the tissue and transmurally through the depth of the tissue. From Fig. 3.18, the epicardial sites exhibit a much larger increase in activation in time than the endocardial sites. Additionally, from Fig. 3.19, it is apparent that heterogeneities exist laterally as well between the left tine and right tine which are spaced 500 μm apart.

Effect of Tissue Reperfusion on Activation Delay

In the second dog heart preparation, the effects of reperfusion on activation delay are investigated. Perfusion is turned off at t = 0 and restarted at t = 530 seconds. The activation delays in dog 2 are shown in Fig. 3.21. It is apparent that the stimulus interval delay decreases after perfusion is turned back on, and takes approximately 70 seconds for the activation delays to return to their original values.

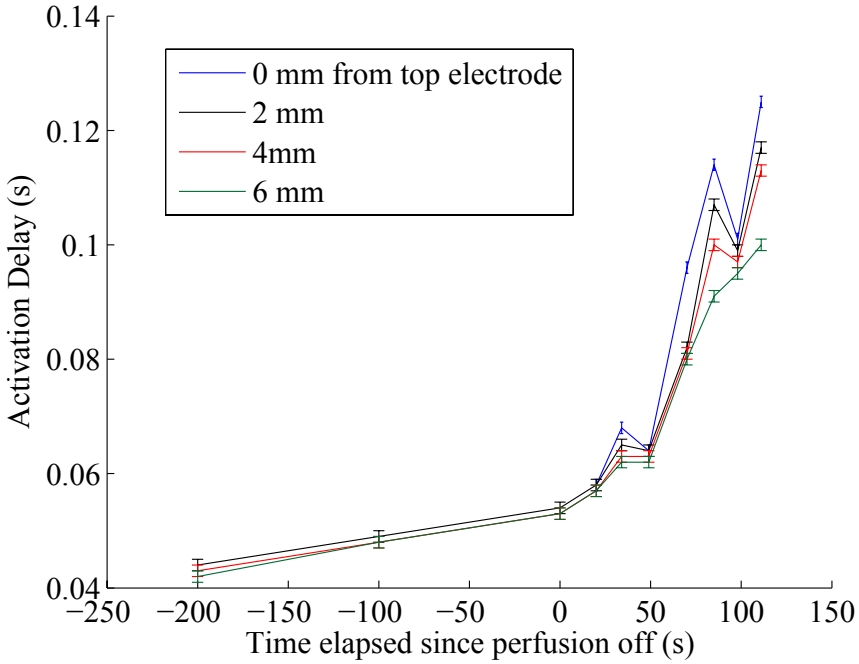

Figure 3.15: Change in stimulus activation time (ACT) over time for Probe 4 electrodes at depths of 0 mm, 2 mm, 4 mm, and 6 mm relative to the top epicardial electrode site.

Change in Action Potential Durations Through Ischemia

Previously, a decrease in action potential duration with increased time in ischemic conditions has been observed for epicardial and endocardial tissue. The action potential durations for the silicon microprobe recordings were measured and determined using a thresholding method. Forty-points prior to each stimulus artifact were averaged together and used as the baseline for each recording, as the DC levels were shifted due to the electrode-electrolyte interface offsets. The thresholds for all of the recordings were set to 1 mV or 1.5 mV above this baseline level.

Heart preparation two exhibited normal rhythms with no alternans even when the cycle length was reduced from 500 ms to 400 ms to 300 ms before

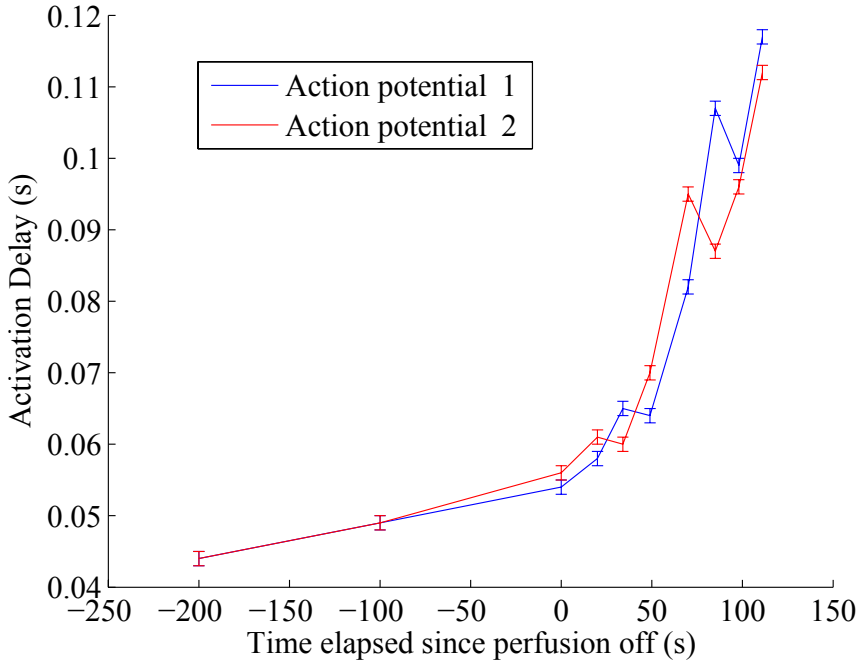

Figure 3.16: Change in stimulus activation time (ACT) over time for Probe 4 and action potentials 1 and 2.

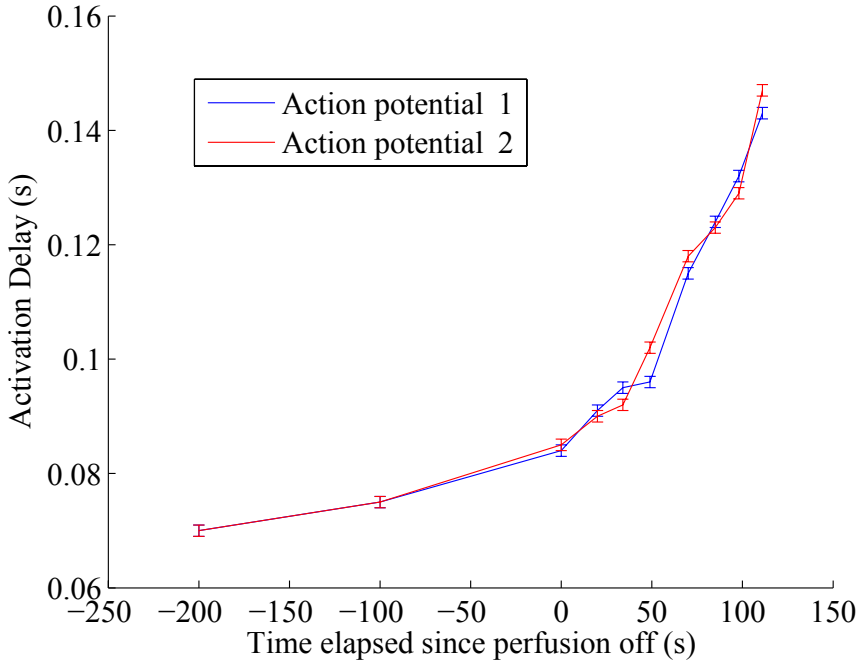

Figure 3.17: Change in stimulus activation time (ACT) over time for Probe 2 and action potentials one and two.

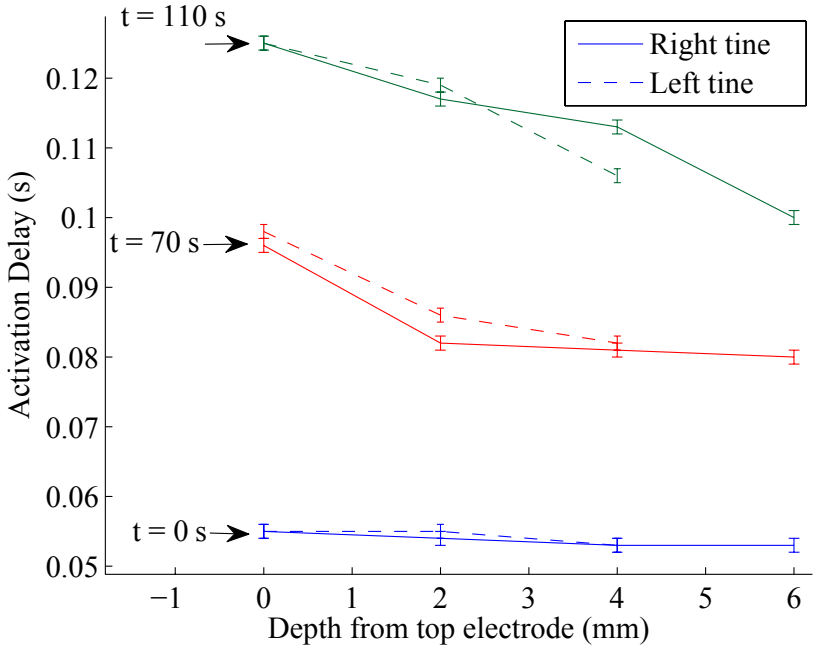

Figure 3.18: Change in ACT in canine ventricle after 0, 70, and 110 seconds of ischemia for Probe 4. Change is plotted for sites at epicardial surface, and 2 mm, 4 mm, and 6 mm into the tissue.

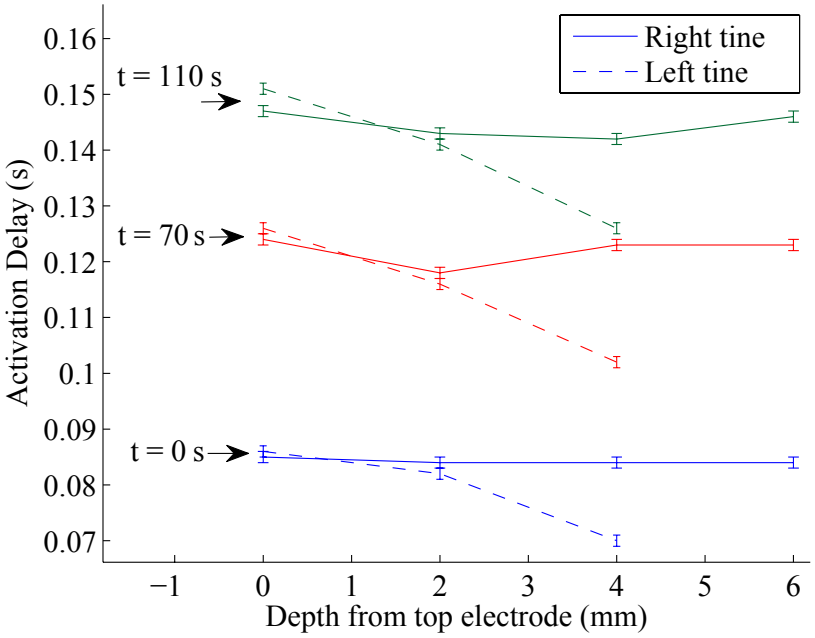

Figure 3.19: Change in ACT in canine ventricle after 0, 70, and 110 seconds of ischemia for Probe 2. Change is plotted for sites at epicardial surface, and 2 mm, 4 mm, and 6 mm into the tissue.

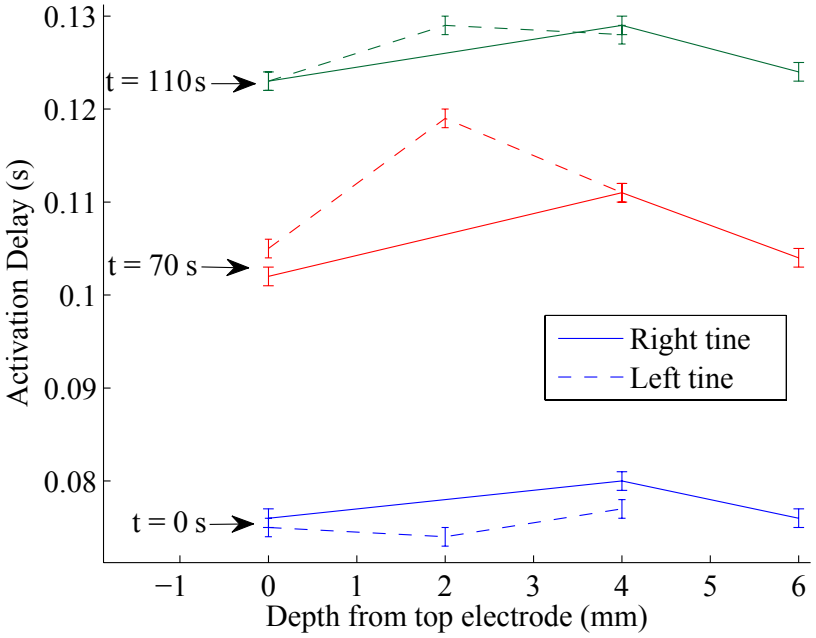

Figure 3.20: Change in ACT in canine ventricle after 0, 70, and 110 seconds of ischemia for Probe 1. Change is plotted for sites at epicardial surface, and 2 mm, 4 mm, and 6 mm into the tissue.

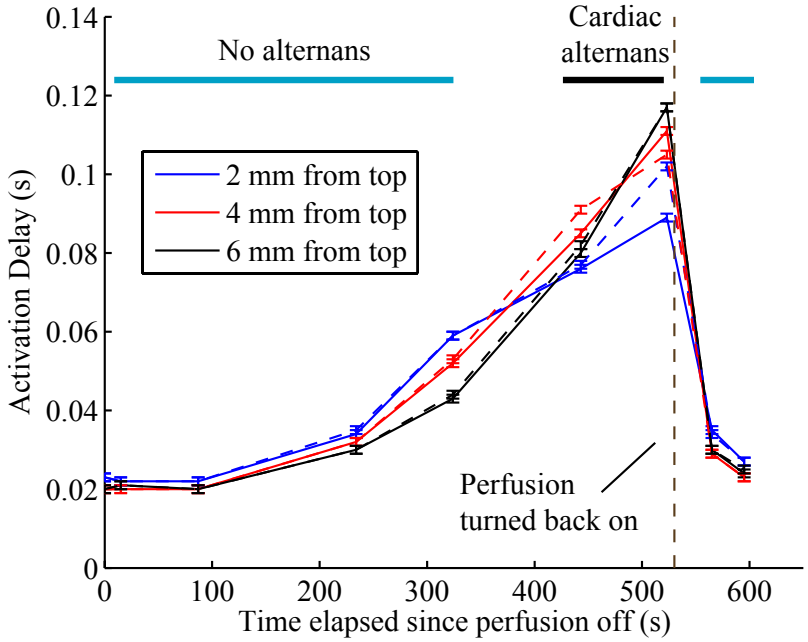

Figure 3.21: Measured ACT over time for three probe sites at various depths in the tissue for action potentials one (solid lines) and two (dotted lines).

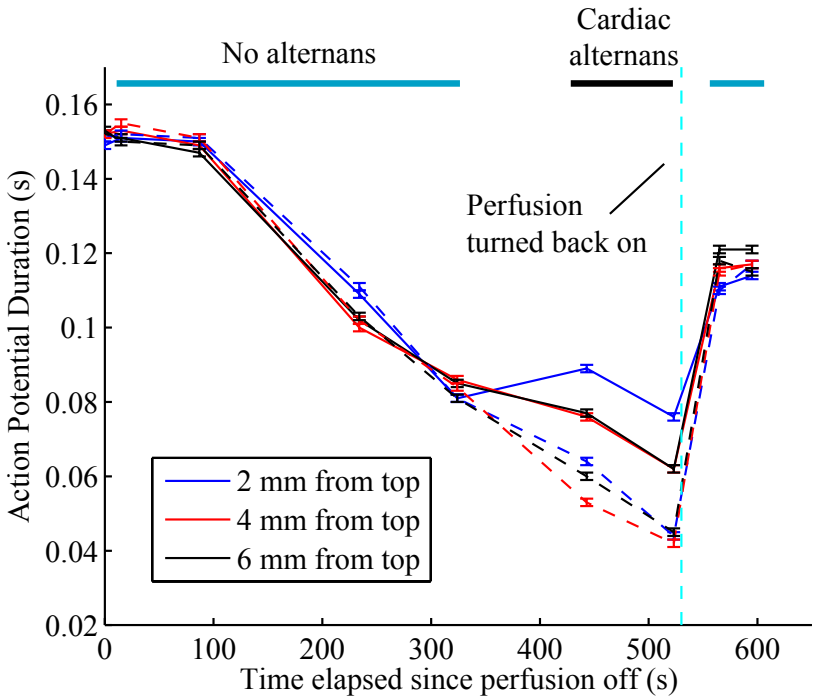

Figure 3.22: Measured APD over time for three probe sites at various depths in the tissue for action potentials one (solid lines) and two (dotted lines).

perfusion was turned off. Additionally, no alternans was observed for the first 450 seconds of no perfusion. After this, cardiac alternans was observed until 530 seconds, when perfusion was turned back on. The action potential durations exhibited during normal rhythms and cardiac alternans are shown in Fig. 3.22, with an initial decrease in action potential duration which is consistent with the literature citeGilmourZipes. After this, with the onset of cardiac alternans, the slope of action potential duration decrease flattened out before returning to higher levels with perfusion.

For dog heart preparation one, a small degree of alternans is visible at t = 0, before perfusion is turned off when the tissue is being paced at 300 ms cycle lengths. Alternans is indicated by a difference in action potential duration

between consecutive action potentials. It is apparent from Fig. 3.23 that just prior to ventricular fibrillation, all seven recording sites through the depth of the tissue are experiencing a large degree of alternans. Just after t = 80 seconds, from the recordings from the right probe prong, it is clear that the epicardial and endocardial sites experience little alternans while the intermediate sites experience much more alternans, though this pattern does not hold for the left probe prong. For these left and right prong recordings which are 500 μm apart, the tissue experiences concordant alternans.

The action potential durations for the most endocardial sites for Probes 1, 2, and 4 are shown in Fig. 3.24. Probes 1 and 2 have the largest alternans during the control recording before perfusion is turned off, and Probes 1 and 4 display the largest APD alternans just before fibrillation at 123 seconds.

3.4 Recordings of strain and electrical activity during ischemia onset

Various biological systems demonstrate coupled electrical and mechanical activity. For example, it is well known that cardiac muscle contracts in correlation with an electrical action potential that propagates through the tissue. It is also known that changes in mechanical loads on cardiac tissue, like those resulting from ischemia, can lead to abnormal action potentials or depolarization through the mechanoelectric effect [44]. Coupled mechanical and electrical recording can potentially provide more information and a more robust means to gather information about bioelectrical systems. One group has demonstrated the possible use of 3-axis accelerometers as a sensitive tool for early detection of

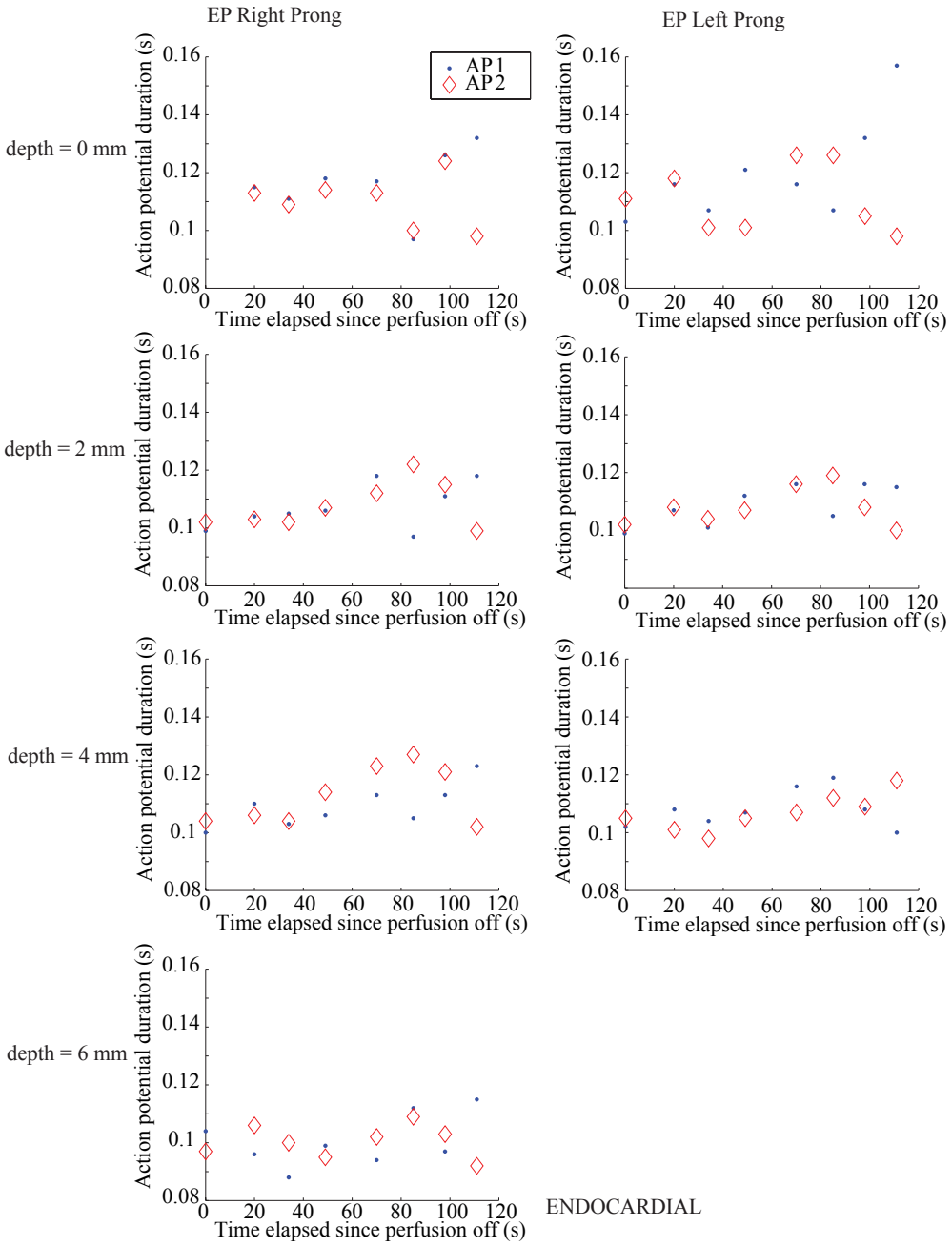

Figure 3.23: Change in action potential durations with no perfusion for action potentials one and two at various depths for Probe 4. Errors are 0.001 seconds on all measurements.

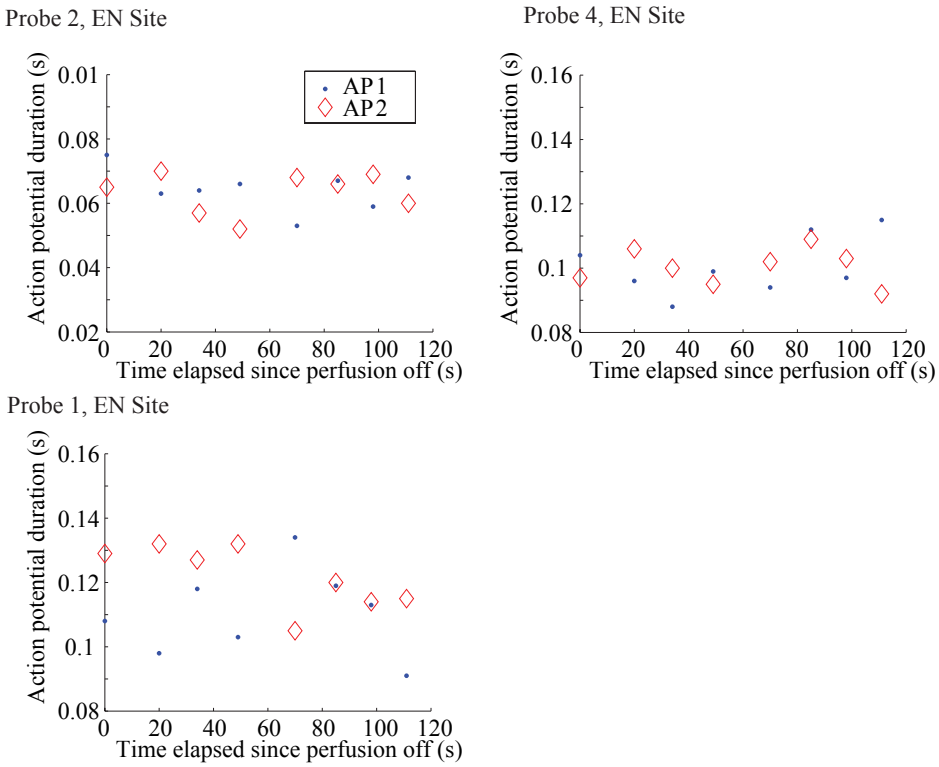

Figure 3.24: Change in action potential durations with no perfusion for action potentials one and two at the endocardial site for Probes 1, 2, and 4. Errors are 0.001 seconds on all measurements.

cardiac ischemia through monitoring of mechanical acceleration [45]. By comparing the frequency spectrum of the measured accelerations before and after occlusion, the authors were able to define a parameter for mechanical detection of occlusion.

In this section, we investigate the use of coupled mechanical and electrical probes to study ventricular arrhythmias. Using probes with integrated strain gauges presented in Chapter 2, the electrical and mechanical activity of canine left ventricles were recorded simultaneously through ischemia. The characterized force versus Wheatstone bridge voltage parameters are shown in Fig.

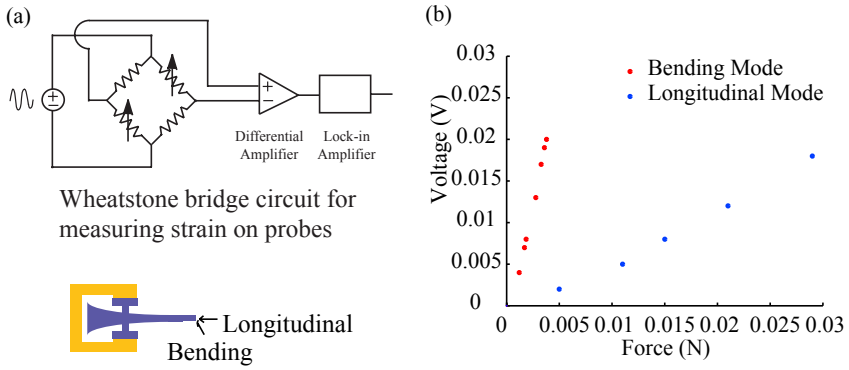

Figure 3.25: Wheatstone bridge circuit used to measure strain on probe with bending (left dots) and longitudinal (right dots) forces.

3.25. Since the heart is composed of cardiac fibers which are oriented in various directions through the thickness of the tissue to allow the organ to contract, strain recordings with the silicon probes will be sensitive to strain along many axes. The probes effectively integrate all the forces along their lengths into the strain measurements. For this reason, the strain profile varies from recording to recording, but are constant from beat to beat during normal perfusion.

Recording from the platinum recording sites and the integrated strain gauges allows observation of the signal morphologies presented in Fig. 3.26 and Fig. 3.27, which were observed under normal perfusion conditions. Though the strain signal morphology is different in the two preparations, there is no beat-to-beat variation in the strain signal. The optimal probe and fiber orientation can be investigated.

The effects of ischemia on mechanical measurements are then tested, as shown in Fig. 3.28 and Fig. 3.29, where perfusion is turned off for the indicated time. Cardiac alternans is clearly visible in the electrical action potential recordings. The strain signal similarly exhibits an alternating strain amplitude

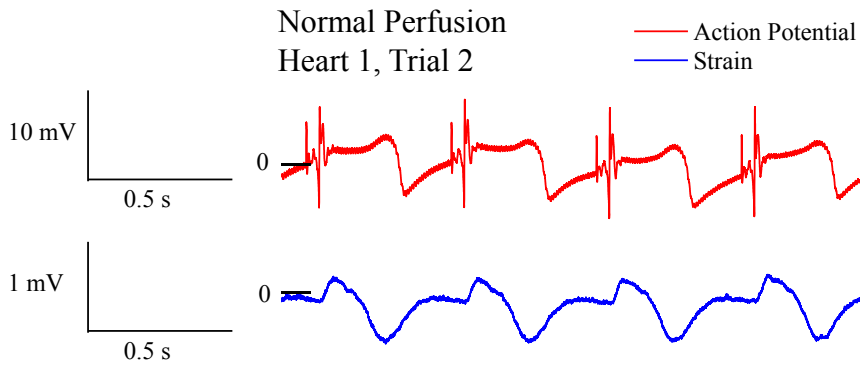

Figure 3.26: Simultaneous recordings of cardiac action potentials and strain in canine left ventricle during normal perfusion from dog heart preparation one with electrical recordings (top trace) and strain recordings (bottom).

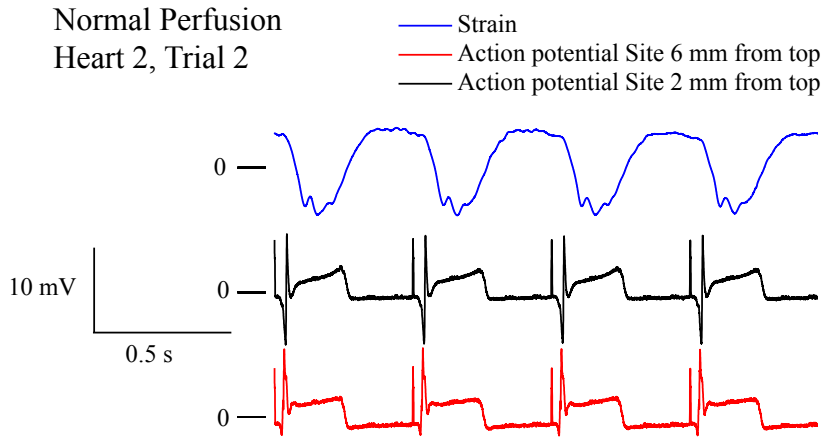

Figure 3.27: Simultaneous recordings of cardiac action potentials and strain in canine left ventricle during normal perfusion from dog heart preparation two with strain recordings (top trace) and electrical recordings (bottom two traces).

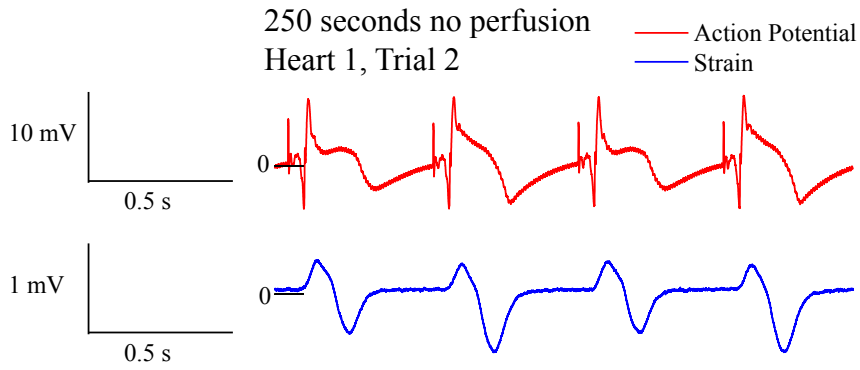

Figure 3.28: Simultaneous recordings of cardiac action potentials and strain in canine left ventricle with perfusion turned off from dog heart preparation one. Cardiac alternans is visible in the electrical (top trace) and mechanical signals (bottom).

for each successive beat, though the strain signal morphology is quite different between the two ventricles and recording locations. Even with the limitations of unknown fiber orientation, the strain signals give an indication of abnormal behavior in the heart due to the asymmetry between strain signals for successive beats. The strain signals are also able to give an indication of irregular heart beating, as shown in Fig. 3.30 and Fig. 3.31.

3.5 Future directions

In this section, the ability to record and extract information from many locations through cardiac tissue was presented. This capability allows us to gain an understanding of the variation of action potential durations and activation delay among various sites in the tissue with no perfusion conditions. Ischemic conditions are shown to be correlated with development of arrhythmias. These

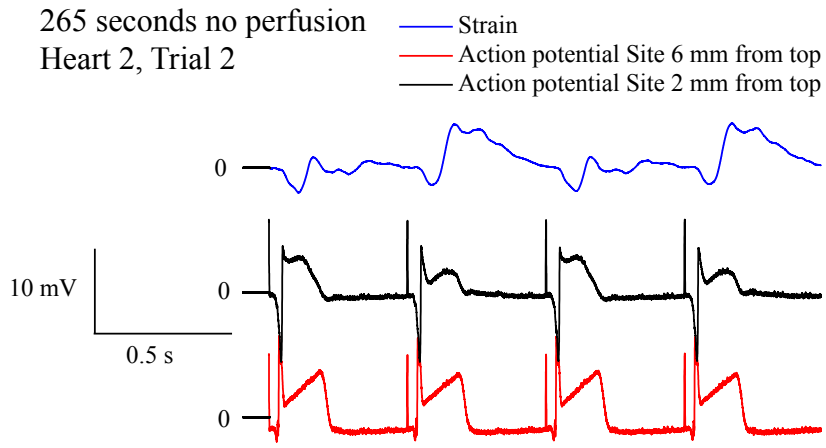

Figure 3.29: Simultaneous recordings of cardiac action potentials and strain in canine left ventricle with perfusion turned off from dog heart preparation two. Cardiac alternans is visible in the electrical (bottom two traces) and mechanical signals (top trace).

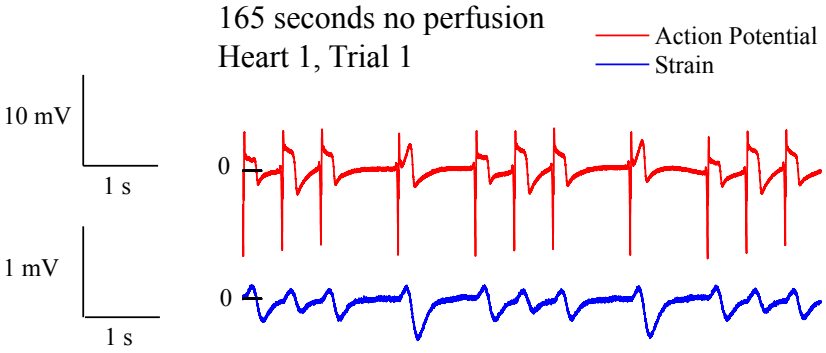

Figure 3.30: Simultaneous recordings of cardiac action potentials (top) and strain (bottom) in canine left ventricle with perfusion turned off from dog heart preparation one with irregular beats.

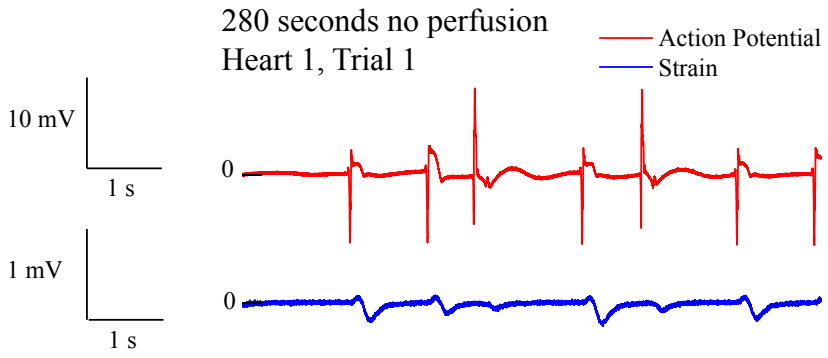

Figure 3.31: Simultaneous recordings of cardiac action potentials (top) and strain (bottom) in canine left ventricle with perfusion turned off from dog heart preparation one. Irregular beating is observed.

multichannel recordings can be further expanded to more canine ventricle samples and combined with histological observation to obtain a fuller understanding of variables affecting the observed differences in activation delay and APD through the depth and from apex to base of the tissue. Because conditions *in vitro* are not quite replicates of the *in vivo* conditions, arising from variables including residual blood inside the ventricles and stimulation from pacemaker cells in the heart instead of a bipolar stimulator, the effect of some variables can be further investigated. Additionally, the observed cardiac signal morphology, which can be time and site dependent, can be further investigated to remove the hypothesized capacitive filtering effects on the signals.

The ability to detect cardiac alternans and abnormal heart rhythms with ultrasonic horn probes with integrated strain gauges was also introduced in this chapter. Although fiber orientations and probe placement in the heart created variations in the recorded strain signals, using the probe system, cardiac alternans and irregular beating were able to be detected by comparing the beat-to-

beat variations in strain signals. This allows a measure of the amount of work done by the heart. Further characterization of the optimal probe orientations can be studied, as well as effects of mechanical stimuli on electrical activity in the heart.

CHAPTER 4

WIRELESS CARDIAC ACTION POTENTIAL DATA TRANSMISSION WITH ULTRASONIC HORN PROBES

4.1 Motivation

In this section, the development of a wireless transmission system for cardiac action potentials is introduced. Together with the ultrasonically inserted probes presented in the previous chapters, using a wireless data transmission system the number of recording channels can be dramatically increased. This can help in obtaining a more detailed understanding of cardiac action potential propagation in 3D under conditions leading to VF. By adding a wireless data transmission system and eliminating the wires, we can also remove wire induced stress on the probes and reduce micro-motion noise that would be picked up on the data transmission wires. With wireless transmission, the number of wires required for each probe can be reduced to two PZT driving wires which are only attached during the insertion phase of the probes. Thereafter, the PZT driving voltage sources are detached, isolating the setup from wire-induced noise. A battery can be incorporated on the probe-PCB system shown in Figure 4.1 to power the wireless transmission chip.

4.2 Coupled cardiac radio system

4.2.1 Ultrasonic horn probe mechanical characterization

The design and realization of microfabricated silicon probes that can be ultrasonically inserted into cardiac tissue has been presented in previous chapters. In this chapter, a radio for wireless data transmission is designed and integrated with the ultrasonic horn probes, as shown in Figure 4.1, and used to extract important restitution relations indicative of the likelihood of VF.

The probe and radio are affixed to one PCB, and metal contacts from both are wirebonded to the PCB. An antenna is also soldered onto the PCB to wirelessly transmit the radio signals.

4.2.2 Custom application specific wireless transmission chip

An integrated circuit with on board amplifier and radio has been designed to interface with the cardiac silicon probes. The circuit consists of a two-stage amplifier and a Colpitts oscillator [46, 47]. The circuit was designed in 0.35 μm CMOS technology from Austria Microsystems (AMS). The schematic is shown in Fig. 4.2. The chip includes four channels in addition to one set of individual test sub-components that can be assembled into another complete channel. The chip occupies an area of 9 mm^2, and draws 6.9 mW per channel, with approximately 2.4 mW devoted to the voltage controlled oscillator to allow sufficient signal power. Simulations indicate a drawn power of 4.82 mW per channel, but can be improved with a more efficient design of the amplifier and buffer stages.

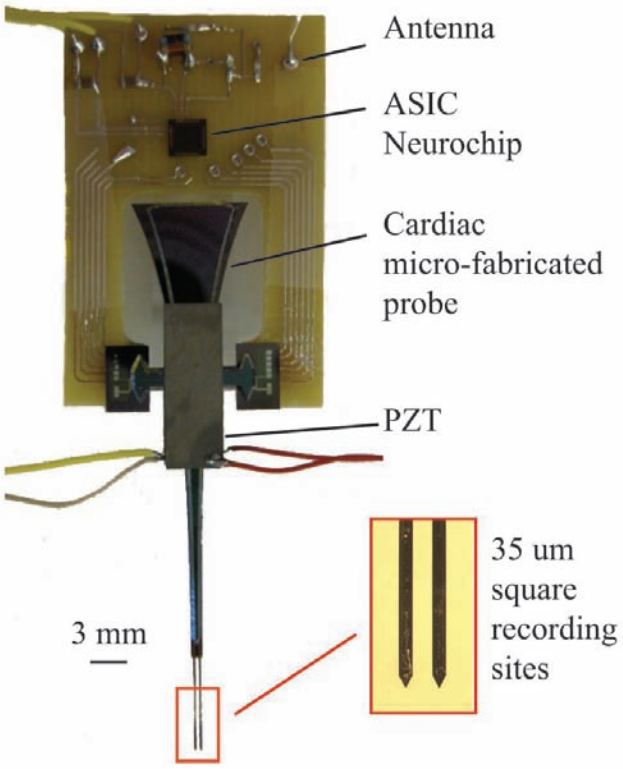

Figure 4.1: Cardiac probe and application specific integrated circuit (ASIC). The lead zirconate titanate (PZT) plates affixed to the cardiac probe are used to ultrasonically resonate the probe for insertion into heart tissue. Electrical contacts on the cardiac probe are used to measure the action potentials which are then sent to the ASIC input to be wirelessly transmitted.

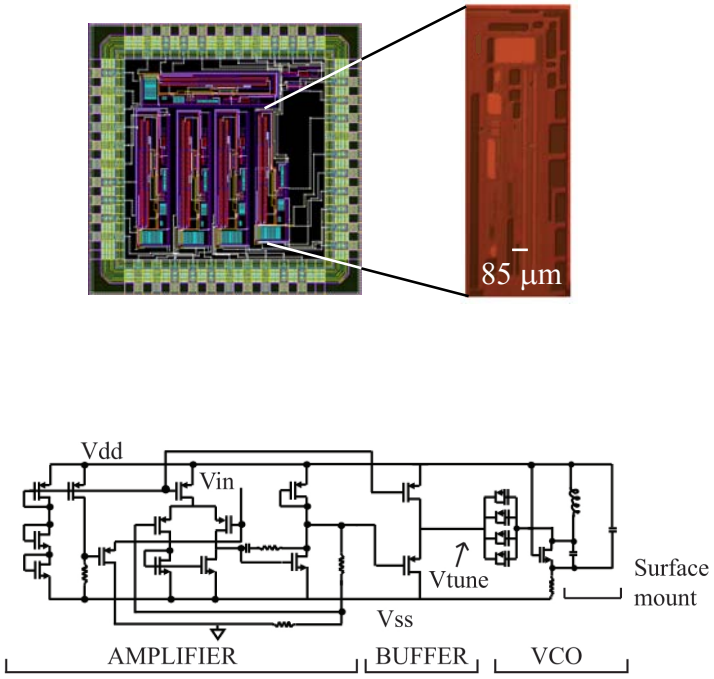

Figure 4.2: Layout of AMS 0.35 um chip in 2.988 mm X 2.988 mm square. This chip contains 4 amplifier and VCO combined systems, plus individual amplifier, buffer, and VCO stages for testing. An individual channel schematic is also shown.

Each channel design is composed of an amplifying stage that amplifies the signal by 40 dB, a buffer stage to provide isolation and prevent loading, and a voltage controlled oscillator (VCO). The amplifier is a two-stage amplifier with a differential first stage, and resistive feedback used to maintain a 40 dB gain.

Amplifier

For a feedback system, we must ensure certain conditions are satisfied for stability. A typical feedback system is as shown in Fig. 4.3 and the transfer function is given by

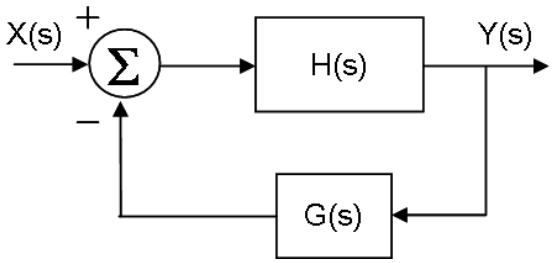

Figure 4.3: Negative feedback system and transfer function.

$$H(s) * (X(s) - G(s) * Y(s)) = Y(s) \tag{4.1}$$

$$\frac{Y(s)}{X(s)} = \frac{H(s)}{1 + G(s)H(s)} \tag{4.2}$$

In our amplifier H(s) is given by the gain of the two stages of the amplifier, and $G(s) = \frac{R_2}{R_1+R_2}$. To be stable in negative feedback, the open loop gain with equivalent loading must satisfy the two conditions G(s)*H(s) < 1 and the phase of G(s)H(s) < 180°, otherwise the denominator of the closed loop transfer function can go to infinity and cause oscillations when G(s)H(s) = -1.

For stability, the amplifier should have a phase margin of at least 45°, meaning that the magnitude of the phase plus 180° when the gain is 0 dB should be > 45°. To characterize the stability of the amplifier, the feedback loop is broken after the feedback stage. As shown in Fig. 4.4, the phase margin is slightly greater than 104°, giving an amplifier with good stability.

For our application as a neural amplifier whose output is fed to the tuning stage of a voltage controlled oscillator for wireless transmission, we are interested in a 10 kHz bandwidth stage with a 40 dB gain. As such, the resistors R_1 and R_2 are chosen to give $G(s) = \frac{1}{100}$ with R1 = 98000 Ω and R2 = 900 Ω. Fig. 4.5 shows the closed loop performance of both stages of the amplifier. As can be

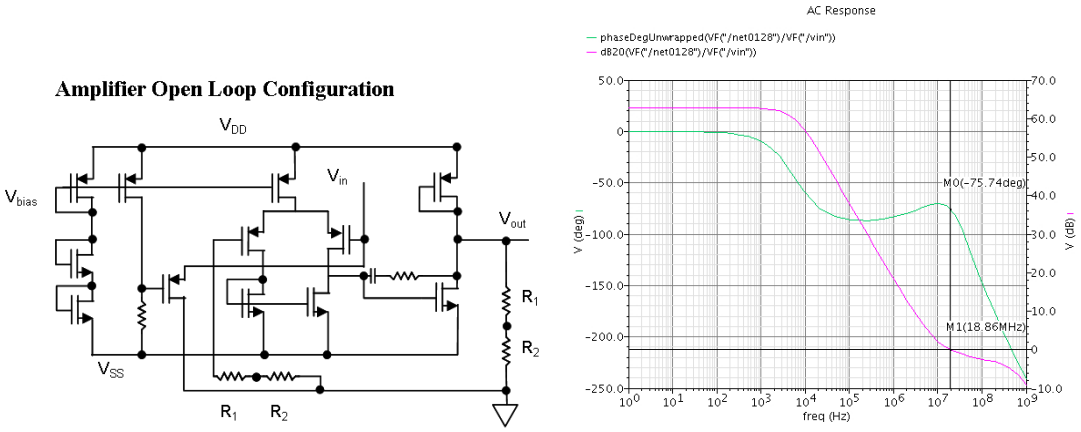

Figure 4.4: (left) Schematic of open loop system used to characterize circuit performance (right) Bode plot of amplifier performance. From the plot, it is clear that the phase margin is slightly greater than 104°.

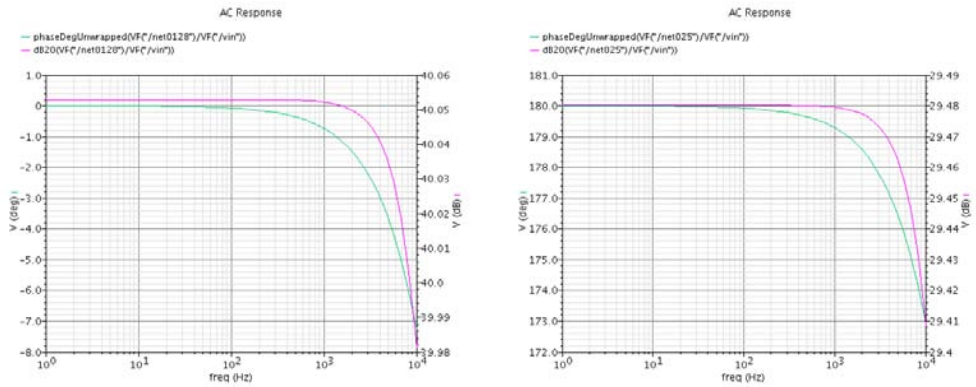

Figure 4.5: Simulated performance for both stages of amplifier (left), and simulated performance of first stage only (right) in closed loop configuration.

seen, a stable gain of 40 dB is achieved over a 10 kHz bandwidth.

The closed loop gain is related to the open loop gain according to

$$A_{CL}(f) = A_{OL}(f)\frac{R_1}{R_1 + R_2} \tag{4.3}$$

Node	Simulated DC bias (mV)	VDD/VSS = +/-1.5 V DC bias (mV)	VDD = 1.86 V, VSS = -1.26 V DC bias (mV)
V_{gate}	-856	-613	-556
$V_{outstageone}$	-828	-687	-345
V_{-bias}	703.8	666	956
V_{-out}	-8.3	-360	-102

Figure 4.6: Simulated and measured DC bias node conditions for designed power supplies (VDD/VSS = +/-1.5 V), and those that provided the best gain conditions (VDD = 1.86 V, VSS = -1.26 V).

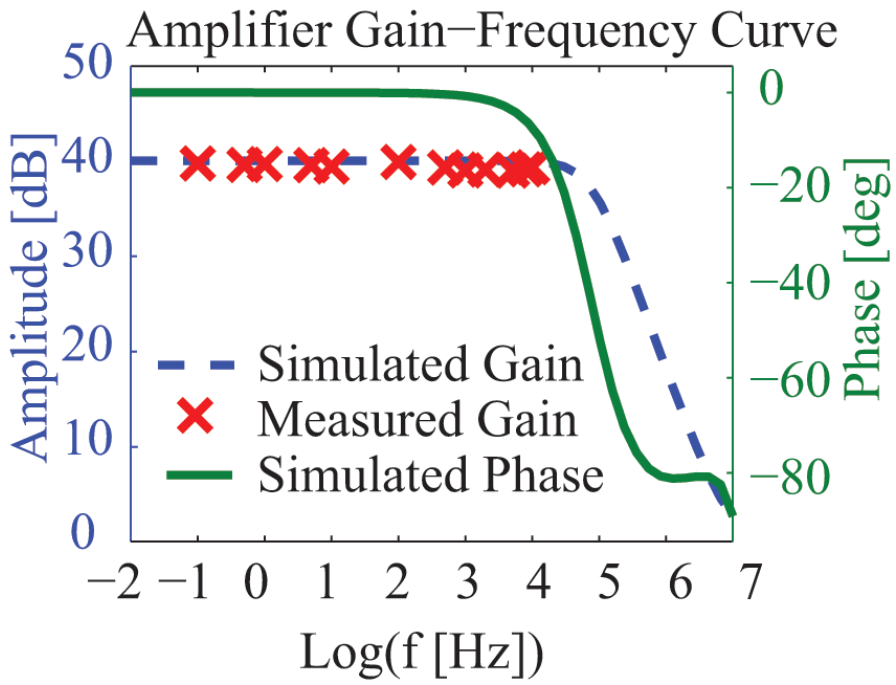

Figure 4.7: Measured amplifier performance versus simulated performance.

The measured DC node voltages at the various stages versus the simulated voltages are shown in Table 1. The measured performance of the amplifier stage alone is as shown in Fig. 4.7. The gain was measured to be 114.5 (41.18 dB) over the range 100 Hz to 10 kHz.

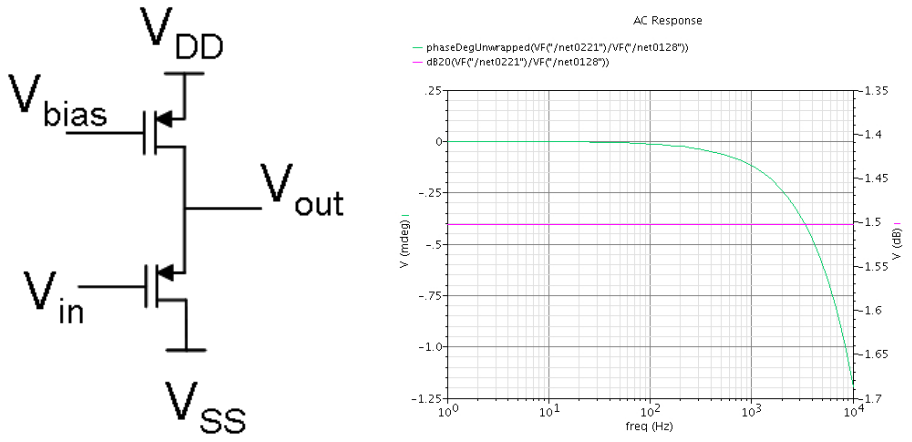

Figure 4.8: Buffer design and simulated performance for VDD = 1.5 V and VSS=-1.5 V over the frequency range of interest (0-10 kHz). As can be seen, the gain and phase are stable over the 10 kHz range (gain -1.5 dB and the phase reaches -0.00125° at 10 kHz).

Buffer

To isolate the amplifier from any loading effects from the VCO stage, a buffer was included consisting of a source follower stage. Since the gain of a source follower stage is given by $A_v = -g_m R_L$, a gain of close to unity can be obtained for a large bandwidth. The design and simulated performance of the buffer stage are shown in Fig. 4.8.

Voltage controlled oscillator

Finally, the voltage controlled oscillator was implemented using a Colpitts oscillator. The voltage controlled oscillator uses the input signal (a neural or cardiac signal) to modulate the frequency of oscillation, with frequency modulation (FM) of the 100 MHz carrier signal. As any signal can be decomposed into its Fourier components, the concept of frequency modulation can be understood

by considering the frequency modulation imparted by an arbitrary message signal, M(t) [48], where M(t) is given by a single tone signal:

$$M(t) = A_m \cos(2\pi f_m t) \tag{4.4}$$

With the message signal modulating the carrier frequency, f_c, the new frequency is given by:

$$f_i(t) = f_c + k_f A_m \cos(2\pi f_m t) \tag{4.5}$$

where $k_f A_m$ is the frequency deviation that the message signal imparts on the carrier signal.

The phase is then given by

$$\theta_i(t) = 2\pi \int_0^t f_i(t)\,\mathrm{d}t. = 2\pi f_c t + \frac{\delta f}{f_m} \sin(2\pi f_m t) \tag{4.6}$$

and the modulated carrier signal S(t) is

$$S(t) = A_c \cos(2\pi f_c t + \beta \sin(2\pi f_m t)) \tag{4.7}$$

where $\beta = \frac{\delta f}{f_m}$.

The schematic for a Colpitts oscillator, which is used in this design, is shown in Fig. 4.10. The oscillation frequency is given by:

$$\omega_R^2 = \frac{1}{L(C_{var} + \frac{C_1 C_2}{C_1 + C_2})} \tag{4.8}$$

where L is the inductance, C_{var} is the variable capacitance determined by the message signal tuning, and C_1 and C_2 are the two fixed load capacitances. A 1 cm wire is connected to the oscillation node to serve as an antenna.

To achieve frequency modulation, the buffer output is fed to the drain-source node of four NMOS MOSCAPS tied in parallel. MOS varactors exhibit lower power consumption and better phase noise performance than diode varactors [4]. By varying the drain-source voltage relative to the gate voltage, which is held at a DC bias of approximately the positive power supply voltage of 1.5 V, the depletion channel and number of holes/electrons is modulated. Acting in series with the oxide capacitance, the overall capacitance over the MOSCAP changes. The MOSCAPS are used in inversion mode with the drain and source tied together and the bulk tied to the lowest power supply voltage. Inversion mode MOSFETS (I-NMOS) allow for a wider tuning range than accumulation mode MOSFETS with the bulk, source and drain tied together and thus are particularly useful for VCO applications with relatively large AC voltage swings over the MOSCAPS. This results from the reduced ability of the structure to enter accumulation mode, as shown in Fig. 4.9. With these MOSCAPs, the simulated transient oscillating behavior of the Colpitts oscillator is shown in Fig. 4.10.

Measured VCO performance

The frequency modulated (FM) wave can be demodulated using a commercial portable FM radio with a superheterodyne receiver tuned to the carrier frequency of the VCO. Here, a commercial Win-Radio FM receiver is used to receive the signals. The signals are fed to the audio card of a PC, and a custom

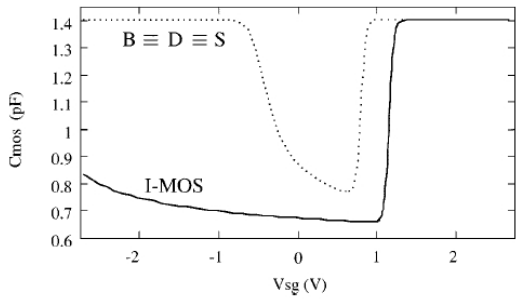

Figure 4.9: Inversion mode and accumulation mode pMOS MOSCAPS [4].

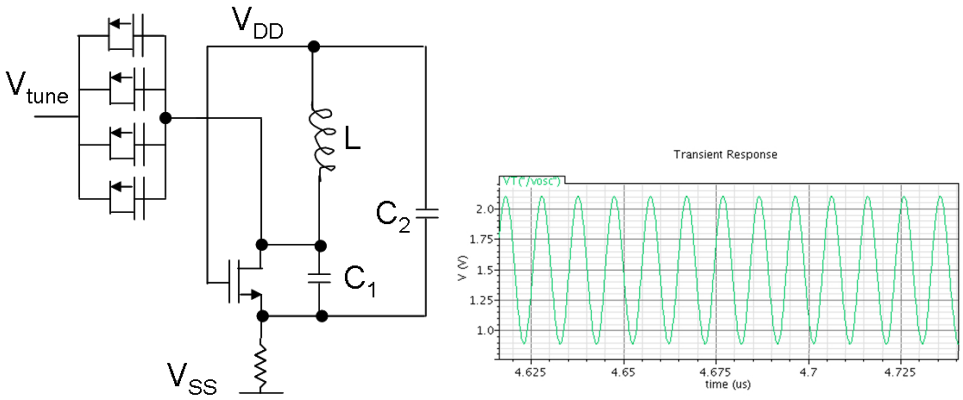

Figure 4.10: Schematic of voltage controlled oscillator and simulated transient behavior.

LabVIEW program is used to record these signals.

The frequency tuning characteristics of the VCO were measured by providing a DC voltage input and measuring the received signal frequency. As the transmission antenna is an inductor and capacitor, it parasitically affects the oscillation frequency. With parasitics from the antenna included with the equivalent circuit model of the VCO, the oscillation frequency is given by the solution to

$$1 - \omega_R^2(L_aC_a + LC_a + L(\frac{C_1C_2}{C_1 + C_2} + C_{var}) + \omega_R^4 L_aC_aL(\frac{C_1C_2}{C_1 + C_2} + C_{var}) = 0 \qquad (4.9)$$

where the inductor, L_a and capacitor C_a in series. Fitting this to the measured tuning characterstics for the voltage controlled oscillator yields antenna equivalent circuit parameters of:

$$L_a = 10^{-13} H \tag{4.10}$$

$$C_a = 5.415 * 10^{-12} F \tag{4.11}$$

Simulating the expected tuning characteristics with parasitics included and comparing these with the measured tuning curve yields the fit shown in Fig. 4.11. It is seen that the two agree pretty well. At a certain voltage around 1 V, the measured oscillation frequency plateaus. This is due to ESD protection diodes in the input pads which prevent the voltage from reaching too near the power supply voltages of -1.5 and 1.5 volts.

The range of the current system is approximately 1 meter, with 2.4 mW devoted per channel as mentioned previously. The range of the system could be extended by increasing the transmitted power or including a power amplifier stage. The required transmitted power based on received power, wavelength, and distance is given by the Friis Transmission Equation.

$$P_t = k(\frac{4\pi R}{\lambda})^2 \tag{4.12}$$

Phase noise

The phase noise of the voltage controlled oscillator is measured using an HP 4395A spectrum analyzer. As the spectrum analyzer has a 50 Ω input impedance, an impedance matching circuit is constructed to the output oscillation node of the VCO to avoid loading the circuit. The circuit is shown in Fig.

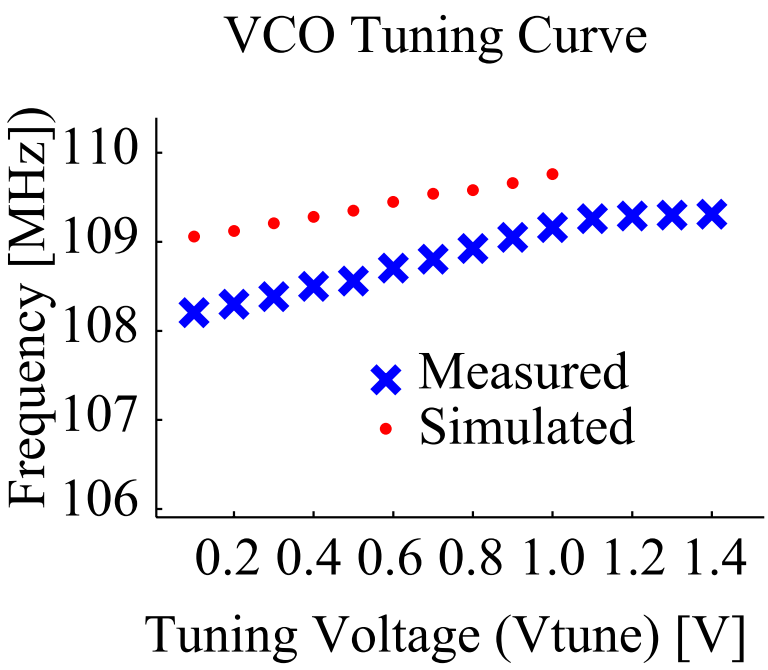

Figure 4.11: Voltage controlled oscillation measured and simulated tuning curve for various values of the tuning voltage.

4.12 where the voltage controlled oscillator components are $C_1 = C_2 = 5.6$ pF, L = 220 nH, R = 3 kΩ. C_p arises from the parasitic capacitances of the printed circuit board and based on measurements is equal to approximately 6.3 pF. The surface mount impedance matching components are $C_3 = 1$ pF, $L_1 = L_2 = 68$ nH. $C_p = 42.75$ pF arises from the parasitic capacitances of the BNC cable leading from the circuit to the spectrum analyzer, which is 1.5 ft long and has 28.5 pF/ft of capacitance. R_{in} represents the input impedance of the HP 4395A spectrum analyzer and is 50 Ω.

The measured phase noise (PN) in dBm is converted to the phase noise power in dBm/Hz using the expression:

$$PN[dBm/Hz] = PN_{\Delta f}[dBm] - 10\log(RBW)[Hz] \tag{4.13}$$

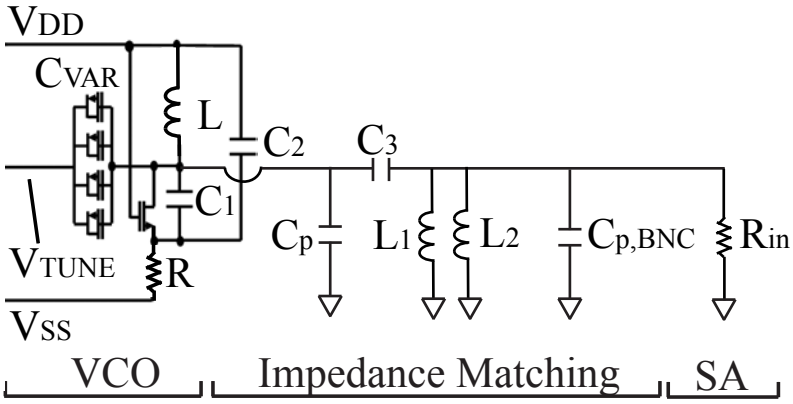

Figure 4.12: Impedance matching circuit to output of voltage controlled oscillator for measuring phase noise, with the voltage controlled oscillator (VCO), impedance matching circuit, and spectrum analyzer equivalent circuit components shown.

where RBW is the resolution bandwidth and $PN_{\Delta f}$ is the phase noise at a frequency offset of Δf. The measured phase noise characteristics are shown in Figure 4.13.

4.3 Wireless transmission with assembled system

4.3.1 Wireless transmission of cardiac action potentials from canine ventricular tissue

The cardiac ultrasonic horn probes were integrated with the designed wireless chip for action potential wireless transmission from canine ventricular tissue preparations. The details of tissue extraction and preparation can be found in

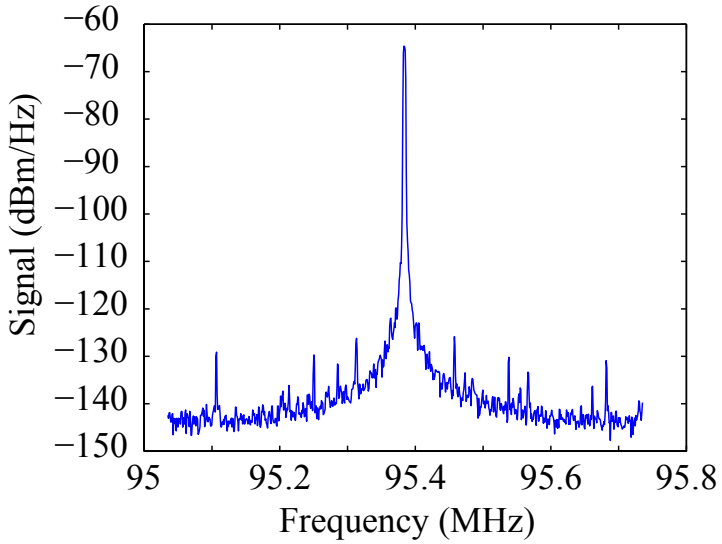

Figure 4.13: Measured spectrum for oscillator using impedance matching circuit, with Vtune = 0 V, and battery powered operation. The measured phase noise at a 100 kHz offset is -71.1 dBc/Hz.

[49]. Briefly, after anesthetizing the dogs (n = 2), the heart tissue was extracted and the ventricles were cannulated. The tissue was perfused with heated, oxygenated Tyrode solution (124 mM NaCl, 4 mM KCl, 24 mM $NaHCO_3$, 0.9 mM NaH_2PO_4-H_2O, 0.7 mM MgCl-6H_2O, 0.5 mM dextrose, and 2 mM $CaCl_2$-2H_2O) and was electrically paced with a bipolar electrode with nominal values of 2 ms pulses at 500 ms cycle lengths. For the wireless transmission experiments, a software-defined G305e WinRadio receiver and demodulator were used to capture the incoming FM signals. A custom LabVIEW code was written to capture the resulting demodulated signals output through the PC audio card.

The coupled cardiac probe and PZT resonance was measured (111 kHz) with an HP 4194A impedance analyzer. A 111 kHz 16-Vpp sine wave was applied

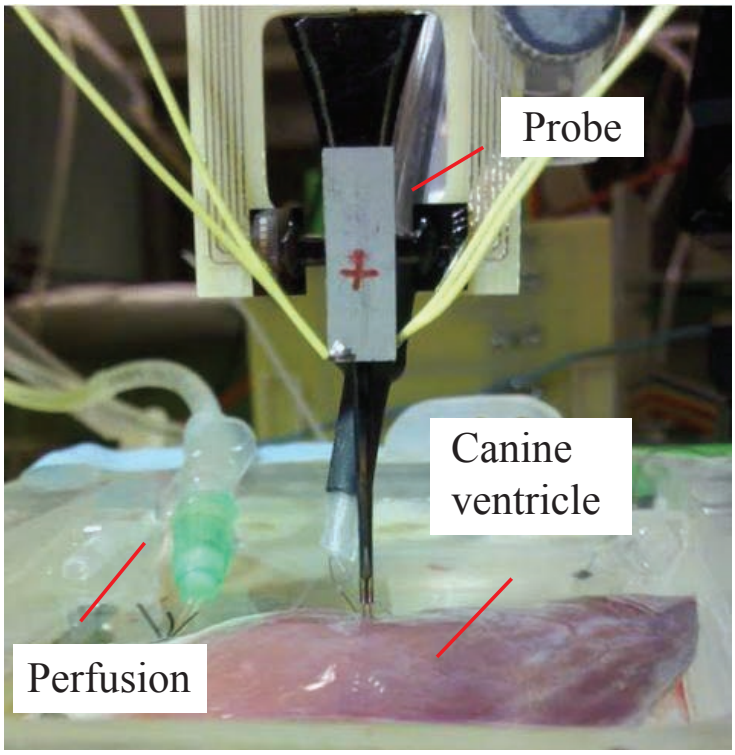

Figure 4.14: Ultrasonically inserted probe in canine left ventricle tissue. The tissue is perfused with Tyrode solution and paced with a bipolar stimulation electrode.

to the PZT to ultrasonically excite the cardiac probe during insertion. After insertion of the silicon probe, as shown in Figure 4.14, one channel of the cardiac probe was amplified using an AM Systems Model 1800 amplifier with an amplification of 100 and 0.1 Hz and 10 kHz high-pass and low-pass cutoffs, respectively. A National Instruments USB-6009 data acquisition system was used for acquisition and data were recorded on a PC using a custom LabVIEW code. The same line of the cardiac probe was sent to the radio with a 100 pF capacitor in parallel to serve as a capacitive divider to maintain the frequency modulation within the 20 kHz demodulation bandwidth.

As the cardiac signals are relatively large (10-20 mV), the cardiac signals were directly sent to the VCO rather than amplified first. The cardiac signals were wirelessly received and demodulated. The wired and wirelessly transmitted signals were captured sequentially, as shown in Figure 4.15. High frequency components in the action potentials are present at the start and end of the action potentials, and the high frequency overshoot of the oscillator response is visible at these locations. Based on the impulse response of LC oscillators, the magnitude of the effect of a current pulse on amplitude and phase is time-variant depending on the phase of the oscillator relative to the current pulse, but automatic gain control methods can be used to minimize the amplitude variation effects [50].

Additional noise sources during the ex vivo heart tissue recordings arise from the DC power source (Agilent E3631A) used to power the VCO, causing up-conversion of low frequency noise into VCO phase noise, and the cardiac probes, which also pick up a large amount of noise with the power supply noise present. As can be seen from Figure 4.15, though the discussed noise factors make the wirelessly transmitted signal noisier than the wired signal, the parameters of interest including the action potential durations (APDs) and diastolic intervals (DIs), or intervals between action potentials, can clearly be distinguished from both wired and wireless recordings.

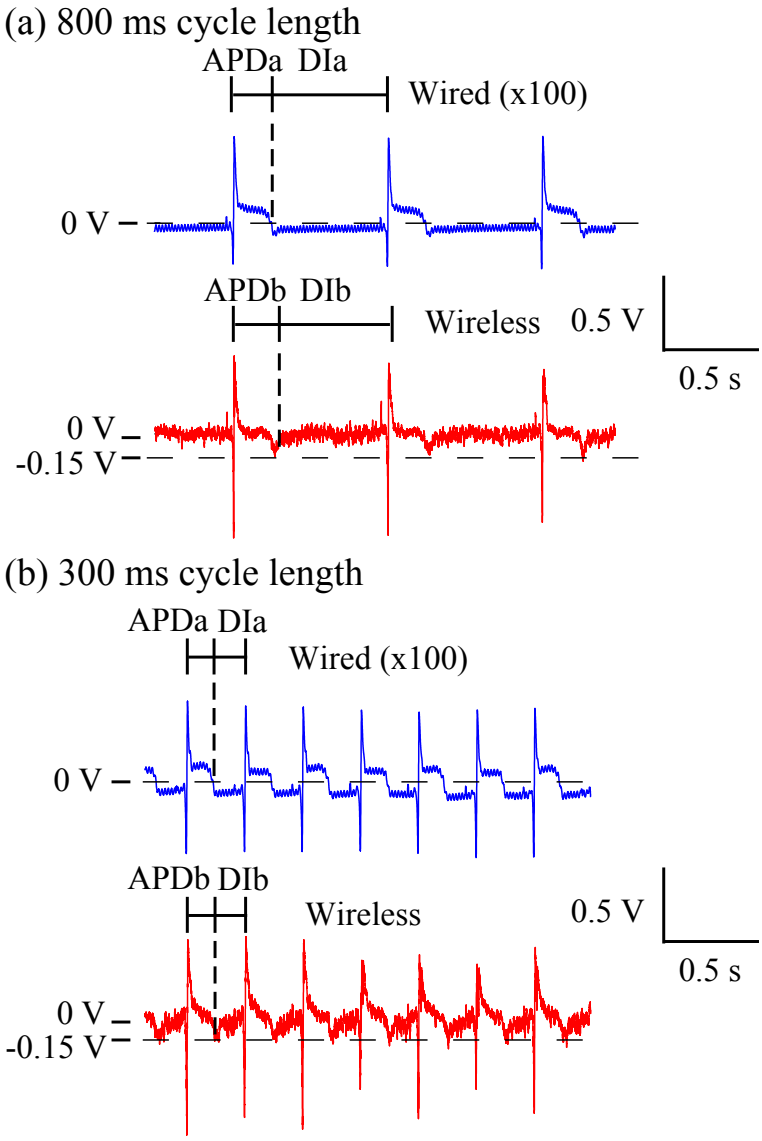

Figure 4.15: Averaged wired and wirelessly transmitted action potentials recorded using the silicon microprobes in a canine ventricular preparation. The tissue was paced with 2 ms pulses at different cycles lengths, shown here with lengths of (a) 800 ms and (b) 250 ms. The method for extracting restitution curve parameters is also shown. Threshold voltages of 0 V for the wired signals, and -0.15 V for the wirelessly transmitted signals were used to extract the action potential durations (APDs) and diastolic intervals (DIs).

4.3.2 Wireless transmission to study cardiac restitution relations

From the wirelessly transmitted data of cardiac action potentials, important relations governing cardiac tissue function can be obtained from various regions in the 3D tissue.

The left ventricular tissue preparations were paced at various cycle lengths, as shown in Figure 4.15, to extract the restitution curve. The tissue was first paced at cycle lengths of 900 ms with 2 ms pulse lengths for 30 seconds. The cycle lengths were then decreased in 100 ms intervals, and the tissue was allowed to settle for 30 seconds at each pacing interval before action potential measurements were taken. From the data, we can calculate the action potential durations and diastolic intervals. Typically, action potential durations are estimated based on the interval between the stimulus artifact and some percentage of repolarization, for example 95% [51]. For these probe recordings, DC and low frequency signal components are filtered for both the wired amplified signal and for the voltage controlled oscillator transmitted signal. Since signal amplitudes remain relatively constant over the restitution curve recording time (10 minutes), we use a constant voltage threshold to indicate action potential duration and diastolic interval. This estimation is as shown in Figure 4.15, where a 0 V threshold was selected for the wired transmissions, and -0.15 V for the wireless transmissions. The extracted restitution curves from the wired and wirelessly transmitted action potentials are shown in Figure 4.16, with data averaged from five action potential cycles (data is not available for five points at a diastolic interval of 0.4 s and so this point is excluded). The curves demonstrate the expected increase in slope at small diastolic intervals, as well as a plateau at higher diastolic

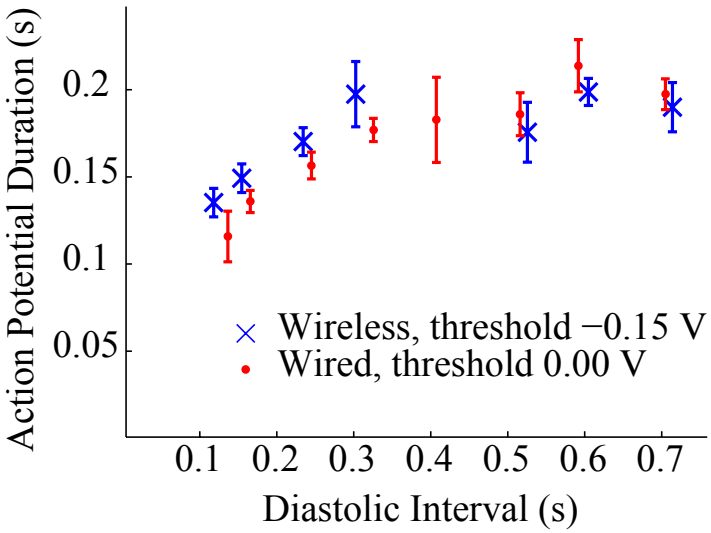

Figure 4.16: Extracted restitution curves from wired and wirelessly transmitted data using the indicated voltage thresholds. Measurements were averaged for five action potentials per pacing cycle length. Error bars indicate standard deviation of measurements.

intervals.

Since action potential duration and diastolic intervals of subsequent action potentials are related, averaging action potential durations and intervals over many cycles can help to reduce the variation in the measurements. With further measurements, the wired and wireless techniques can be analyzed using Bland-Altman analysis to conclusively determine the expected variation and 95% confidence interval of expected differences between the two measurement techniques.

4.4 Future directions: Proposed miniaturized 3D system and comparison to optical fluorescence techniques

Based on the aforementioned results, the design for a preliminary 3D microprobe array is presented in Figure 4.17, which can have resolutions for recording action potentials of < 2.5 and 5 mm along the x and y directions parallel to the surface of the tissue and 100 microns in the z-axis through the thickness of the tissue. The x and y resolution can be further improved with thinner PCBs and smaller PCB linewidths. To achieve this, the silicon microprobe dimensions can be scaled down by a factor of four in each axis. Finite element simulations reveal this silicon horn structure has a longitudinal resonance of 410.5 kHz. When assembled, the probes can simultaneously be driven into the tissue by driving the PZT plates. Selected channels can be wirelessly transmitted to obtain action potential data in 3D throughout the tissue, and map the varying restitution relations throughout the tissue.

The proposed system provides an advantage over other techniques currently available, such as fluorescence imaging techniques with voltage sensitive dyes, which can achieve very good micron resolutions along the x and y axes, but almost no resolution in the z-axis. Two-photon imaging techniques can help to some extent, allowing imaging up to depths of 1 mm into the tissue, and scanning over a 1 cm^3 section of tissue in x and y [52]. However, these techniques cannot provide the z-resolution capable with the miniaturized silicon ultrasonically inserted microprobes, demonstrating the potential of the 3D microprobe system for further study of cardiac arrhythmias.

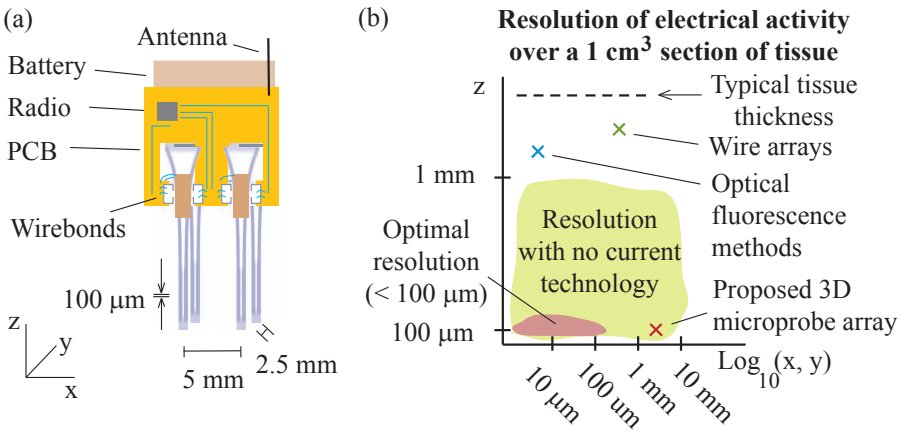

Figure 4.17: (a) Four probe section of proposed miniaturized 3D microprobe array. (b) Improvement in resolution attainable with proposed 3D silicon microprobe array.

CHAPTER 5

SILICON MICROPROBES FOR HYBRID INSECT NEURAL GAS SENSING

5.1 Motivation

Insects have developed sensor abilities over billions of years of evolution. In this work, we demonstrate the feasibility of creating a fully implantable system interfaced to an insect's neural system to detect insect responses to various olfactory cues in the environment.

Insect biosensors that detect increased neural activity from single olfactory receptor neurons (ORNs) on the antenna or from electroantennograms have been previously investigated [53, 54]. Studies have demonstrated some species, such as the moth Bombyx mori, have olfactory neurons capable of detecting pheromones with concentrations as low as several parts per quadrillion [55]. With traditional neural recording equipment using in vivo preparations of insects to test responses to chemical odorants, concentrations of parts per trillion can be detected, comparable to or surpassing sensitivities of large proton-transfer reaction-mass spectrometers [56]. However, these biosensors have limitations in their practical effectiveness. Some respond similarly to the presence of any odor, thus not demonstrating specificity, while others only sample molecules which diffuse close to a single ORN (with a cross-section of several μm^2) limiting reliability and portability by requiring accurate and stable probe placement. These sensors require that microelectrodes be positioned accurately on the antenna surface, or near a specific ORN. Studies have demonstrated that the range of responsiveness of moths can be expanded beyond those that

moths naturally respond to using Pavlovian conditioning. For example, one study trained adult moths to respond to explosives odors with a feeding response [57]. This particular approach to achieve a gas sensor, which is based on behavioral responses, has limitations in its reliability and specificity since behavioral responses can vary with other stimuli (e.g. light and sound) [57]. However, together with another recent paper showing that moths can also be trained to respond to certain odors prior to the pupal stage, during the larvae stage Fig. 5.1, and retain memory of their training into the adult stage [58], these studies demonstrate the possible range of applicability of an integrated insect sensor.

For an effective sensor system, it is desirable to have reliability, specificity, and sensitivity. It has been demonstrated that surgically implanted substrates for microsystems can be implanted in pupal stage insects without greatly affecting their adult lifespan [59], suggesting promise for utilizing a pupal-stage implanted microelectrode in the pupal brain for an integrated gas sensor. As shown in Fig. 5.1, probes inserted during the pupal stage of the *Manduca sexta* life span provide the best electrical and mechanical integration. The insect microsystem could provide enhanced reliability, specificity, and sensitivity by tapping into the high sensitivity and specificity of an insect's olfactory system, coupled with pupal stage insertions allowing for good tissue integration and reliability. Additionally, further studies have demonstrated that moths can be maintained in the pupae stage and prevented from becoming an adult by injecting juvenile hormone, allowing a hybrid sensor to remain active indefinitely [60].

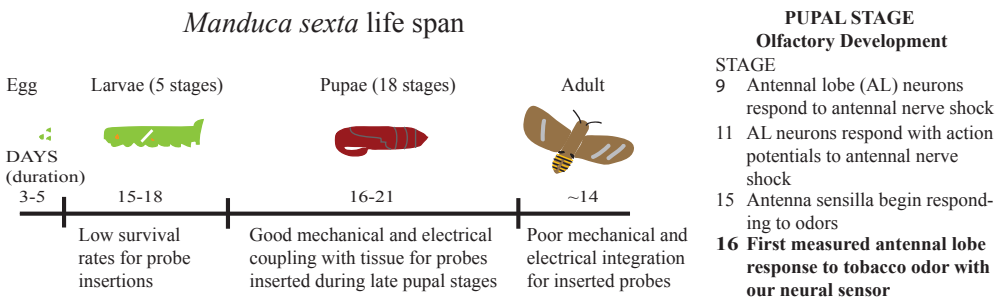

Figure 3. Stages of insect development and results of probe insertion at various time points (left). Important pupal stage events during olfactory development (right).

Figure 5.1: A timeline depicting the main developmental stages in the insect Manduca sexta, as well as results of substrate insertions at various point during development.

5.2 Microfabricated sensor interface

5.2.1 MEMS neural probes design and fabrication

Intracellular neural recordings are typically performed to study individual neurons. This method utilizes small diameter glass capillaries pulled to very fine tip diameters for cell penetration or patch clamping. While these methods are very useful for short term studies of ion channels and cell action potentials, long-term and large-scale studies of cell behavior become difficult to perform.

For studying the behavior of many cells at once, multielectrode arrays of microfabricated neural probes allow for parallel recording from many different sites with known distances separating them. This can potentially allow for extraction of information about the location and pattern of activity distributed across a wide region of neurons.

Neural probes were designed and microfabricated in the Cornell Nanofabrication Facility, following a similar process flow used for the cardiac probes. The

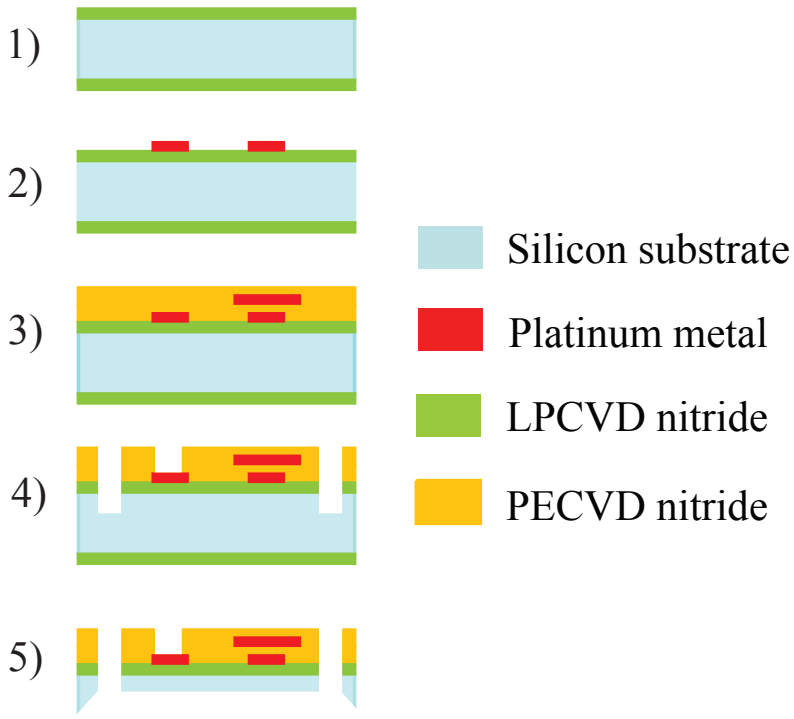

Figure 5.2: Process flow for microfabricating neural probes illustrated using cross-section of probe tip. 1) Deposit LPCVD nitride on silicon wafer. 2) Deposit photoresist and evaporate and pattern metal using lift-off. 3) Deposit an insulating layer of nitride, evaporate and pattern another ground layer of metal using lift-off, then passivate surface with another layer of silicon nitride. 4) Etch openings to bond and recording sites. DRIE silicon to define probe boundaries. 5) KOH etch to release probes.

process flow is reproduced in 5.2.

5.2.2 Microprobe impedance characterization

To measure the impedance characteristics of the microfabricated neural probes, cyclic voltammetry followed by electrochemical impedance spectroscopy (EIS) is performed on the microfabricated electrodes, as discussed in previous chap-

ters. During the tests, the electrodes are immersed in insect saline to mimic the hemolymph inside the insect. Three consecutive EIS measurements are averaged together yielding the experimentally measured interface impedance shown in Fig. 5.3. Also shown are the simplified equivalent circuit model and fit to the measured results.

5.3 Insect olfactory system

In many insects, the olfactory system is extremely important for survival and reproduction [61]. In male moths, the olfactory system is highly selective and specific to pheromone chemicals. Based on numerous studies, it is well known that moths can guide their flight towards pheromone sources several kilometers away [62]. Due to structural and processing similarities between insect antennal lobes and the olfactory bulb in the central nervous system, there has been much research on the morphology and physiology of insect antennal lobes, as well as how the presence of different odors are coded, and how concentrations are encoded.

The first order detectors in the insect are olfactory receptor neurons (ORNs) located in the antenna. The axons of the ORNs travel down the antennal nerve to the antennal lobe [61]. The antennal lobe is composed of approximately 40 distinct clusters of glomeruli which serve as the first order processing centers for different odors [61]. Several types of neurons originate from the antennal lobe including local neurons, output neurons known as projection neurons, and centrifugal neurons. It is known that most of the olfactory receptor neurons are specialists, meaning they encode for specific odors such as pheromone com-

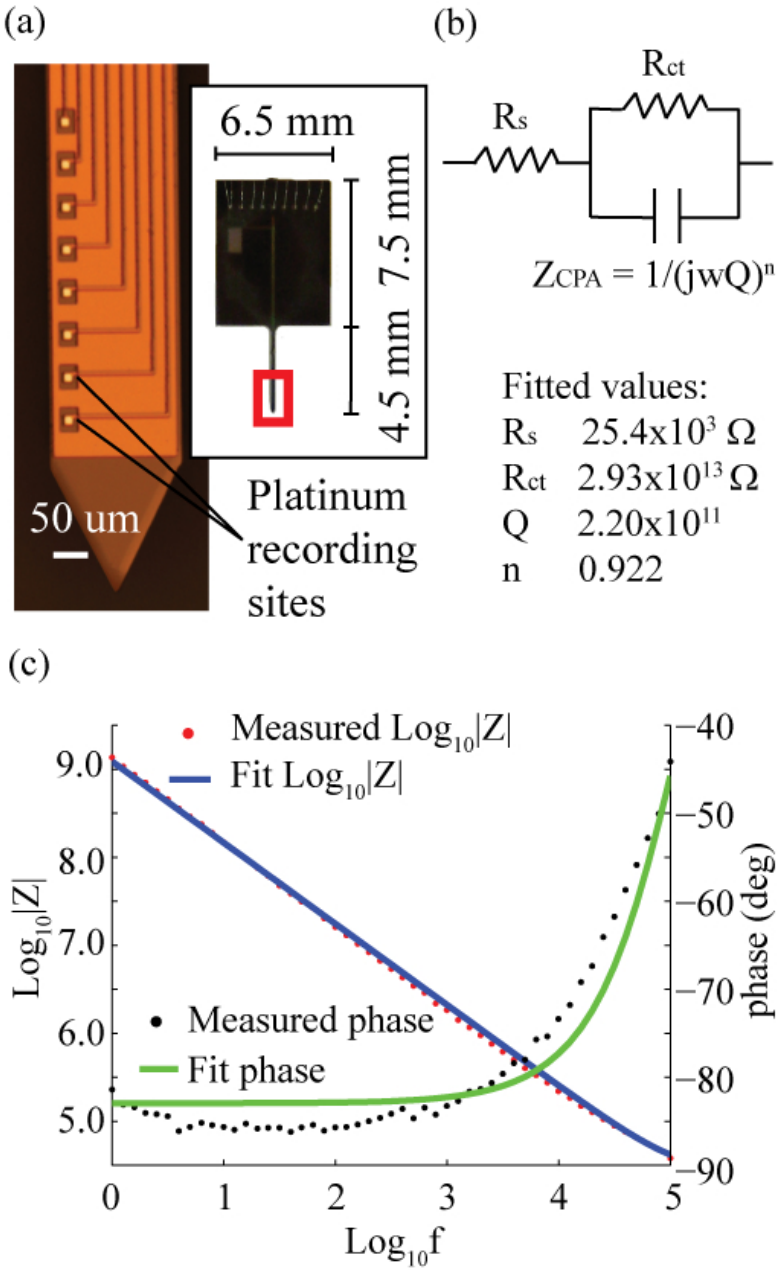

Figure 5.3: (a) Microfabricated silicon neural probe with eight platinum recording lines insulated with silicon nitride, and square 10 μm recording sites along the length of the probe for sensor (b) Simplified equivalent circuit and calculated equivalent parameters from fit of equivalent circuit model to measured impedance shown in (c). (c) Measured impedance data averaged over 3 consecutive electrochemical impedance spectroscopy (EIS) measurements and fit to the simplified model.

ponents. Furthermore, the glomeruli are organized into processing areas for different odorants. For example, it has been shown that the macroglomerular complex (MGC) is composed of glomeruli that specifically contain information relayed from olfactory receptor neurons responsive to pheromone components [61].

The insect used in our experiments *Manduca sexta* has been shown to have projection neurons that link the antennal lobe to other parts of the brain that are specifically responsive to certain pheromone components, including E10, Z12-16 as well as the pheromone component mimic E11, Z13-15 [63]. It is also known that these moths are responsive to tobacco, as a host plant of the insect [62].

5.4 Microprobe olfactory sensor

Male *Manduca sexta* late stage pupae reared at the Boyce Thompson Institute, Cornell University were used for the experiments. Short pulses of air mixed with target molecules were directed at the antenna of pupal stage male moths. One antenna was freed from the pupal cuticle, and the resulting opening in the pupal cuticle was sealed with wax.

As shown in Fig. 5.3, probes were designed such that the 10 μm by 10 μm recording sites matched the cell body diameter of 60% of the neurons in the lateral cluster in the antennal lobe [64]. Microprobes were inserted with a micromanipulator. As shown in Fig. 5.4, probes were directed towards the antennal lobe ipsilateral to the freed antenna. Fig. 5.4 shows a dissection of an adult sphinx moth revealing the brain structure [5], and Fig. 5.4 demonstrates the

location that was targeted with the probe insertions. These insertions were performed during the later stages of pupal development, to ensure robustness as an antennal cuticle does not form around the antennae until pupal stage twelve [65]. After initial insertions, the electrodes are coarse and fine positioned during development to find the strongest signals in the target brain volume.

To apply the olfactory stimuli, a setup similar to that presented in [64] was used. Charcoal filtered air (at a flow rate of approximately 0.05 liters per minute) was directed through a glass cartridge aimed at the insect antenna. To apply each stimulus, small pieces of filter paper containing dissolved stimulant were placed in a separate glass cartridge also directed towards the antenna. Using a relay controlled pinch valve, 300-400 ms pulses of air were diverted from the charcoal filtered normal air flow to the stimulus cartridge. Stimuli included the *Manduca sexta* host plant tobacco, major pheromone component E10Z12-16Al (Bombykal) [62], a mimic of another major pheromone component E11Z13-15Al ('C-15') [62], and clean air. Pheromone components were generously supplied by Prof. Jocelyn Millar (UC Riverside). Small pieces of tobacco leaves were placed directly into the cartridges for tobacco tests. Electrophysiological signals were amplified and filtered with a notch filter at 60 Hz using a commercial A-M systems Model 1800 amplifier with an 100 GΩ input impedance, and digitized at 10 kHz using a data acquisition board from National Instruments. Data were recorded using a PC with a custom LabVIEW code.

Pupal stage insertions allowed fine and coarse positioning of microprobes to determine locations with the strongest response signals. Probes inserted in the 14th pupal stage (P14) and maintained in a given location did not demonstrate antennal lobe tobacco responsiveness until the moth reached P16, indicating ol-

factory response development between the 14th and 16th stages (Fig. 5.1, right). This is supported by studies investigating the onset of antennal lobe responsiveness to various natural stimuli [65].

Recordings from P16 inserted probes in response to 300-400 ms air pulses containing various stimuli are shown in Fig. 5.5. The sensor demonstrates high specificity for tobacco, but is also weakly responsive to 6 ppb concentrations of bombykal, demonstrating a tobacco signal-to-noise ratio of greater than 10. This signal-to-noise ratio is defined as the ratio of amplitudes of the tobacco response to any other stimulus response. As shown in Fig. 5.5, the insect response is sensitive to the concentration and/or history of applied stimuli, as the magnitude of the response decreases over consecutive tobacco pulses.

Our method can potentially provided enhanced performance in reliability, specificity, and sensitivity by: 1) Measuring neural signals directly from the insect's first odor processing areas, the antennal lobes. These signals convey integrated information from neurons spanning the entire antenna (2-3 cm long, 1 mm wide) that are receptive to a specific odor. 2) EMIT pupal stage probe insertions which improves insect and neural integration. That is, EMIT enables development of the insect brain around the microprobes, rather than insertion into fully developed brains. Due to tissue-anchoring, EMIT avoids physical damage to the adult neural circuitry, and uses the highly active brain development during metamorphosis to heal any damage. As further brain growth occurs around probes, it is hypothesized that the small pupal motion reduces the shift in the position of the electrodes away from the desired neurons, making signal capture robust and reliable.

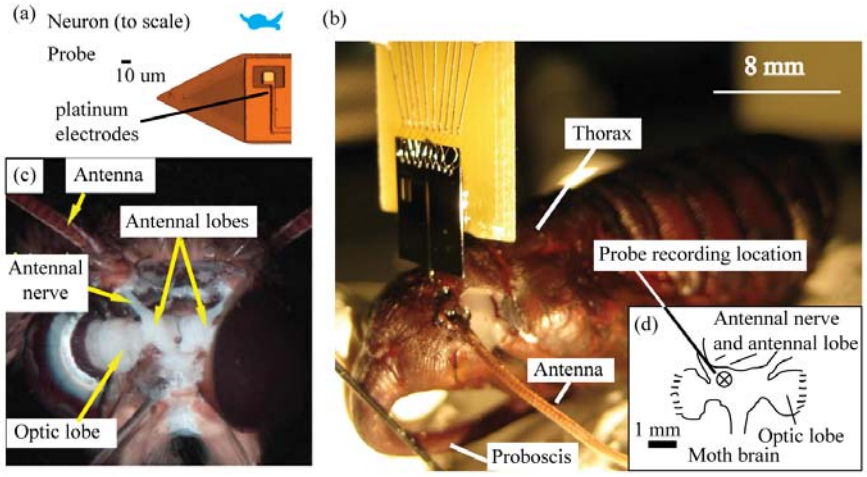

Figure 5.4: (a) Size comparison of probe tip and representation of neuron drawn to scale (b) Photograph of hybrid bio-electromechanical sensor system composed of microprobe inserted in Manduca sexta pupae using Early Metamorphosis Insertion Technology (EMIT) (c) Frontal view of brain of adult sphinx moth (adapted from [5]) (d) Diagram of insect brain.

5.5 Airborne olfactory sensor system and future directions

Having demonstrated the ability to record responses to various odorants, the feasibility of achieving an airborne olfactory sensor system is investigated. The necessary components would be a neural recording probe, an amplifier and wireless transmission system, and batteries. We have demonstrated that the silicon neural recording microprobes can be inserted in pupal *Manduca sexta* and are able to emerge with the probe still intact, as shown in Fig. 5.7. Additionally, based on prototype devices, as shown in Fig. 5.6, it is anticipated that an entire airborne system to be mounted on the insect could weigh approximately 87 mg without batteries.

While 12 mAh lithium batteries weigh 300 mg, which approaches the weight-bearing capacity of *Manduca sexta* insects, an even larger species has

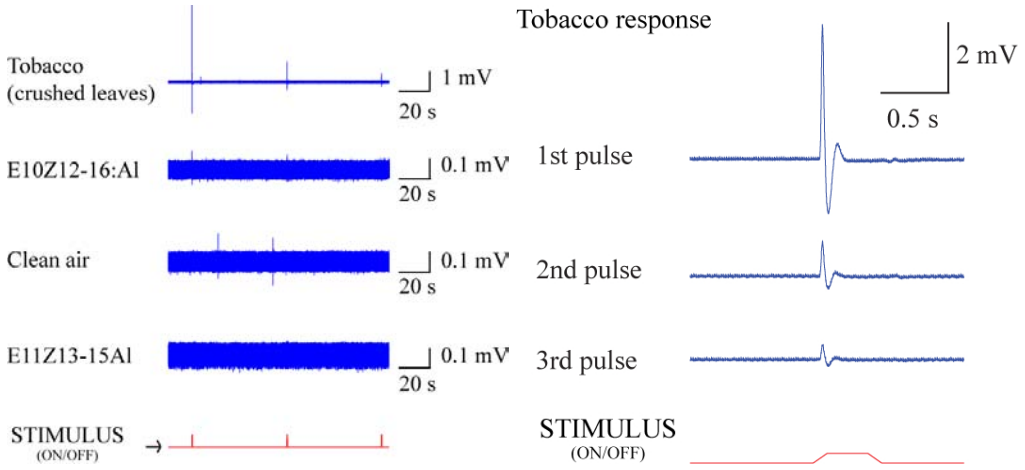

Figure 5.5: Recorded neural activity (blue, top traces) in response to indicated stimulus pattern (red, bottom trace) consisting of three 300-400 ms pulses of air mixed with target molecules. Measurements were recorded from male 16th pupal stage Manduca sexta. Strong responses to tobacco were observed at least 21 times, and weak-to-no responses to the pheromone and pheromone-mimic components E10Z12-16:Al and E11Z13-15:Al were observed, respectively. Measurements showed a tobacco response amplitude to non-tobacco response amplitude greater than 10.(right)Responses of 3 odor pulses separated by 60 s each. Decreasing amplitude of responses were seen with each consecutive pulse.

been investigated for flight carrying capacity. This moth, which has been found in the swamps of Florida, is called the Giant Sphinx moth and can carry greater than 1.1 grams without adversely affecting the insect's ability to generate enough lift to fly. Images from a video of the Giant Sphinx moth flying weight-loaded are shown in Appendix B. The Giant Sphinx moth can also carry a microcontroller and battery, as shown in Fig. 5.8 which could be used to transmit pulses to the insect for flight control.

With the *Manduca sexta* or Giant Sphinx moths, in order to achieve a reliable, specific olfactory system, it is necessary to create a large array of electrodes and develop a spatial map of the specific responses of particular neurons to classes

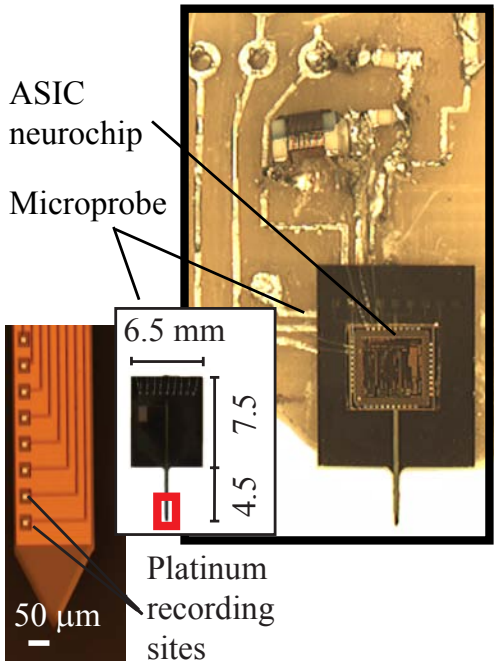

Airborne System Component	Weight
6 mil polyimide PCB	32 mg
ASIC neurochip	13 mg
Microprobe	42 mg
TOTAL	**87 mg**

Figure 5.6: Prototype integrated ASIC neurochip and microprobe

of odorants. While the feasibility of a hybrid insect olfactory sensor is demonstrated here, by integrating silicon probes and with the insect's ability to carry the necessary wireless transmission components, further investigation still remains in developing the precise neuronal maps. These effects are currently taking place but are expected to take another several years before this system can become realizable as a specific and sensitive hybrid olfactory sensor system.

Figure 5.7: Inserted silicon microprobe in pupal insect and adult insect after emergence with probe still intact (circled)

Figure 5.8: Giant Sphinx moth with microcontroller and battery on its back.

CHAPTER 6

MINIATURIZED ULTRASONIC HORN PROBES FOR NEURAL SENSING

6.1 Motivation: Developing miniature neural interfaces

Neural interfaces can be used to record large scale neuronal activity and the information extracted from these recordings can in turn be used to control prosthetics. Neural interface technology can provide a very promising solution to treating people with paralysis or lost limbs. By implanting electrodes which can record and stimulate neural activity with good spatial and temporal resolution, these technologies can help bridge a patient's cortical activity to limbs or external devices. However, immune reactions against the implants currently limit their effective lifetime.

Neurons only comprise approximately 25% of the brain tissue and the rest consists of glial cells and vasculature [15]. Within this environment, to achieve a useful neural interface, the requirements are a high signal-to-noise ratio, the capability to record from many units, and well-defined electrode spatial locations allowing post-processing of recorded signals to isolate distinct unit firing activity. Glial cells can take the form of oligodendrocytes, astrocytes, and microglia, each of which serve particular functions. Oligodendrocytes create myelin. Astrocytes and microglia are involved in the brain's immune response. Astrocytes compose 30-65 % of the glial cells, while microglia comprise 5-10 % of the total glial cells [15]. Astrocytes normally maintain the chemical environment and mechanically support neurons, while microglia can phagocytose and serve as cytotoxic cells. Both microglia and astrocytes change form when they become activated for immune responses.

Many researchers have qualitatively observed the loss of electrode function after chronic insertion in terms of a reduced to zero signal-to-noise ratio. Studies indicate two main types of reactions resulting from electrodes. The first results from the initial insertion trauma which can involve severing of capillaries, the extracellular matrix, and cell processes [15]. It has been observed the initial insertion trauma causes hemorrhage and edema. Additionally, it causes a microglial response which can fade, in some cases, after a few weeks. This phenomenon of an initial insertion trauma response is supported by control studies which examine the impact of electrode stab wounds on tissue and demonstrate little trace of electrode tracks several months after the stab wounds. The initial microglial response is followed by a chronic foreign body response where cell morphology and behavior change to reactive glial type cells. These glial cells most commonly form a glial scar surrounding the electrode a few weeks after insertion. This can be instrumented by microglia, in some cases, or astrocytes. Reactive astrocytes can be monitored in particular by observing the change in morphology with an increased expression of glial fibrillary acid protein (GFAP). Many immunostaining studies target this protein in studying immune response to implanted tissue, by inserting electrodes and sacrificing animals at various time points. Various studies have pointed to different foreign body response reactions to electrode insertions, depending on insertion material, type, and other conditions and limited to a small subset of animals. These make it difficult to define the ultimate solution for successful neural interfaces. However, as the immune reaction is caused by the presence of foreign material in the body, various strategies have been proposed and attempted to reduce the immune reaction and increase the lifetime of the electrodes. Varying electrode shape, material compatibility, size, bioactive coatings, micro-motion, and elasticity may influ-

ence the biological response to the inserted electrodes.

6.2 Effect of microelectrode materials, coatings, and bioactive molecules

One area of interest in neural interface research is developing electrode materials whose mechanical compliance better matches that of the tissue. Current silicon probes, and even polyimide electrodes, have orders of magnitude greater stiffness than biological tissue, which can add to tissue damage and edema resulting from minute changes in electrode position. Thinner and less stiff materials are being investigated to determine their effect on reducing tissue immune reactions. However, one of the challenges of using very thin, flexible materials is proper insertion of the electrodes to the areas of interest. While dissolvable silk with patterned thin electronics has been used for neural recordings, these films have only been placed on the surface of the cortex [14]. One method suggested for electrode insertion is a magnetic tension-based insertion system with a magnetic tip on the electrode [16].

Another area that can affect tissue coupling, demonstrated in tissue cultures, is defining nanotopology on the surface of the electrodes. In cultures, features such as platinum patterned with nanopyramids have been shown to affect neuron orientation and growth [66]. This effect arises from cells receiving biological cues not only at the macroscale but also at the microscale. Integrins, or proteins used by cells to adhere to surfaces, in particular, are nanoscale interaction sources. Studies have also investigated various bioactive coatings to promote neuronal adhesion and growth, as well as repel glial cells to pattern preferential

growth of astrocytes away from electrode areas. However, astrocytes may be able to create an environment to grow equally well despite changes in surface chemistry [67]. Bioactive coatings may also help reduce the initial impedance of the patterned electrode sites so viable recordings can be taken for a longer time.

The effect of silicon electrode tip shape has also been investigated as a potential way to reduce damage to cells. It has been shown that a chisel-point silicon electrode tip shape can produce a kill zone of less than 10 μm [68]. Additionally, electrode insertion velocity may have an effect on tissue response. Strategies have been developed to allow insertion of 100 electrodes simultaneously while producing no significant long-term damage [69].

Clearly, there are many challenges in terms of achieving repeatable reactions to inserted electrodes and creating viable solutions to allow decades long high quality electrical recordings from neural interfaces. However, by developing quantitative methods to assess tissue-electrode reactions in-vivo and ex-vivo in large numbers of animals, we can seek to better understand the problem at hand. In this section, the concept of ultrasonically actuated neural probes is presented. The insertion force reduction properties of ultrasonically driven probes has been discussed in previous chapters. This property and the reduced residual stress in the substrate after ultrasonic probe insertion provide an interesting tool for studying the effect of insertion forces and strain on long-term neural interfaces.

6.2.1 PEDOT coating of electrodes

One solution to deal with increased electrode impedance resulting from immune reactions is using conductive polymer coatings. Conductive polymers can decrease the initial impedance of electrodes, and also serve to reduce the required electrode size in order to record from a given area [70]. Additionally, conductive polymer coatings, such as Poly(3,4-ethylenedioxythiophene) (PEDOT) can increase the charge injection capability of a material [71]. When inserted for long-term neural recordings, PEDOT coated electrodes exhibit a lower electrode site impedance versus uncoated electrodes for a period of at least 40 days post surgery, after an initial swelling period disappears [72].

In this section, the effect of PEDOT coating microfabricated platinum evaporated electrodes on electrode impedance is studied. Platinum electrodes with dimensions of 35 μm by 35 μm were patterned and fabricated. Cyclic voltammetry was performed on the electrode sites to clean the sites prior to measuring the initial electrode impedance. The electrodes were immersed in saline, with a platinum 1 cm x 2 cm counter electrode and a Ag/AgCl reference electrode. Electrochemical impedance spectroscopy is performed on a platinum electrode site three times and the measurements are averaged. PEDOT is mixed using 250 mg of poly(styrenesulfonate) salt, or PSS Na, 35 mg of ethylenedioxythiophene (EDOT), and 25 mL of deionized water. The electrode site is coated with PEDOT using chronopotentiometry with a Gamry FAS2 potentiostat. A constant current of 6 nA for 833 seconds is used for a deposition charge of 400 mC/cm^2. The measured impedance and phase before and after PEDOT coating are shown in Fig. 6.1. From the measured impedance, it is clear that with PEDOT coating the impedance decreases from 278.6 kΩ to 10 kΩ at 1 kHz. The phase also

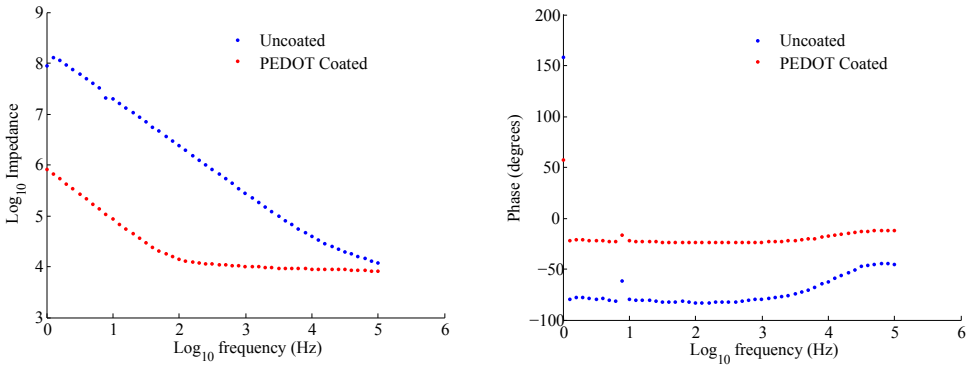

Figure 6.1: Measured impedance and phase of uncoated and coated platinum electrodes.

becomes less capacitive with PEDOT coating and shifts to closer to 0°.

6.3 Miniaturized ultrasonic horn probes for quantifying neural interface failure mechanisms

In previous chapters, the ability of ultrasonic horn probes to reduce the penetration force required to enter substrates of various elasticities was discussed, and a theoretical model with fitted parameters was presented. The model allows prediction of the effective forces that will be encountered by the electrodes during insertion. The force-reduction properties of these probes during ultrasonic actuation can allow investigation of the effect of initial maximum penetration force and residual stress during insertion of neural interfaces. Additionally, the effect of probe micromotion during long-term insertions can be investigated with integrated strain and pressure sensors.

6.3.1 Neural ultrasonic horn design and simulated performance

The design of the miniaturized ultrasonic horn probe is similar to the cardiac ultrasonic horn probes, following a geometry profile of a catenoidal horn defined by:

$$A(x) = A_1 * cosh^2[\alpha(L - x)] \tag{6.1}$$

where

$$\alpha = \frac{acosh[\sqrt{\frac{A_0}{A_1}}]}{L} \tag{6.2}$$

Finite element simulations of the ultrasonic neural probes indicate that the longitudinal resonance frequency is much higher than for the cardiac probes, as expected, since:

$$\omega_r = \sqrt{\frac{k}{m}} \tag{6.3}$$

In particular, the width and length dimensions are scaled down by a factor of four versus the cardiac probes, as shown in Fig. 6.2. The resulting resonance frequency is approximately four-fold higher.

The resonance frequency shifts as the length of the probe is adjusted, as expected. Additionally, the normalized degree of longitudinal displacement can be shifted by varying the length of the probe as seen in Fig. 6.3 with shown lengths of 2.2, 3.2, and 4.2 mm. The tip of the probes experience little relative displacement.

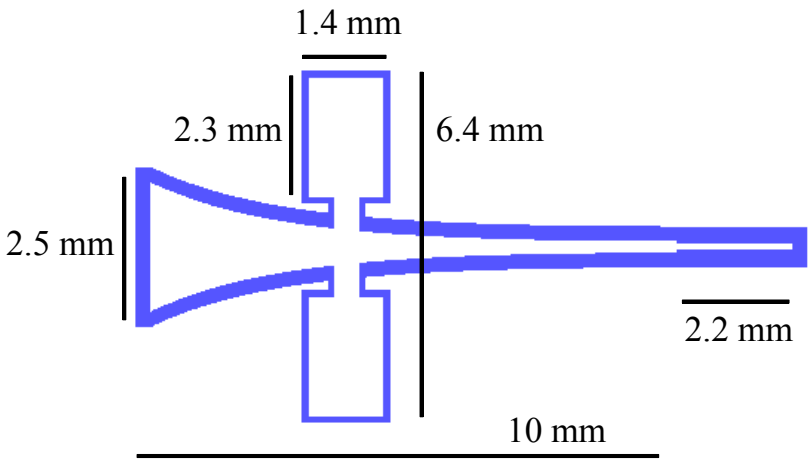

Figure 6.2: Dimensions of miniaturized neural ultrasonic horn probe.

For the miniature ultrasonic horn probes, the added mass of the PZT is quite large in comparison to the mass of the ultrasonic horn. Including the mass of the PZT in the simulations results in a shift of 20-30 kHz in the resonance frequencies. The simulation results are shown in Fig. 6.4. Though a shift in resonance frequency is seen, the normalized longitudinal displacements for given probe tip lengths remain constant.

6.3.2 Neural ultrasonic horn fabrication and performance

The miniaturized ultrasonic horns can be fabricated with integrated strain gauges, much like the cardiac probes. Since the dimensions of the neural horn probes are very small, the cardiac horn fabrication process flow is modified to use DRIE release of devices, rather than potassium hydroxide etching [20]. KOH etching typically provides a sidewall angle of 54.7°. For a 500 μm thick wafer, this means a lateral etch width of 354 μm over which the ¡111¿ plane is

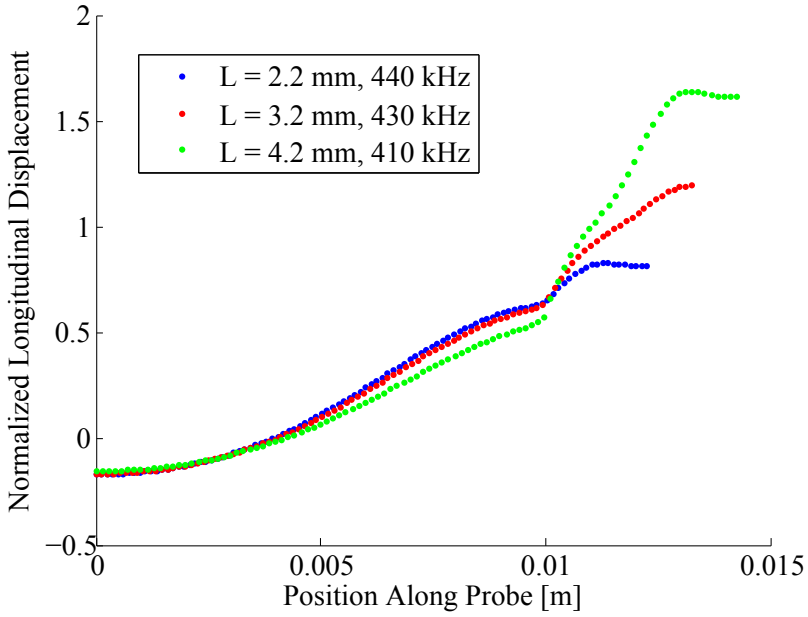

Figure 6.3: Simulated longitudinal resonance frequencies and displacement profiles for probe tip lengths of 2.2, 3.2 and 4.2 mm.

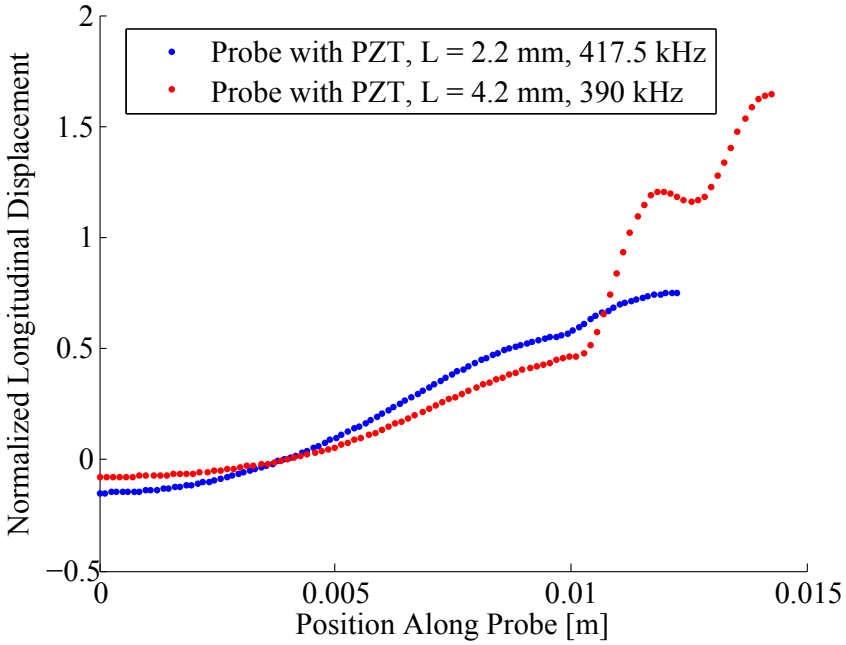

Figure 6.4: Simulated longitudinal resonance frequency for probe with PZT attached and a probe tip lengths of 2.2 mm and 4.2 mm.

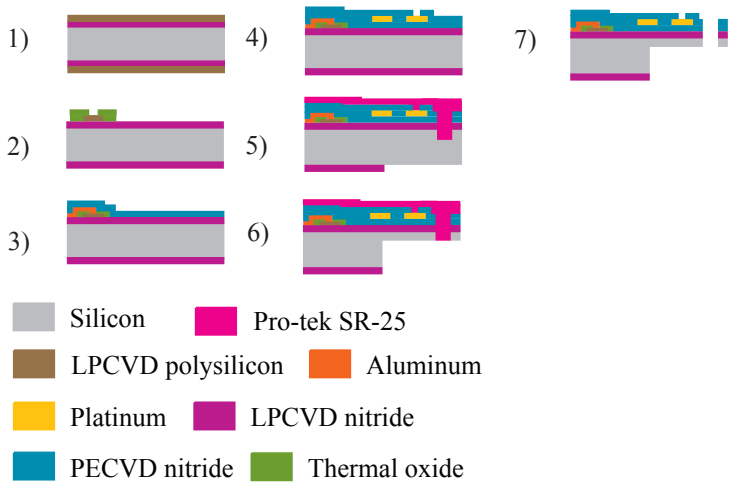

Figure 6.5: Process flow for fabricating silicon platinum electrodes with integrated strain gauges.

exposed. In comparison, sidewall aspect ratios of 50:1 and 100:1 can be achieved with DRIE. The process flow with DRIE etch release is shown in Fig. 6.5, and utilizes a viscous coating Pro-tek SR-25 that can be spun on the wafers and baked to create a glassy material that can withstand RIE and DRIE etching. The Pro-tek material can later be removed in a special Pro-tek remover solvent.

An optical interferometer was used to measure the resonance characterstics of assembled neural ultrasonic horn probes. The resulting scan for an ultrasonic horn with a probe tip length of 2.2 mm and driven with a 5 Vpp driving sine wave is shown in Fig. 6.6. The measured resonance peak is 430.2 kHz compared with the simulated resonance frequency of 417.5 kHz. This difference may arise from etch anisotropies in the fabrication process.

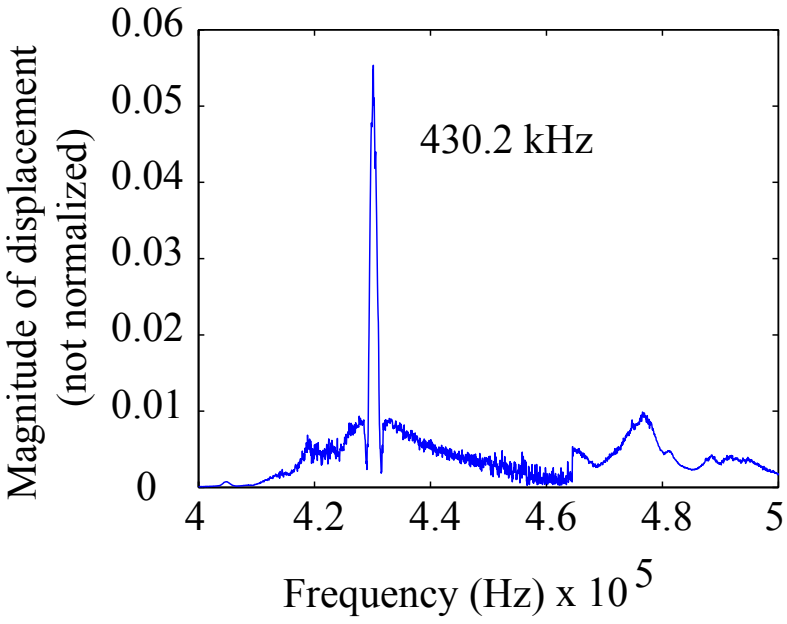

Figure 6.6: Optical interferometer scan of longitudinal displacement of miniature ultrasonic horn probe with 5 Vpp driving voltage.

6.3.3 Miniature neural and ultrasonic horn probes for mice neural recordings

Two types of electrodes have been fabricated for mice neural recordings. Ultrasonic horn based electrodes can allow study of insertion force, initial insertion trauma and strain, and square neural electrodes can allow investigation of electrode coatings and strain (Fig. 6.7). Both probes have integrated strain gauges as well as platinum recording sites.

As shown in Fig. 6.8, the electrodes can be used to record potentials from mice. In this recording, a small 5 mm hole is opened in the mouse skull with the mouse under anesthetization. The electrode is inserted to a depth of 2 mm to target the hindpaw region of the cortex. Two small needles are inserted in the

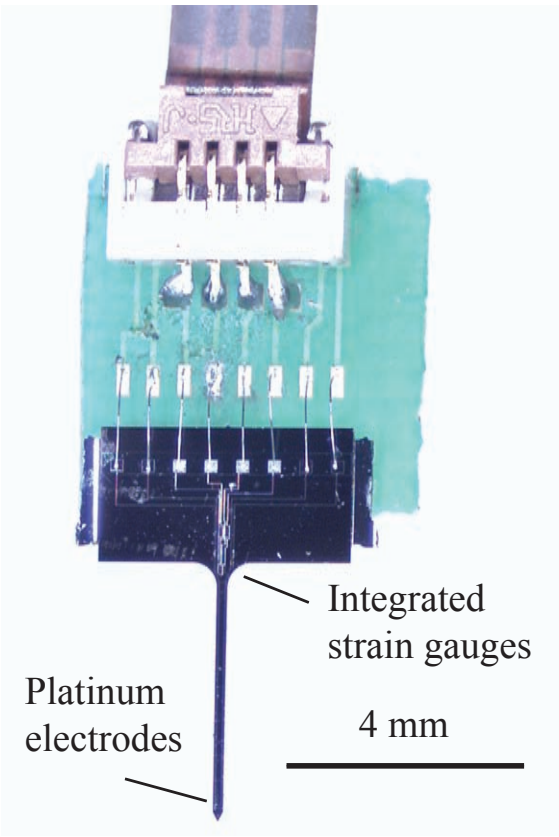

Figure 6.7: Miniature neural electrodes with integrated strain gauges.

hindpaw of the mouse and a current pulse is provided to the mouse. While the stimuli are being applied, the potentials in the hindpaw region of the brain are recorded using the microfabricated electrodes. The whole setup is enclosed in a grounded Faraday cage.

6.3.4 Probe modifications to promote biocompatibility

Including holes in the probe tip may help promote biocompatibility or allow for better signal transduction. Sieve electrodes have been often used in nerve regeneration studies and peripheral nerve recording and have demonstrated

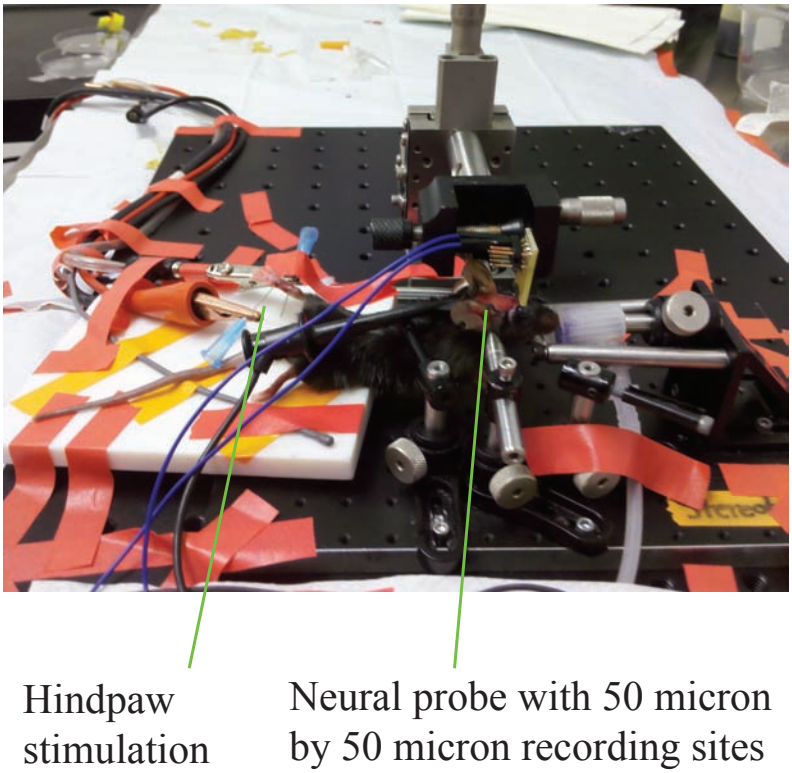

Figure 6.8: Setup for recording potentials from hindpaw region of brain and stimulating hindpaw of mouse.

promising results in allowing neurite growth and good electrical contact [73]. Additionally, other strategies have developed dual-sided electrodes to compensate for lack of signal transduction from the back-side of single-sided electrodes [74].

In this section, developed probes are presented with integrated holes to test the hypothesis that these holes may allow for better signal transduction and biocompatibility. A straighforward modification to the lithography masks for the fabrication process flow allows through DRIE etch of holes in the probe tips. The holes are defined in the frontside etch mask and first etched to a depth of 140 μm. Then holes are then released from the backside DRIE release etch. The

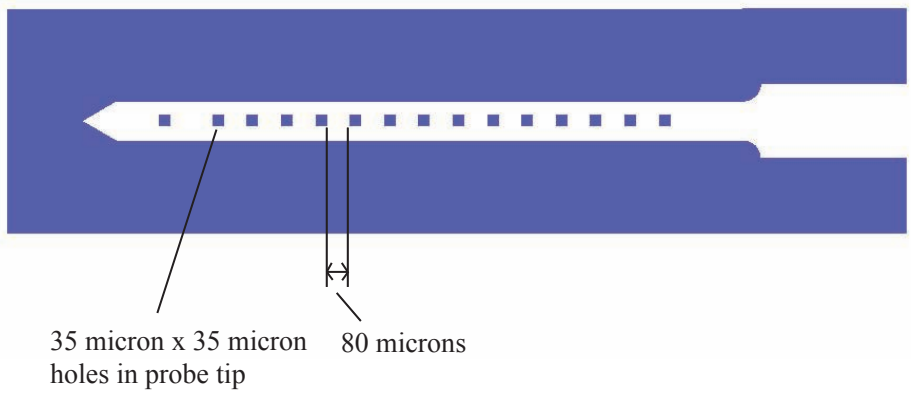

Figure 6.9: Dimensions of probe with holes.

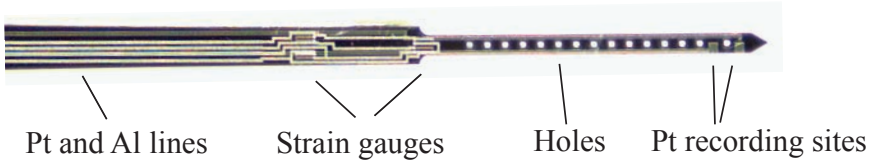

Figure 6.10: Microphotograph of fabricated probe with holes.

integrated holes have dimensions as shown in Fig. 6.9. A microphotograph of a fabricated probe with holes and platinum recording sites with integrated strain gauges in shown in Fig. 6.10. Based on finite element simulations, the expected longitudinal resonance frequency is approximately 440.478 kHz for the probe with holes, compared to 440 kHz without holes. The compared longitudinal displacements are shown in Fig. 6.11.

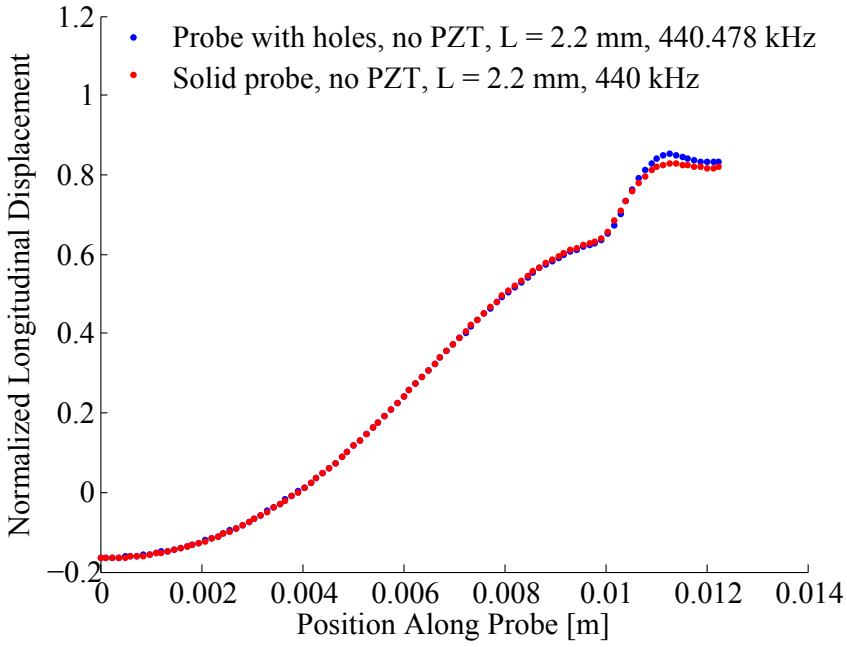

Figure 6.11: Finite element simulation of longitudinal displacement and resonance frequency with and without holes.

6.4 Future directions

The presented miniature ultrasonic horn probes with integrated strain gauges and holes can allow study penetration forces for neural interfaces and strain and electrical conditions over time. The probe ultrasonic motion can be decoupled from mouse skull movement by fixing the PCB which is attached to the zero-displacement node of the probe to the mouse skull, as shown in Fig. 6.12.

With this developed system, several hypotheses and open problems can be investigated. First, the effect of initial insertion trauma can be investigated by monitoring immune reactions and electrode impedance with ultrasonically driven probes and non-ultrasonically driven probes. Two-photon microscopy can be used to observe the immune behavior with genetically-modified animals. Second, the degree of strain and micromotion of the probe can be moni-

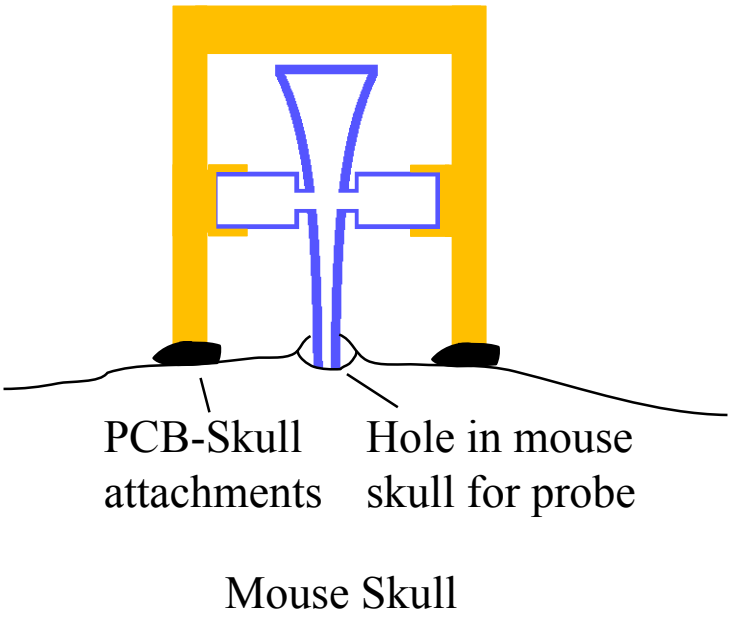

Figure 6.12: Proposed ultrasonic horn and skull attachment to de-couple ultrasonic motion from skull motion.

tored with integrated strain gauges. This can allow a first order assessment of how much movement-associated damage may be present in the tissue. Third, the electrical sites on the probes can be used to monitor change in electrical impedance over time as well as change in neuronal spike activity including change in spike rate and peak-to-peak voltage. Spike sorting algorithms can be implemented to track the signals from given neurons over time and how these progress given different initial insetion conditions. Insights from these experiments can help guide design and development of more robust neural interfaces.

CHAPTER 7

TIME-DIVISION MULTIPLEXED WIRELESS TRANSMISSION SYSTEMS FOR APPLICATIONS IN NEURAL SENSING

7.1 Motivation

In the previous chapters, an amplifier and wireless transmision system has been presented for cardiac action potentials. Wireless transmission can allow study from animals during normal activity by eliminating wires that would limit the range of movement of the animals. The design and performance of a time-division multiplexing system for neural sensing is discussed. This system will be used for amplification and wireless transmission of neural signals from a mouse system to be mounted on a backpack on the mouse back.

7.2 Multiplexed neural amplifier and wireless transmission system

For neural amplification and wireless transmission, the amplifier should have a bandwidth of at least 10 kHz with an input-referred noise level below that of neural signals which can be approximately 100 μVpp in amplitude. This chip is designed to amplify and wirelessly transmit these small amplitude signals, as well as allow multiplexed wireless transmission of four amplifier channels. In this design, the low-voltage CMOS C35 Austria Microsystems process is used instead of the H35 high-voltage process used in the previous design. The layout of the chip is shown in Fig. 7.1 and measures 3 mm by 3 mm.

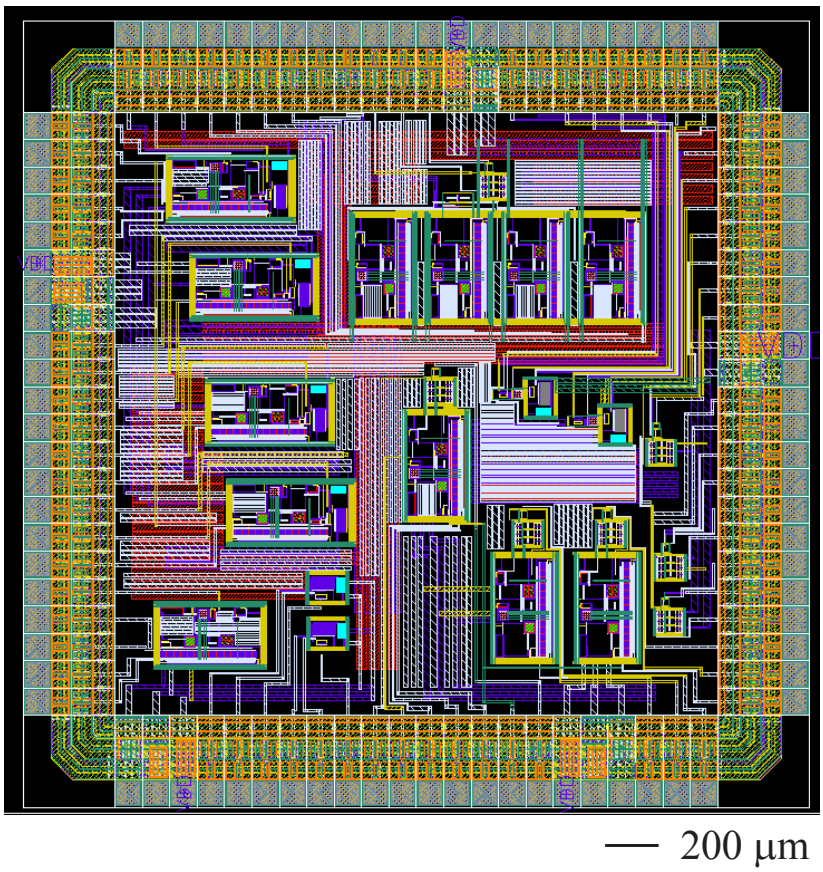

Figure 7.1: Layout of multiplexed neural amplifier and oscillator chip.

7.2.1 Amplifier design and noise considerations

The design of the amplifier consists of a differential amplifier first stage followed by a common source second stage, shown in Fig. 7.3. The simulated gain and frequency of the amplifier are shown in Fig. 7.2.

Noise contributions come from both flicker noise and thermal noise, and guide the design of transistors to minimize noise. The thermal noise contribution from a resistor is given by

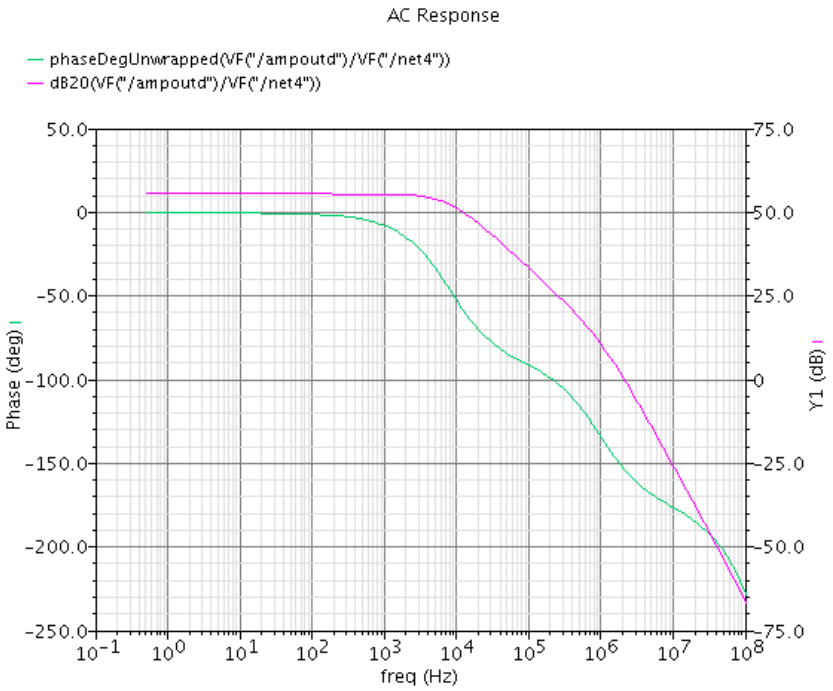

Figure 7.2: Amplifier simulated gain and phase.

$$\overline{V_n^2} = 4kTR \tag{7.1}$$

The flicker noise contribution from a MOSFET is given by

$$\overline{V_n^2} = \frac{K}{C_{ox}WL}\frac{1}{f} \tag{7.2}$$

and the thermal noise contribution is given by

$$\overline{V_n^2} = 4kT(\frac{2}{3}g_m)r_o^2 \tag{7.3}$$

An expression for the thermal noise contributions from the various transistors can be derived

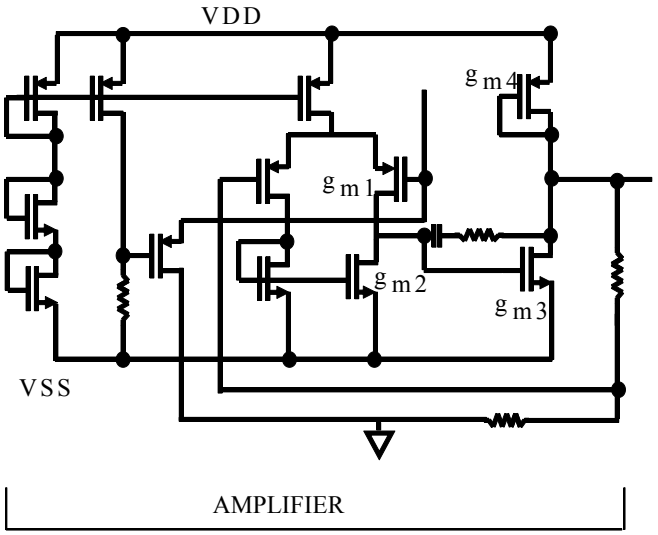

Figure 7.3: Schematic of amplifier.

$$\overline{V_{n,out}{}^2} = \frac{8kT}{3g_{m1}}(1 + \frac{g_{m2}}{g_{m1}})A_1A_2 + \frac{8kT}{3}(g_{m3} + g_{m4})A_2 \tag{7.4}$$

where A_1 and A_2 are the gain of the first and second stages. The equivalent input referred noise is then given by

$$\overline{V_{n,in}{}^2} = \frac{\overline{V_{n,out}{}^2}}{A_1{}^2A_2{}^2} \tag{7.5}$$

Since the gain of the first stage is large, the main noise contribution comes from the first stage. Since the transconductance g_m is proportional to $\frac{W}{L}$, the noise can be minimized by making the transistors large and by increasing g_{m2} relative to g_{m1}. The input-referred noise contribution is optimized with simulations and a value of 1.605 μVrms is obtained for a 0 to 20kHz bandwidth when extracted from the layout with pa rasitics. The equivalent input noise spectrum is shown in Fig. 7.4.

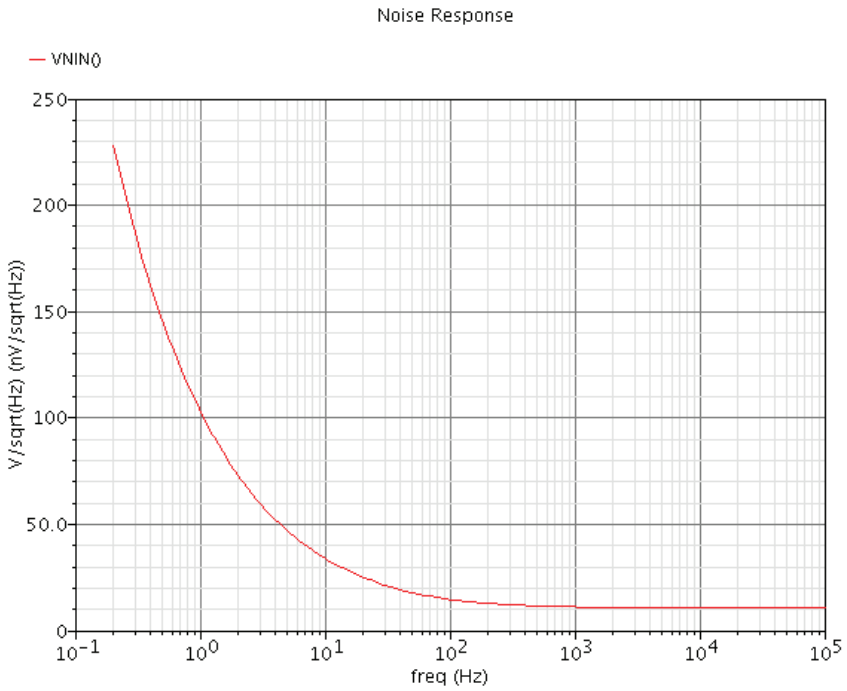

Figure 7.4: Equivalent input noise of amplifier.

7.2.2 Multiplexed design and voltage controlled oscillators

In this design, transmission gates are used to control which amplifier channel is fed to the voltage controlled oscillator, as shown in Fig. 7.5. The simulated switching for 2 channels with switching voltages S1 and S2 is shown in Fig. 7.6. One input channel is set to a DC voltage of 0.5 V and the other channel is set to a DC voltage of 0 V.

Both Colpitts and ring oscillators are implemented in this chip. As the Colpitts design has been discussed in previous chapters, the design of the ring oscillator only is discussed here. A differential ring oscillator layout is used, as shown in Fig. 7.7. The oscillation frequency is tuned by changing the control voltage on the load transistors, as shown in Fig. 7.8. The output waveform

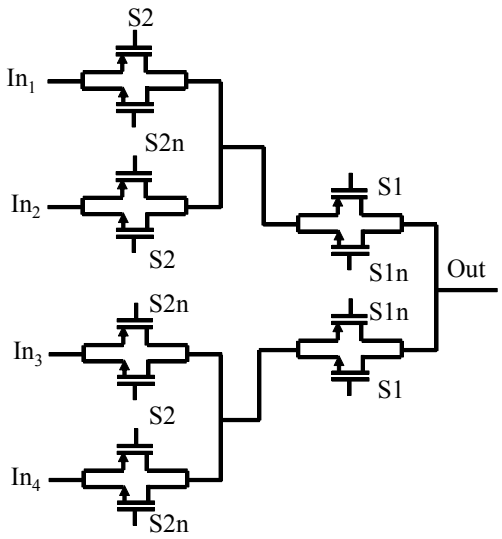

Truth Table

S1	S1n	S2	S2n	Out
0	1	0	1	In1
0	1	1	0	In2
1	0	1	0	In3
1	0	0	1	In4

Figure 7.5: Transmission gates used to control which amplifier channel is fed to the voltage controlled oscillator.

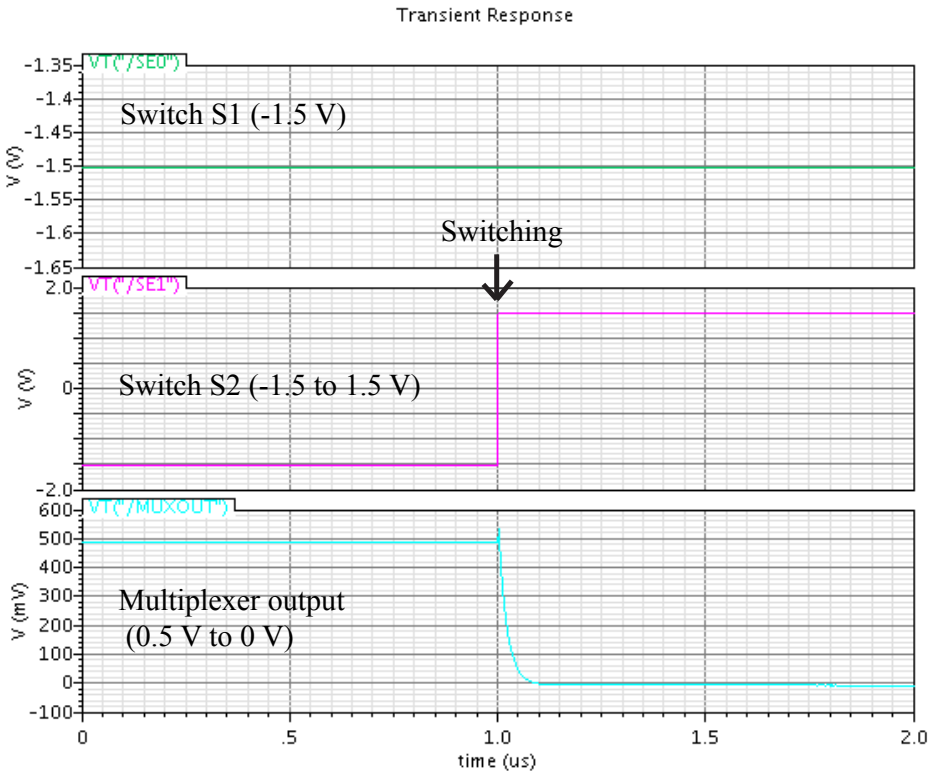

Figure 7.6: Multiplexer output with switching voltages S1 and S2.

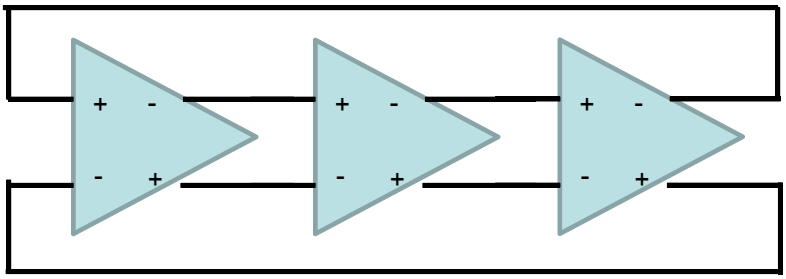

Figure 7.7: Schematic of differential ring oscillator layout.

from the ring oscillators is shown in Fig. 7.9 at a frequency of 72 MHz. The same input voltages used in Fig. 7.6 were multiplexed then sent as control voltages to the ring oscillator. This produced the output frequency shift shown in Fig. 7.10.

7.2.3 Measured performance

A custom PC board was designed to test the packaged chips, as shown in Fig. 7.11. The measured gain of the amplifier is as shown in Fig. 7.12. The wirelessly transmitted and received signals using the ring oscillator are shown in Fig. 7.13 [6]. The measured oscillation frequencies are 82-84 MHz.

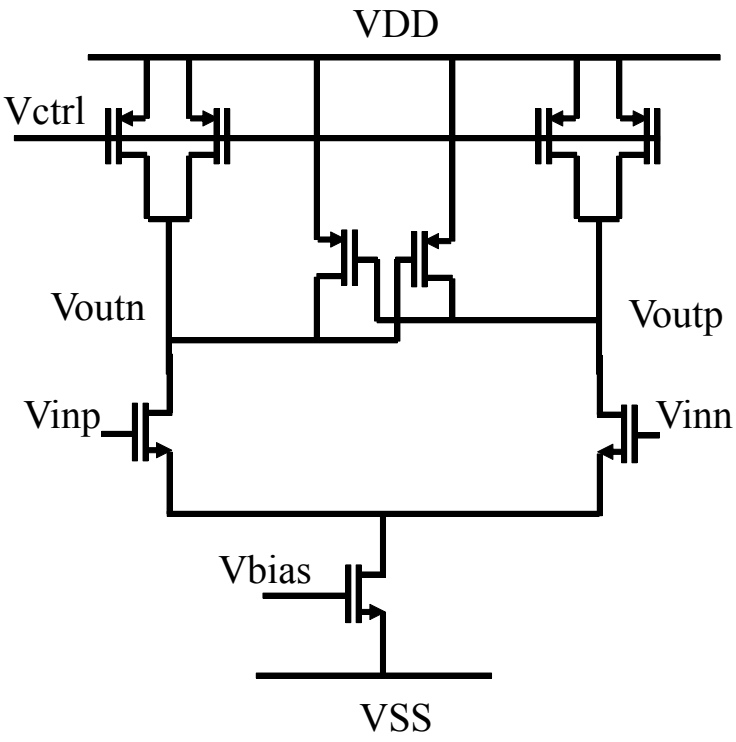

Figure 7.8: Schematic of each ring oscillator stage.

7.3 Future directions

Further testing and development is in progress to use this chip for amplification and wireless transmission on board a mouse system. The system will include the ultrasonic horn probe in the skull, and a backpack on the mouse to carry PC boards with the radio, the battery, and other circuitry, as shown in Fig. 7.14. With this system, neural signals can be recorded during normal mouse activity over extended periods of time to study neural interface failure mechanisms and modifications to promote biocompatibility.

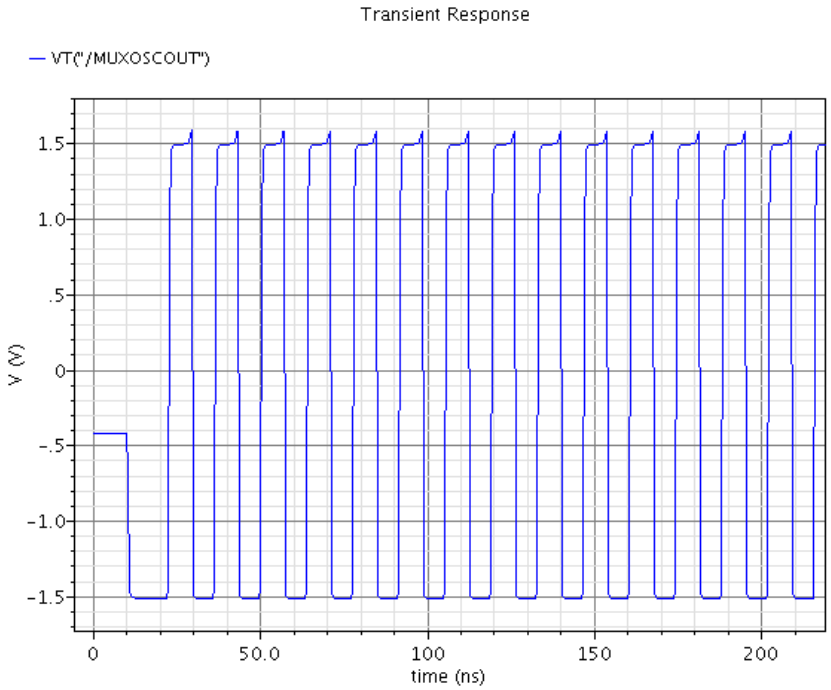

Figure 7.9: Simulation of transient oscillation from ring oscillator.

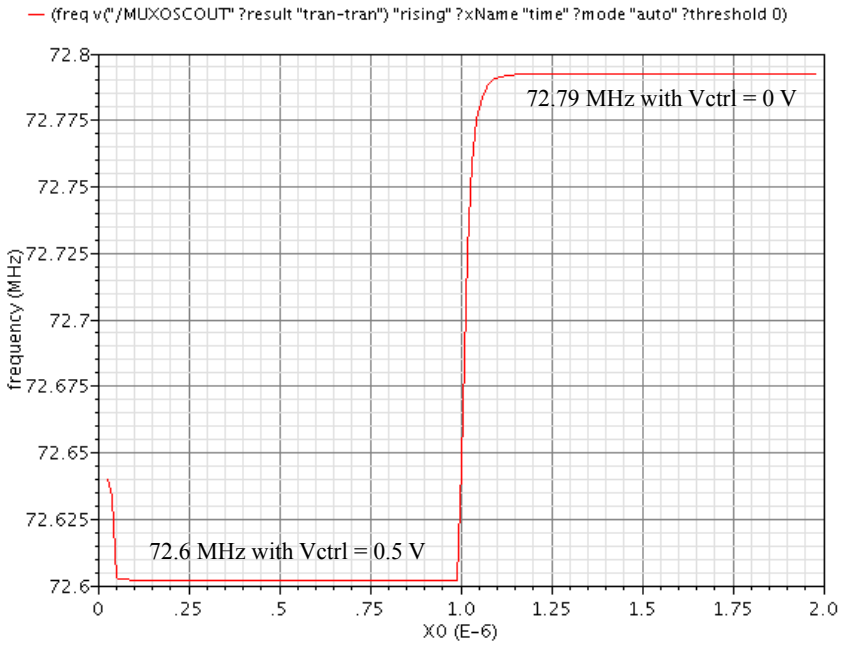

Figure 7.10: Ring oscillator shift in frequency with multiplexed output and shift in control voltage

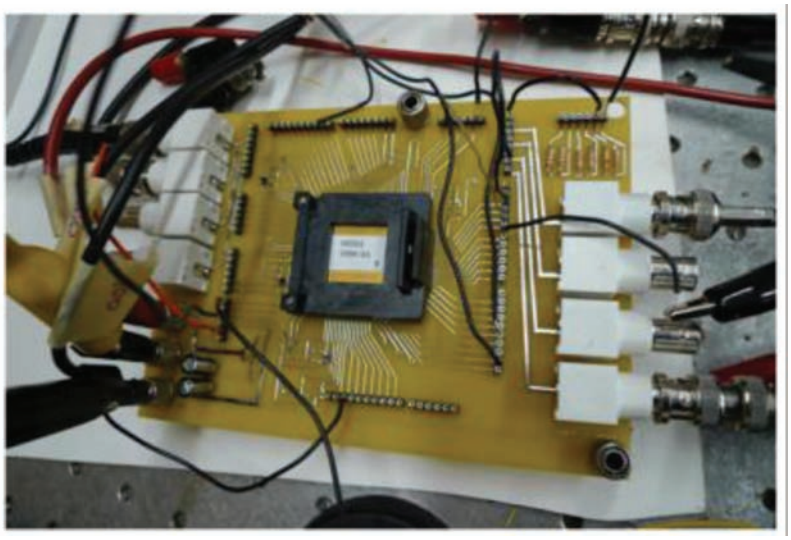

Figure 7.11: Custom PC board used to test chip [6].

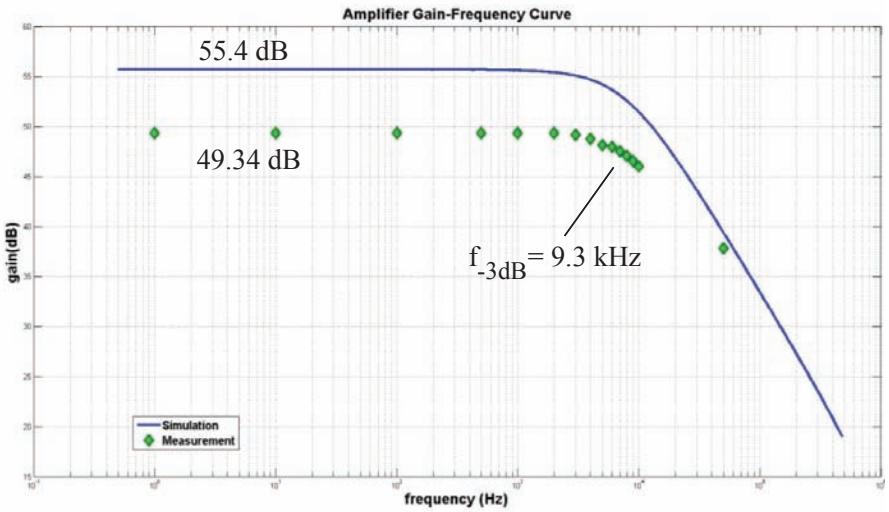

Figure 7.12: Measured and simulated amplifier gain [6].

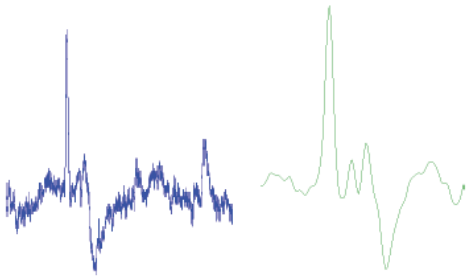

Figure 7.13: Wirelessly transmitted (left) and received (right) signals with ring oscillator [6].

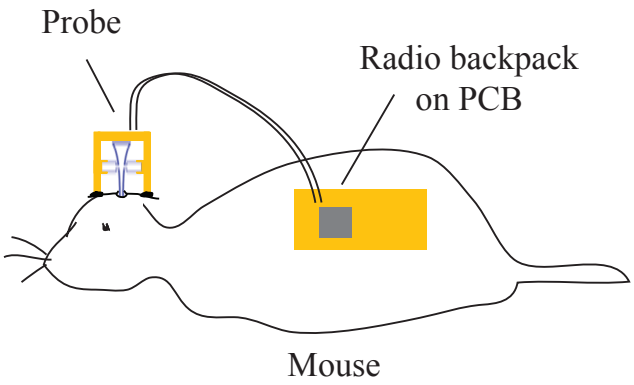

Figure 7.14: Backpack with radio to amplify and transmit neural signals recorded with probe inserted in mouse brain.

APPENDIX A

MICROCONTROLLER CODE FOR 8:1 MULTIPLEXERS

Arduino Mega-2560 code for controlling 8:1 multiplexer

```
void count(void);
int times = 1;
int enable;
int CONTROL = 1;
double val;

const int EN = 13;
void setup()
{
 Serial.begin(9600);
 //pinMode(0,INPUT);
 //pinMode(9,OUTPUT);
 pinMode(2,OUTPUT);
 pinMode(10,OUTPUT);
 pinMode(11,OUTPUT);
 pinMode(12,OUTPUT);
 pinMode(EN,OUTPUT);
 pinMode(7,OUTPUT);

 analogReference(EXTERNAL);
 attachInterrupt(5,count,RISING);
  digitalWrite(EN,HIGH);
  tone(2,16000);
 Serial.println("WHICH LINE ?");
}

void loop()
{


 switch (CONTROL)
 {

  case 1:
        digitalWrite(10,LOW);  // A2
        digitalWrite(11,LOW);  // A1
        digitalWrite(12,LOW);  // A0
        break;

case 2: //digitalWrite(9,LOW);
        digitalWrite(10,LOW);
        digitalWrite(11,LOW);
        digitalWrite(12,HIGH);
         break;

case 3: //digitalWrite(9,LOW);
        digitalWrite(10,LOW);
        digitalWrite(11,HIGH);
        digitalWrite(12,LOW);
        break;

case 4: //digitalWrite(9,LOW);
        digitalWrite(10,LOW);
        digitalWrite(11,HIGH);
        digitalWrite(12,HIGH);
         break;

case 5: //digitalWrite(9,LOW);
        digitalWrite(10,HIGH);
        digitalWrite(11,LOW);
        digitalWrite(12,LOW);
        break;

case 6: //digitalWrite(9,LOW);
        digitalWrite(10,HIGH);
        digitalWrite(11,LOW);
        digitalWrite(12,HIGH);
         break;

case 7: //digitalWrite(9,LOW);
        digitalWrite(10,HIGH);
        digitalWrite(11,HIGH);
        digitalWrite(12,LOW);
        break;

case 8: //digitalWrite(9,LOW);
        digitalWrite(10,HIGH);
        digitalWrite(11,HIGH);
        digitalWrite(12,HIGH);
        break;

  }
}
 void count()
 {



 if(CONTROL <= 7 && times < 2)
  {
   CONTROL++;
   times++;
  }
 else if(times >1)
  times = 1;
 else if(CONTROL > 7 && times < 2)
   {CONTROL = 1;
    times++;
   }

}
```

APPENDIX B

MATLAB DEMULTIPLEXING CODE

MATLAB code for demultiplexing multiplexed cardiac signals

```
%% This file reads in multiplexed data and demultiplexes and plots the data
%% Ching-Ping Janet Shen, August 2011

close all
clear

%% Data is saved in columns for each different probe
%% Two samples are taken per multiplexer switching to account for charging
%% times (switchc is used to select whether to use the first or second
%% sample)
filename = 'rec030';
probe = '3';
switchc = 1;
% Write demultiplexed outputs to file?
write = 1;

% read in multiplexed file
M =
dlmread(sprintf('C:\\Users\\MEMS\\Documents\\Janet\\Cardiac\\72811_microcontroller\\%s.txt',filename),'\t');

N = M(:,str2double(probe));

% Specify data acquisition rate
sampling = 16000;
time = (0:1/sampling:(length(N)*1/sampling-1/sampling))';

% Specify effective number of channels (2 samples taken for each of 8
% channels means 16 samples per cycle)
nchannels = 16;
n = 1;
S = zeros(nchannels, floor(length(N)/(nchannels*n)));
Stime = zeros(nchannels, floor(length(N)/(nchannels*n)));
counter = 0;
index = 0;
for i = 1:floor(length(N)/(nchannels*n))
   counter = counter + 1;
   for j = 1:nchannels
      index = index + 1;
      S(j,counter:(counter+(n-1))) = N(index:(index+(n-1)),1);
      Stime(j,counter:(counter+(n-1))) = time(index:(index+(n-1)),1);
   end
end

%% Plot extracted samples taken for first time point (switchc = 0)
figure;
hold on;
plot(Stime(1,:),S(1,:),'b')
plot(Stime(3,:),S(3,:),'r')
plot(Stime(5,:),S(5,:),'g')
plot(Stime(7,:),S(7,:),'k')
plot(Stime(9,:),S(9,:),'m')
plot(Stime(11,:),S(11,:),'y')
```

```
plot(Stime(13,:),S(13,:),'k')
plot(Stime(15,:),S(15,:),'b')
hold off


%% Plot extracted samples taken for second time point (switchc = 1)
figure;
hold on;
plot(Stime(2,:),S(2,:),'r')
plot(Stime(4,:),S(4,:),'g')
plot(Stime(6,:),S(6,:),'k')
plot(Stime(8,:),S(8,:),'m')
plot(Stime(10,:),S(10,:),'y')
plot(Stime(12,:),S(12,:),'k')
plot(Stime(14,:),S(14,:),'b')
plot(Stime(16,:),S(16,:),'b')
hold off

% Based on which waveforms are demultiplexed correctly in above figures,
% select either switchc = 0 or 1

% Digitally filter noise initial 950 LPF
[z,p,k] = butter(5,950/1000,'low');
[sos,g] = zp2sos(z,p,k);        % Convert to SOS form
Hd = dfilt.df2tsos(sos,g);   % Create a dfilt object
h = fvtool(Hd);              % Plot magnitude response
set(h,'Analysis','freq')        % Display frequency response
yfilta(1,:) = filter(Hd,S(1,:));
yfilta(2,:) = filter(Hd,S(3,:));
yfilta(3,:) = filter(Hd,S(5,:));
yfilta(4,:) = filter(Hd,S(7,:));
yfilta(5,:) = filter(Hd,S(9,:));
yfilta(6,:) = filter(Hd,S(11,:));
yfilta(7,:) = filter(Hd,S(13,:));
yfilta(8,:) = filter(Hd,S(15,:));

yfiltb(1,:) = filter(Hd,S(2,:));
yfiltb(2,:) = filter(Hd,S(4,:));
yfiltb(3,:) = filter(Hd,S(6,:));
yfiltb(4,:) = filter(Hd,S(8,:));
yfiltb(5,:) = filter(Hd,S(10,:));
yfiltb(6,:) = filter(Hd,S(12,:));
yfiltb(7,:) = filter(Hd,S(14,:));
yfiltb(8,:) = filter(Hd,S(16,:));


%% Calculate the mean of all of the filtered samples. One of the channels
%% is set to a DC voltage of 0 volts so that the physical locations of the
%% multiplexed signals can be extracted. Find this sample and reference all
%% the samples to this.

for i = 1:8
```

```
   yfiltamean(i) = mean(yfilta(i,:));
end
for i = 1:8
   yfiltbmean(i) = mean(yfiltb(i,:));
end

starti = 100;
yfilta = yfilta(:,starti:end);
yfiltb = yfiltb(:,starti:end);
Stime = Stime(:,starti:end);


yfiltaplot = zeros(8,length(yfilta));
zero = 0;

if(switchc == 0)
   % when switchc = 0, use the following columns of data
   zero = find(abs(yfiltamean) < 0.01);

   counter = 1;
   for z = 1:8
      if(zero == 8)
         yfiltaplot(counter,:) = yfilta(zero,:);
         zero = 1;
         counter = counter + 1;
      else
         yfiltaplot(counter,:) = yfilta(zero,:);
         zero = zero + 1;
         counter = counter + 1;
      end
   end

   figure;
   hold on;
   % Subtract the DC offsets from all of the channels and plot the
   % samples with fixed DC offsets for ease of viewing
   plot(Stime(1,:),yfiltaplot(1,:)-yfiltaplot(1,1),'b')
   plot(Stime(3,:),yfiltaplot(2,:)-yfiltaplot(2,1)+0.01,'m')
   plot(Stime(5,:),yfiltaplot(3,:)-yfiltaplot(3,1)+0.03,'y')
   plot(Stime(7,:),yfiltaplot(4,:)-yfiltaplot(4,1)+0.05,'k')
   plot(Stime(9,:),yfiltaplot(5,:)-yfiltaplot(5,1)+0.09,'m')
   plot(Stime(11,:),yfiltaplot(6,:)-yfiltaplot(6,1)+0.11,'y')
   plot(Stime(13,:),yfiltaplot(7,:)-yfiltaplot(7,1)+0.13,'k')
   plot(Stime(15,:),yfiltaplot(8,:)-yfiltaplot(8,1)+0.07,'b')
   xlabel('Time (s)')
   ylabel('Voltage (V)')

   set(gca,'FontName','Times New Roman','FontSize',14)
   set(get(gca,'XLabel'),'FontName','Times New Roman','FontSize',14)
   set(get(gca,'YLabel'),'FontName','Times New Roman','FontSize',14)
   hold off
   if(write == 1)
```

```
      % Write the demultiplexed signals to a file if write == 1

dlmwrite(sprintf('C:\\Users\\MEMS\\Documents\\Janet\\Cardiac\\72811_microcontroller\\72811_%s_P%s.txt',fi
lename,probe), yfiltaplot','delimiter','\t')
   end
else
   % when switchc = 1, use the following columns of data
   zero = find(abs(yfiltbmean) < 0.01);

   counter = 1;
   for z = 1:8
      if(zero == 8)
         yfiltbplot(counter,:) = yfiltb(zero,:);
         zero = 1;
         counter = counter + 1;
      else
         yfiltbplot(counter,:) = yfiltb(zero,:);
         zero = zero + 1;
         counter = counter + 1;
      end
   end


   figure;
   hold on;
   plot(Stime(2,:),yfiltbplot(1,:)-yfiltbplot(1,1),'b')
   plot(Stime(4,:),yfiltbplot(2,:)-yfiltbplot(2,1)+0.01,'m')
   plot(Stime(6,:),yfiltbplot(3,:)-yfiltbplot(3,1)+0.03,'y')
   plot(Stime(8,:),yfiltbplot(4,:)-yfiltbplot(4,1)+0.05,'k')
   plot(Stime(10,:),yfiltbplot(5,:)-yfiltbplot(5,1)+0.09,'m')
   plot(Stime(12,:),yfiltbplot(6,:)-yfiltbplot(6,1)+0.11,'y')
   plot(Stime(14,:),yfiltbplot(7,:)-yfiltbplot(7,1)+0.13,'k')
   plot(Stime(16,:),yfiltbplot(8,:)-yfiltbplot(8,1)+0.07,'b')
   xlabel('Time (s)')
   ylabel('Voltage (V)')
   set(gca,'FontName','Times New Roman','FontSize',14)
   set(get(gca,'XLabel'),'FontName','Times New Roman','FontSize',14)
   set(get(gca,'YLabel'),'FontName','Times New Roman','FontSize',14)
   hold off
   if(write == 1)
      % Write the demultiplexed signals to a file if write == 1

dlmwrite(sprintf('C:\\Users\\MEMS\\Documents\\Janet\\Cardiac\\72811_microcontroller\\72811_%s_P%s.txt',fi
lename,probe), yfiltbplot','delimiter','\t')
   end
end
```

APPENDIX C

GIANT SPHINX MOTH WEIGHT-CARRYING FLIGHT

The Giant Sphinx Moth was loaded with a microcontroller and battery. Video frames from the moth flight are shown below.

Additionally, the moth was loaded with magnets to test the limits of the weight-carrying capacity of the insects. The insect was able to carry at least 1.103 grams and generate sufficient lift for flight, as shown in the flight video frames below.

Figure C.1: Giant Sphinx moth flight at 0.07 and 0.33 seconds.

Figure C.2: Giant Sphinx moth flight at 0.53 and 1 seconds.

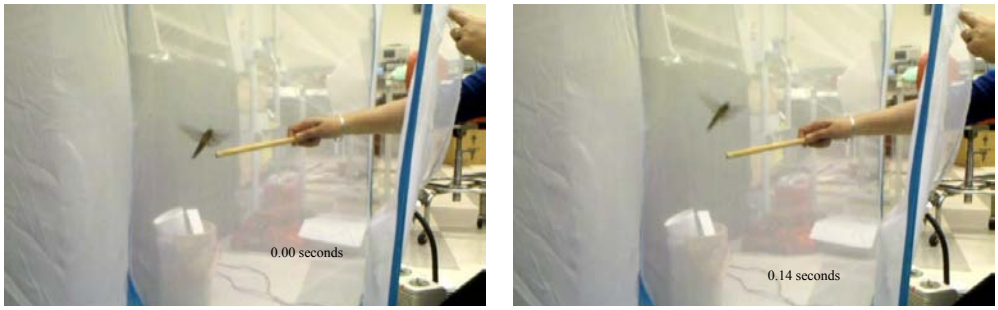

Figure C.3: Giant Sphinx moth flight with 1.103 gram load at 0.0 and 0.14 seconds.

Figure C.4: Giant Sphinx moth flight at 0.53 and 1 seconds.

APPENDIX D

ANSYS CODE FOR MINIATURE ULTRASONIC HORN PROBES WITH PZT

The ANSYS code for the miniaturize ultrasonic horn probe with PZT attached is below. The horn was modeled rigidly attached to PZT plates on either side of 3.55 by 1.25 mm in size.

```
!! Modified to include PZT coupling

!! CATENARY HORN PROBE FOR NEURAL RECORDINGS

FINISH
/CLEAR
/CWD, C:\horn
/Title, Catenary Horn 3D – Mini Ultrasonic Probe PZT/Si
/PREP7                    ! /PREP7: Enters the model creation preprocessor.

/UNIT,SI
/TRIAD,LBOT                    ! /TRIAD: Display triad in lower left screen corner
SMART,ON                ! SMART: Smart Meshing ?!



!-----------------------------------------------------------------------------
! PHYSICAL PARAMETERS FOR MODEL
!-----------------------------------------------------------------------------
NM=1E-9
UM=1E-6                    ! MICRON
MM=1E-3
CM=1E-2
MIL=25.4*UM                ! 1/1000 INCH
KHZ=1000
MHZ=1000*KHZ
GHZ=1000*MHZ

ZR=0                    ! ZERO

!SIN_T=500*NM
!ALN_T=224*NM

SIN_T=500e-9
ALN_T=224e-9


TSTEP = 10.0E-6            ! TECHNOLOGY STEP
FSTART=5.5*GHZ
FSTOP=5.8*GHZ

!-----------------------------------------------------------------------------
--
! MATERIAL PROPERTIES
!-----------------------------------------------------------------------------
--

ET,1,SOLID95                    ! ET: Defines a local element type from the element library
```

```
                    ! SOLID95 is a 3-D 8-node solid element
MP,EX,1,169e9               ! MP: Defines a linear material property as a constant or a function
MP,NUXY,1,0.22          ! temperature. EX – Elastic Moduli, NUXY – Minor Poisson's ratio
MP,DENS,1,2330              ! and DENS – Mass Density

ET,2,98                     ! FOR PZT (8 NODE COUPLED-FIELD)
!ET, 3, 92                 ! For Si (8-node solid) and glue


!-------------------------------------------------------------------------------
! PZT: MATERIAL PROPERTIES : CHECK PIEZOELECTRIC CONSTANT
!-------------------------------------------------------------------------------
MP,DENS,2,7530              ! DENSITY
MP,NUXY,2,.31               ! POISSON'S RATIO
MP,PERX,2,1700              ! RELATIVE PERMITTIVITY
MP,PERY,2,1700              ! RELATIVE PERMITTIVITY
MP,PERZ,2,1700              ! RELATIVE PERMITTIVITY

!TB,PIEZ,2                  ! DEFINE PIEZO. TABLE FOR PZT
!TBDATA,3,-6.10             ! PIEZO MATRIX CONSTANTS
!TBDATA,6,-6.10
!TBDATA,9,15.70

TB,PIEZ,2                   ! PIEZOELECTRIC "E" MATRIX OF PIEZOCERAMIC (PZT-4)
TBDATA,3,-5.2
TBDATA,6,-5.2               ! PHYSICAL ACOUSTIC PRINCIPLES AND METHODS
TBDATA,9,15.1               ! WARREN P. MASON VOLUME 1 ACADEMIC PRESS 1964
TBDATA,11,12.7
TBDATA,13,12.7

TB,ANEL,2                   ! STIFFNESS "C" MATRIX OF PIEZOCERAMIC (PZT-4)
TBDATA,1,13.9E10,7.78E10,7.43E10
TBDATA,7,13.9E10,7.43E10        ! PHYSICAL ACOUSTIC PRINCIPLES AND METHODS
TBDATA,12,11.5E10           ! WARREN P. MASON VOLUME 1 ACADEMIC PRESS 1964
TBDATA,16,2.56E10
TBDATA,19,2.56E10
TBDATA,21,3.06E10

!TB,ANEL,1                  ! DEFINE STRUCTURAL TABLE FOR PZT
!TBDATA,1,12.80E10,6.8E10,6.6E10 ! INPUT [C] MATRIX FOR PZT
!TBDATA,7,12.8E10,6.6E10
!TBDATA,12,11.0E10
!TBDATA,16,2.1E10
!TBDATA,19,2.1E10
!TBDATA,21,2.1E10

MP,MURX,2,0                 ! MATERIAL PROPERTIES TO SUPPRESS ERROR MESSAGES
MP,KXX,2,0                  ! MATERIAL PROPERTIES TO SUPPRESS ERROR MESSAGES
```

```
!-----------------------------------------------------------------------------------------------------------------------
--
! DEVICE DIMENSIONS AND SHAPE DEFINITION
!-----------------------------------------------------------------------------------------------------------------------
--

! HORN SHAPE

LEN=10E-3               ! Horn Length
W0=2.5E-3               ! End Width
W1=250E-6               ! Tip Width
DX=w1                   ! 'NOFPX-1' divisions in the horn part, 1mm each
NOFPX=(LEN)/DX+1
ALPHA=181.845           ! ALPHA=ACOSH(SQRT(W0/W1))/LEN
                        ! ANSYS doesn't haveACOSH function!

*DO,II,1,NOFPX          ! Define keypoints for the upper half of the horn
        XX=(II-1)*DX
        YY=W1*COSH(ALPHA*(LEN-XX))**2/2         ! divide by two
        K,0,XX,YY,0
        K,0,XX,0,0
*ENDDO

*DO,II,1,NOFPX-1        ! Define areas of the upper half of the horn by Keypoints
        A,2*II-1,2*II,2*(II+1),2*(II+1)-1
*ENDDO


! DUMMY DEVICE ON TOP

*DO,II,1,NOFPX          ! Define keypoints for the upper half of the horn
        XX=(II-1)*DX
        YY=W1*COSH(ALPHA*(LEN-XX))**2/2
        K,0,XX,YY,5E-4
        K,0,XX,0,5E-4
*ENDDO
*DO,II,1,NOFPX-1        ! Define areas of the upper half of the horn by Keypoints
        A,82+2*II-1,82+2*II,82+2*(II+1),82+2*(II+1)-1
*ENDDO

K,10001,0,0,0           ! K: Defines a Keypoint.
K,10002,0,0,-5E-4
L,10001,10002           ! L: Defines a line between two keypoints.
```

```
ASEL,s,loc,z,0,1E-4              ! ASEL: Selects a subset of areas.
!ASEL,r,loc,x,0,LEN
AADD,ALL                 ! AADD: Adds separate areas to create a single area.
VDRAG,ALL,0,0,0,0,0,243      ! VDRAG: Generates volumes by dragging an area pattern along a

K,10003,0,0,5E-4                 ! K: Defines a Keypoint.
L,10003,10002                    ! L: Defines a line between two keypoints.


ASEL,s,loc,z,5E-4, 6E-4          ! ASEL: Selects a subset of areas.
!ASEL,r,loc,x,0,LEN
AADD,ALL                 ! AADD: Adds separate areas to create a single area.
VDRAG,ALL,0,0,0,0,0,369      ! VDRAG: Generates volumes by dragging an area pattern along a
                         ! path.
VSEL,ALL
VADD,ALL
```

! CLAMP FOR THE LONGITUDINAL NODE WITH EARS

```
NODEX=3.75E-3                    ! COORDINATES OF THE DISPLACEMENT NODE
NODEY=0
NODEZ=0
CW=0.480E-3                          ! DIMENSIONS OF THE CLAMP BAR
CH=3.15E-3
!CH = 6.123E-3                       !!
EW=1.435E-3                          ! DIMENSIONS OF THE HORN'S EARS
EH=0.633E-3

K,50001,NODEX-CW/2,NODEY+CH/2,NODEZ
K,50002,NODEX+CW/2,NODEY+CH/2,NODEZ
K,50003,NODEX+CW/2,NODEY,NODEZ
K,50004,NODEX-CW/2,NODEY,NODEZ
A,50001,50002,50003,50004

K,50005,NODEX-EW/2,NODEY+CH/2,NODEZ
K,50006,NODEX+EW/2,NODEY+CH/2,NODEZ
K,50007,NODEX+EW/2,NODEY+CH/2-EH,NODEZ
K,50008,NODEX-EW/2,NODEY+CH/2-EH,NODEZ
A,50005,50006,50007,50008

ASEL,s,loc,x, NODEX-EW/2, NODEX+EW/2      ! ASEL: Selects a subset of areas.
ASEL,r,loc,z,0,1E-4
BOPTN,KEEP,NO
AOVLAP,ALL
AADD,ALL                         ! AADD: Adds separate areas to create a single area.


VDRAG,ALL,0,0,0,0,0,243      ! VDRAG: Generates volumes by dragging an area pattern along a
```

```
                                ! path.
VSEL,ALL
BTOL,0.5157E-5
VADD,ALL
VATT,1,,1
VSEL,ALL
VSEL, S, TYPE,,1



!-----------------------------------------------------------------------------------------------------------------------
--
! DEFINE PZT
!-----------------------------------------------------------------------------------------------------------------------
--

! PZT dimensions for mini probe are 3.55 mm x 1.25 mm

PZTW = 3.55E-3
PZTH = 1.25E-3
PZTT = 5E-4                ! Define PZT thickness – estimate as 500 um

K,60001,NODEX-PZTW/2, PZTH/2, 5E-4
K,60002,NODEX+PZTW/2, PZTH/2, 5E-4
K,60003,NODEX-PZTW/2, 0, 5E-4
K,60004, NODEX+PZTW/2, 0, 5E-4
A,60001,60002,60004,60003

K,60005,0,0,5E-4                ! K: Defines a Keypoint.
K,60006,0,0,5E-4+PZTT
L,60005,60006                ! L: Defines a line between keypoints

VDRAG,27,0,0,0,0,0,130        ! VDRAG: Generates volumes by dragging an area pattern along a
                                ! path.
VSEL,s,loc,z,5E-4+PZTT/4,5E-4+PZTT,,0
VATT,2,,1
VSEL,ALL
VGLUE, ALL


K,60007,NODEX-PZTW/2, PZTH/2, -5E-4
K,60008,NODEX+PZTW/2, PZTH/2, -5E-4
K,60009,NODEX-PZTW/2, 0, -5E-4
K,60010, NODEX+PZTW/2, 0, -5E-4
A,60007,60008,60010,60009

K,60011,0,0,-5E-4                ! K: Defines a Keypoint.
K,60012,0,0,-5E-4-PZTT
```

```
L,60011,60012                    ! L: Defines a line between keypoints

VDRAG,27,0,0,0,0,0,149           ! VDRAG: Generates volumes by dragging an area pattern along a
                                 ! path.
VSEL,s,loc,z,-5E-4-PZTT/4,-5E-4-PZTT,,0
VATT,2,,1


VSEL,ALL
VGLUE, ALL


! CURVE LEADING TO MICROPROBES

R=57.3E-6                        ! Radius of curvature leading into microprobes
DX2=11.46E-6
NOFPX2=R/DX2 + 1                 ! 'NOFPX2' divisions in the curved part, 15E  -6 each

III2=1
IXX2=LEN+(III2-1)*DX2
IYY2a=(W1/2)
!YY2b=SQRT((R**2 - (IXX2-(LEN+R))**2))
K, (100000+4*(III2-1)+1),IXX2,IYY2a,-1.5E-4
K, (100000+4*(III2-1)+1)+1,IXX2,0,-1.5E-4
K, (100000+4*(III2-1)+1)+2,IXX2,IYY2a,0
K, (100000+4*(III2-1)+1)+3,IXX2,0,0


*DO,II2,2,NOFPX2
        XX2=LEN+(II2-1)*DX2
        YY2a=(W1/2) - SQRT((R**2 - (XX2- (LEN+R))**2))
        !YY2b=SQRT((R**2 - (XX2-(LEN+R))**2))
        K, (100000+4*(II2-1)+1),XX2,YY2a,-1.5E-4
        K, (100000+4*(II2-1)+1)+1,XX2,0,-1.5E-4
        K, (100000+4*(II2-1)+1)+2,XX2,YY2a,0
        K, (100000+4*(II2-1)+1)+3,XX2,0,0
*ENDDO


*DO,II2,1,NOFPX2-1               ! Define areas of the upper half of the microprobe by Keypoints
V, (100000+4*(II2-1)+1), (100000+4*(II2-1)+1)+1, (100000+4*(II2-1)+1)+3, (100000+4*(II2-1)+1)+2,
(100000+4*(II2)+1), (100000+4*(II2)+1)+1, (100000+4*(II2)+1)+3, (100000+4*(II2)+1)+2
*ENDDO

!! Define probe tip

BLOCK, LEN+R, LEN+R+4.2E-3, 0, 66.5E-6,0,-1.5E-4
```

```
K,10004, LEN+R+4.2E-3, 66.5E-6,0
K,10005, LEN+R+4.2E-3, 0,0
K,10006, LEN+R+4.2E-3+109E-6, 0,0
K,10007, LEN+R+4.2E-3, 66.5E-6,-1.5E-4
K,10008, LEN+R+4.2E-3, 0, -1.5E-4
K,10009, LEN+R+4.2E-3+109E-6, 0, -1.5E-4
V,10004,10005,10006,10007,10008,10009

VSEL, S, LOC, X, LEN+DX2/2, LEN+R+4.2E-3+109E-6
VATT,1,,1

VSEL,ALL
VSEL, S, LOC, X, LEN+DX2/2, LEN+R+4.2E-3+109E-6
VSEL, A, VOLU,, 5

VADD,ALL

VSEL, ALL
VSYMM,Y,ALL

VSEL, ALL

VSEL, S, VOLU,,1
VSEL, A, VOLU,,2
VADD, ALL
VATT,2,,2

VSEL, S, VOLU,,3
VSEL, A, VOLU,,4
VADD, ALL
VATT,2,,2

VSEL, S, VOLU,,5
VSEL, A, VOLU,,11
VADD, ALL
VATT,1,,1


VSEL,ALL

                ! VATT: Associates element attributes with the selected, unmeshed
                    ! volumes. Element type defined in Material properties section.


!-----------------------------------------------------------------------------------------------------------------
--
! MESHING
```

```
!-----------------------------------------------------------------------------------------------------------------
--


!NUMMRG,KP                  ! NUMMRG: Merges coincident or equivalently defined items.

MSHKEY,0                ! MSHKEY: Specifies whether free meshing or mapped meshing
                        ! should be used to mesh a model. (Free meshing (0) used here)
MSHAPE,1                ! MSHAPE: For elements that support multiple shapes, specifies the
                        ! element shape to be used for meshing. (Triangle (1) used here)
MOPT,TETEXPND,2             ! MOPT: Specifies meshing options.
                        ! Before meshing a volume this will allow a mesh with elements that
                        ! are approximately twice as large in the interior of the volume as they
                        ! are on the boundary



!ESIZE = 1E-5
VMESH, 2


VMESH, 1
VMESH, 6

!VMESH,ALL                   ! VMESH: Generates nodes and volume elements within volumes.



!-------------------------------------------------------------------------------------
! ELECTRODE NODES
!-------------------------------------------------------------------------------------
!VSEL,S,TYPE,,2              ! SELECT VOLUME WITH ELEMENT TYPE ATTRIBUTE 1
VSEL,S,VOLU,,1


NSEL,ALL
NM = 1E-9
NSEL,S,LOC,Z,5E-4+NM,5E-4+NM        ! SELECT LOWER ELECTRODE NODES
NSEL, A, LOC, Z, -5E-4-NM, -5E-4-NM
CM,BOT_ELEC,NODE                ! TOP ELECTRODE NODE COMPONENT
CP,1,VOLT,ALL                   ! COUPLES VOLT DOF ON TOP ELECTRODE
*GET,NEL1,NODE,,NUM,MIN         ! GET LOWEST NODE NUMBER OF SELECTED NODE
SET

!VSEL,ALL
!VSEL,S,TYPE,,1
NSEL,S,LOC,Z,5E-4+PZTT-NM,5E-4+PZTT-NM
NSEL, A, LOC, Z, -5E-4-PZTT+NM,-5E-4-PZTT+NM
```

```
CM,TOP_ELEC,NODE
CP,2,VOLT,ALL
*GET,NEL2,NODE,,NUM,MIN

!ALLSEL
!FINISH

FINISH                          ! FINISH: Exits normally from a processor.


!-----------------------------------------------------------------------------------------------------------------------
--
! SOLUTION PROCESSOR
!-----------------------------------------------------------------------------------------------------------------------
--

/SOLU                           ! /SOLU: Enters the solution processor.
ANTYPE,MODAL                    ! ANTYPE: Specifies the analysis type and restart status.
RIGID,ALL               ! RIGID: Specifies known rigid body modes (if any) of the model.

D,TOP_ELEC,VOLT,0.0       ! ASSIGN ZERO POTENTIAL TO A NODE OF TOP ELECTRODE
D,BOT_ELEC,VOLT,0.0       ! ASSIGN ZERO POTENTIAL TO A NODE OF TOP ELECTRODE


! CLAMP DISPLACEMENT AT TIP OF MICROPROBES

!nsel,s,loc,x, LEN+R+4.70E-3+1E-4, LEN+R+4.70E-3+1E-4
!d,all,ux,0.0
!d,all,uy,0.0
!d,all,uz,0.0

! CLAMPING THE LONGITUDINAL NODE

nsel,s,loc,y, NODEY+CH/2-EH, NODEY+CH/2    ! clamp the displacement node area
nsel,r,loc,x, NODEX-EW/2, NODEX+EW/2
d,all,ux,0.0
d,all,uy,0.0
d,all,uz,0.0
nsel,s,loc,y, -NODEY-CH/2+EH, -NODEY-CH/2  ! clamp the displacement node area
nsel,r,loc,x, NODEX-EW/2, NODEX+EW/2
d,all,ux,0.0
d,all,uy,0.0
d,all,uz,0.0


NSEL,ALL                ! NSEL: Selects a subset of nodes.
!MODOPT,SUBSP,40            ! MODOPT: Specifies modal analysis options. (30 modes extracted)
!MXPAND,40,,,YES            ! MXPAND: Specifies the number of modes to expand and write for a
```

```
                        ! modal or buckling analysis.
MODOPT,LANB,60,1.5e5,1.5e6
MXPAND,60,,,YES
SOLVE                   ! SOLVE: Solve a solution.


FINISH                  ! FINISH: Exits normally from a processor.


!-----------------------------------------------------------------------------------------------------------------
--
! POST-PROCESSING
!-----------------------------------------------------------------------------------------------------------------
--

/POST1                  ! /POST1: Enters the database results postprocessor.
SET,NEAR,,,0,400000     ! SET: Defines the data set to be read from the results file.
                        ! Resonance frequency found to be 112.621 KHz, for mini probe 659

/WAIT,3                 ! /WAIT: Causes a delay before the reading of the next command.

N1=NODE(0,0,0)
N2=NODE(LEN+R+4.2E-3,0,0)
PATH,MYPATH,2,,100      ! DEFINE 'MYPATH' HAVING TWO POINTS,100 DIVISIONS
PPATH,1,N1              ! FISRT POINT ON 'MYPATH'
PPATH,2,N2              ! SECOND POINT ON 'MYPATH'
PDEF,DISPX,U,X      ! CALCULATE UX ON 'MYPATH' AND DEFINED AS 'DISPX'

/TITLE,X DISPLACEMENT IN PROBE
PLPATH,DISPX            !PLOT 'DISPX'
paget,ZLIST,TABLE
*STATUS,ZLIST


PDEF,DISPY,U,Y      ! CALCULATE UX ON 'MYPATH' AND DEFINED AS 'DISPX'
/TITLE,Y DISPLACEMENT IN CENTER LINE
PLPATH,DISPY            !PLOT 'DISPX'
paget,ZLIST,TABLE
*STATUS,ZLIST


PDEF,DISPY,U,Z      ! CALCULATE UX ON 'MYPATH' AND DEFINED AS 'DISPX'
/TITLE,Z DISPLACEMENT IN CENTER LINE
PLPATH,DISPZ            !PLOT 'DISPX'
paget,ZLIST,TABLE
*STATUS,ZLIST
```

BIBLIOGRAPHY

[1] R.E. Klabunde, "Cardiovascular pharmacology concepts," 2011.

[2] X. Chen, A. Lal, M.L. Riccio, and R.F. Gilmour Jr., "Ultrasonically actuated silicon microprobes for cardiac signal recording," *IEEE Transactions of Biomedical Engineering*, vol. 53, pp. 1665–1671, 2006.

[3] Abhishek Ramkumar, *Ultrasonic silicon horn actuators for biomedical applications: surgical tools, cardiac electrophysiological recordings, testicular tubule-size detection and fluid viscosity measurement*, Ph.D. thesis, Cornell University, 2010.

[4] P. Andreani and S. Mattison, "On the use of mos varactors in rf vco's," *IEEE Journal of Solid-State Circuits*, vol. 35, no. 6, 2000.

[5] T. Michaelis, T. Watanable, O. Natt, S. Boretius, J. Frahm, S. Utz, and J. Schachtner, "In vivo 3d mri of insect brain: cerebral development during metamorphosis of manduca sexta," *NeuroImage*, vol. 24, pp. 596–602, 2005.

[6] Po-Cheng Chen, "Transmitter design for bio-potential signals with ultrasonically guided insertion of silicon probes," M.S. thesis, Cornell University, 2011.

[7] C.R. Lowe, "An introduction to the concepts and technology of biosensors," *Biosensors*, vol. 1, pp. 3–16, 1985.

[8] E.M. Maynard, C.T. Nordhausen, and R.A. Normann, "The utah intracortical electrode array: a recording structure for potential brain-computer interfaces," *Electroencephalography and clinical Neurophysiology*, vol. 102, pp. 228–239, 1997.

[9] D.R. Kipke, "Implantable neural probe systems for cortical neuroprostheses," in *Proc. 2006 IEEE EMBS Conference*. 2006.

[10] Lewis Carroll (Charles L. Dodgson), *Neuroscience*, George MacDonald, 1865.

[11] R.F. Gilmour Jr., "Electrophysiology of the heart," *BIOAP 458 Class Notes*.

[12] Y. Hanein, K. Bohringer, R. Wyeth, and A. Willows, "Towards mems probes for intracellular recording," *Sensors Update*, vol. 10, pp. 47–75, 2002.

[13] P.J. Rousche, D.S. Pellinen, D.P. Pivin, J.C. Williams, R.J. Vetter, and D.R. Kipke, "Flexible polyimide-based intracortical electrode arrays with bioactive capability," *IEEE Transactions on Biomedical Engineering*, vol. 48, no. 3, 2001.

[14] Dae-Hyeong Kim and Jonathan Viventi et al., "Dissolvable films of silk fibroin for ultrathin conformal bio-integrated electronics," *Nature Materials*, vol. 9, pp. 511–517, 2010.

[15] V.S. Polikov, P.A. Tresco, and W.M. Reichert, "Response of brain tissue to chronically implanted neural electrodes," *Journal of Neuroscience Methods*, vol. 148, pp. 1–18, 2005.

[16] D.B. Jaroch, M.P. Ward, E.Y. Chow, J.L. Rickus, and P.P. Irazoqui, "Magnetic insertion system for flexible electrode implantation," *J. of Neuroscience Methods*, vol. 183, pp. 213–222, 2009.

[17] G.T.A. Kovacs, "Introduction to the theory, design, and modeling of thin-film microelectrodes for neural interfaces," in *Enabling Technologies for Cultured Neural Networks*. Academic Press, 1994.

[18] E.T. McAdams, A. Lackermeier, J.A. McLaughlin, and D. Macken, "The linear and non-linear electrical properties of the electrode-electrolyte interface," *Biosensors and Bioelectronics*, vol. 10, pp. 67–74, 1995.

[19] Amit Lal, *Micromachined silicon ultrasonic longitudinal-mode actuators: theory and applications to surgery, pumping, and atomization*, Ph.D. thesis, Cornell University, 1996.

[20] A. Ramkumar and A. Lal, "Silicon ultrasonic horn actuated microprobes based self-calibrating viscosity sensor," in *Proc. Int. IEEE MEMS 2010 Conference*. 2008.

[21] Y. Kim and S. Kwon, "Resistivity dependence of gauge factor of polysilicon strain gauge," *Micro and Nano Letters*, vol. 5, pp. 189–192, 2010.

[22] A. Ramkumar, R.F. Gilmour Jr., and A. Lal, "Ultrasonic microprobe based in vitro direct-mechanical stimulation of canine left-ventricular tissue," in *Proc. Int. IEEE Ultrasonics Symposium*. 2008.

[23] Antonio Arnau, *Piezoelectric Transducers and Applications*, Springer-Verlag, Berlin, 2008.

[24] M.K. Nabibekov, B.D. Plyushchenkov, and I.Y. Sarkisov, "Study of ultrasonic cutting of soft biotissues," *Mechanics of Composite Materials*, vol. 16(3), pp. 377–382, 1980.

[25] M. Stolz, R. Raiteri, A.U. Daniels, M.R. VanLandingham, W. Baschong, and U. Aebi, "Dynamic elastic modulus of porcine articular cartilage determined at two different levels of tissue organization by indentation-type atomic force microscopy," *Biophysical Journal*, vol. 86, pp. 3269–3283, 2004.

[26] A. Vinckier and G. Semenza, "Measuring elasticity of biological materials by atomic force microscopy," *FEBS Letters*, vol. 430, pp. 12–16, 1998.

[27] T. Nitta, H. Haga, K. Kawabata, K. Abe, and T. Sambongi, "Comparing microscopic with macroscopic elastic properties of polymer gel," *Ultramicroscopy*, vol. 82, pp. 223–226, 2000.

[28] A. Karma and R.F. Gilmour Jr., "Nonlinear dynamics of heart rhythm disorders," *Physics Today*, vol. 60, pp. 51–57, 2007.

[29] F.X. Witkowski, L.J. Leon, P.A. Penkoske, W.R. Giles, M.L. Spano, W.L Ditto, and A.T. Winfree, "Spatiotemporal evolution of ventricular fibrillation," *Nature*, vol. 392, pp. 78–82, 1998.

[30] J.M. Pastore, S.D. Girouard, K.R. Laurita, F.G. Akar, and D.S. Rosenbaum, "Mechanism linking t-wave alternans to the genesis of cardiac fibrillation," *Circulation*, vol. 99, pp. 1385–1394, 1999.

[31] D.A. Hooks, I.J. LeGrice, J.D. Harvey, and B.H. Smaill, "Intramural multisite recording of transmembrane potential in the heart," *Biophysical Journal*, vol. 81, pp. 2671–2680, 2001.

[32] J.P. DiMarco, "Implantable cardioverter-defibrillators," *The New England Journal of Medicine*, vol. 349, pp. 1836–1847, 2003.

[33] P.N. Jordan and D.J. Christini, "Adaptive diastolic interval control of cardiac action potential duration alternans," *J. of Cardio. Electrophys.*, vol. 15, no. 10, pp. 1836–1847, 2004.

[34] C.M. Berger, J.W. Cain, J.E.S. Socolar, and D.J. Gauthier, "Control of electrical alternans in simulations of paced myocardium using extended time-delay autosynchronization," *Phys. Rev. E. Stat. Nonlin. Soft Matter Phys.*, vol. 76, 2007.

[35] K. Najafi and J.F. Hetke, "Strength characterization of silicon microprobes in neurophysiological tissues," *IEEE Transactions of Biomedical Engineering*, vol. 37, pp. 474–481, 1990.

[36] A. Garfinkel, Y.H. Kim, O. Voroshilovsky, Z. Qu, J.R. Kil, M.H. Lee, H.S. Karagueuzian, J.N. Weiss, and P.S. Chen, "Preventing ventricular fibrillation by flattening cardiac restitution," *PNAS*, vol. 97, pp. 6061–6066, 2000.

[37] J.N. Weiss, A. Karma, Y. Shiferaw, P.S. Chen, A. Garfinkel, and Z. Qu, "From pulsus to pulseless: The saga of cardiac alternans," *Circulation Research*, vol. 98, pp. 1244–1253, 2006.

[38] W.E. Cascio, G.X. Yan, and A.G. Kleber, "Passive electrical properties, mechanical activity, and extracellular potassium in arterially perfused and ischemic rabbit ventricular muscle. effects of calcium entry blockade or hypocalcemia.," *Circulation Research*, vol. 66, pp. 1461–1473, 1990.

[39] E. Downar, M.J. Janse, and D. Durrer, "The effect of acute coronary artery occlusion on subepicardial transmembrane potentials in the intact porcine heart," *Circulation*, vol. 56, pp. 217–224, 1977.

[40] E. Kaplinsky, S. Ogawa, C.W. Balke, and L.S. Dreifus, "Two periods of early ventricular arrhythmia in the canine acute myocardial infarction model," *Circulation*, vol. 60, pp. 397–403, 1979.

[41] J.P. Boineau and J.L. Cox, "Slow ventricular activation in acute myocardial infarction: a source of re-entrant premature ventricular contractions," *Circulation*, vol. 48, pp. 702–713, 1973.

[42] S.G. Matsumoto and J.G. Hildebrand, "Olfactory mechanisms in the moth manduca sexta: response characteristics and morphology of central neurons in the antennal lobes," *Proc. of the Royal Society of London, Series B, Biological Sciences*, vol. 213, pp. 249–277, 1981.

[43] R.F. Gilmour Jr. and D.P. Zipes, "Different electrophysiological responses of canine endocardium and epicardium to combined hyperkalemia, hypoxia, and acidosis," *Circulation Research*, vol. 46, pp. 814–825, 1980.

[44] J.W. Dean and M.J. Lab, "Arrhythmia in heart failure: role of mechanically induced changes in electrophysiology," *The Lancet*, 1989.

[45] O.J. Elle, S. Halvorsen, M.G. Gulbrandsen, L. Aurdal, A. Bakken, E. Samset,

H. Dugstad, and E. Fosse, "Early recognition of regional cardiac ischemia using a 3-axis accelerometer sensor," *Physiological Measurement*, vol. 26, pp. 429–440, 2005.

[46] S.J. Eliades P. Mohseni, K. Najafi and X. Wang, "Wireless multichannel biopotential recording using an integrated fm telemetry circuit," *IEEE Transactions on Neural Systems and Rehabilitation Engineering*, vol. 13, no. 3, 2005.

[47] C.J. Shen, A. Ramkumar, A. Lal, and R.F. Gilmour Jr., "Wireless transmission of cardiac action potentials with ultrasonically guided insertion of silicon probes," in *Proc. Int. IEEE EMBC*. 2010.

[48] Simon Haykin, *Communication Systems, 3rd ed.*, John Wiley and Sons Inc., 1994.

[49] B.M. Tice, B. Rodriguez, J. Eason, and N. Trayanova, "Mechanistic investigation into the arrhythmogenic role of transmural heterogeneities in regional ischaemia phase 1a," *Europace*, vol. 9, pp. vi46–vi58, 2007.

[50] A. Hajimiri and T.H. Lee, *The design of low noise oscillators*, Kluwer Academic Publishers, Boston, 1999.

[51] M.L. Koller, M.L. Riccio, and R.F. Gilmour Jr., "Dynamic restitution of action potential duration during electrical alternans and ventricular fibrillation," *Am. J. Physiol. Heart Circ. Physiol.*, vol. 275, pp. 1635–1642, 1998.

[52] B. Kuhn, W. Denk, and R.M. Bruno, "In vivo two-photon voltage-sensitive dye imaging revelas top-down control of cortical layers 1 and 2 during wakefulness," *PNAS*, vol. 105, pp. 7588–7593, 2008.

[53] M.J. Huotari, "Biosensing by insect olfactory receptor neurons," *Sensors and Actuators B*, vol. 71, 2000.

[54] M.J. Schoning, S. Schutz, P. Schroth, B. Weissbecker, A. Steffer, P. Kordos, H.E. Hummel, and H. Luth, "A biofet on the basis of intact insect antennae," *Sensors and Actuators B*, vol. 47, 1998.

[55] R.L. Metcalf, "Ultramicrochemistry of insect semiochemicals," *Mikrochim. Acta*, vol. 129, 1998.

[56] C. Lindinger, P. Pollien, A. Santo, C. Yeretzian, I. Blank, and T. Mark, "Unambiguous identification of volatile compounds by proton-transfer reaction mass spectrometry coupled with gc/ms," *Anal. Chem.*, vol. 77, 2005.

[57] T.L. King, F.M. Horine, K.C. Daly, and B.H. Smith, "Explosives detection with hard-wired moths," *IEEE Trans. on Instrum. and Meas.*, vol. 53, 2004.

[58] D.J. Blackiston, C.E. Silva, and M.R. Weiss, "Retention of memory through metamorphosis: can a moth remember what it learned as a caterpillar?," *PLoS ONE*, vol. 3, 2008.

[59] A. Paul, A. Bozkurt, J. Ewer, B. Blossey, and A. Lal, "Surgically implanted micro-platforms in manduca sexta moths," *Hilton Head Island Solid-State Sensors, Actuators, and Microsystems Workshop*, vol. 1, 2006.

[60] H.F. Nijhout and C.M. Williams, "Control of moulting and metamorphosis in the tobacco hornworm, manduca sexta (l.): Cessation of juvenile hormone secretion as a trigger for pupation," *J. Exp. Biol.*, vol. 61, 1974.

[61] B.S. Hansson and S. Anton, "Function and morphology of the antennal lobe: New developments," *Annu. Rev. Entomol.*, vol. 45, pp. 203–231, 2000.

[62] T.A. Christensen and J.G. Hildebrand, "Male-specific, sex pheromone-selective projection neurons in the antennal lobes of the moth manduca sexta," *J. Comp. Physiol. A*, vol. 160, pp. 553–569, 1987.

[63] R. Kanzaki, E.A. Arbas, N.J. Strausfeld, , and J.G. Hildebrand, "Physiology and morphology of projection neurons in the antennal lobe of the male moth manduca sexta," *J. Comp. Physiol. A*, vol. 165, pp. 427–453, 1989.

[64] S.G. Matsumoto and J.G. Hildebrand, "Olfactory mechanisms in the moth manduca sexta: response characteristics and morphology of central neurons in the antennal lobes," *Proc. of the Royal Society of London, Series B, Biological Sciences*, vol. 213, pp. 249–277, 1981.

[65] E.S. Schweitzer, J.R. Sanes, and J.G. Hildebrand, "Ontogeny of electroantennogram responses in the moth, manduca sexta," *J. Insect Physiology*, vol. 22, pp. 955–960, 1976.

[66] C.P. Pennisi, C. Sevcencu, A. Dolatshahi-Pirouz, M. Foss, J.L. Hansen, A.N. Larsen, V. Zachar, F. Besenbacher, and K. Yoshida, "Response of fibroblasts

and glial cells to nanostructured platinum surfaces," *Nanotechnology*, vol. 20, 2009.

[67] R. Biran, M.D. Noble, and P.A. Tresco, "Characterization of cortical astrocytes on materials of differing surface chemistry," *J. of Biomedical Materials Research*, vol. 46, 1999.

[68] D.J. Edell, V.V. Toi, V.M. McNeil, and L.D. Clark, "Factors influencing the biocompatibility of insertable silicon microshafts in cerebral cortex," *IEEE Transactions on Biomedical Engineering*, vol. 39, pp. 635–643, 1992.

[69] P.J. Rousche and R.A. Normann, "A system for impact insertion of a 100 electrode array into cortical tissue," in *Proc. Int. IEEE EMBS Conference*. 1990.

[70] K.A. Ludwig, N.B. Langhals, M.D. Joseph, S.M. Richardson-Burns, J.L. Hendricks, and D.R. Kipke, "Poly(3,4-ethylenedioxythiophene) (pedot) polymer coatings facilitate smaller neural recording electrodes," *J. Neural Eng.*, vol. 8, 2011.

[71] X.T. Cui and D.D. Zhou, "Poly(3,4-ethylenedioxythiophene) for chronic neural stimulation," *IEEE Trans. on Neural Systems and Rehabilitation Engineering*, vol. 15, pp. 502–508, 2007.

[72] K.A. Ludwig, J.D. Uram, J. Yang, D.C. Martin, and D.R. Kipke, "Chronic neural recordings using silicon microelectrode arrays electrochemically deposited with a poly(3,4-ethylenedioxythiophene) (pedot) film," *J. Neural Eng.*, vol. 3, 2006.

[73] P.M. Klinge, M.A. Vafa, T. Brinker, A. Brandis, G.F. Walter, T. Stieglitz, M. Samii, and K. Wewetzer, "Immunohistochemical characterization of axonal sprouting and reactive tissue changes after long-term implantation of a polyimide sieve electrode to the transected adult rat sciatic nerve," *Biomaterials*, vol. 22, pp. 2333–2343, 2001.

[74] T. Stieglitz and M. Gross, "Flexible biomems with electrode arrangements on front and back side as key component in neural prostheses and biohybrid systems," *Sensors and Actuators B*, vol. 83, pp. 8–14, 2002.